

Georgia State University

## ScholarWorks @ Georgia State University

---

Physics and Astronomy Dissertations

Department of Physics and Astronomy

---

5-4-2020

### Optoelectronic and Transport Properties of Indium Nitride

Garnett Cross

Follow this and additional works at: [https://scholarworks.gsu.edu/phy\\_astr\\_diss](https://scholarworks.gsu.edu/phy_astr_diss)

---

#### Recommended Citation

Cross, Garnett, "Optoelectronic and Transport Properties of Indium Nitride." Dissertation, Georgia State University, 2020.

doi: <https://doi.org/10.57709/17466223>

This Dissertation is brought to you for free and open access by the Department of Physics and Astronomy at ScholarWorks @ Georgia State University. It has been accepted for inclusion in Physics and Astronomy Dissertations by an authorized administrator of ScholarWorks @ Georgia State University. For more information, please contact [scholarworks@gsu.edu](mailto:scholarworks@gsu.edu).

# OPTOELECTRONIC AND TRANSPORT PROPERTIES OF INDIUM NITRIDE

by

GARNETT BRENDAN CROSS

Under the Direction of Alexander Kozhanov, PhD and Nikolaus Dietz, PhD

## ABSTRACT

In this thesis I document the growth of InN above accepted decomposition temperatures of 630°C and discuss the analysis of the Fourier-transform infrared spectroscopy measurements of InN properties. InN films were grown by MEPA-MOCVD at growth temperatures ranging from 700 to 957 °C. The evidence of InN presence in grown films is presented from infrared spectroscopy, X-ray diffraction studies, Raman spectroscopy, and atomic force microscopy. The data and previous studies indicate polycrystalline grainy InN film partially with dominant epitaxial material crystallographically locked to the substrate. The mathematical modelling of infrared reflectance and comparison with data is performed for non-polarized light. A model is applied to

extract thickness, carrier concentration and phonon frequencies for InN film grown on sapphire.

The developed model can be refined to analyze other III-Nitride materials, including multilayer heterostructures as the optoelectronic calculations are similar for this class of material.

INDEX WORDS: Indium nitride, Group III-nitrides, FTIR, Phonon structure, Hopping conductivity, Grain conductivity, Semiconductor physics, Electron transport

OPTOELECTRONIC AND TRANSPORT PROPERTIES OF INDIUM NITRIDE

by

GARNETT BRENDAN CROSS

A Dissertation Submitted in Partial Fulfillment of the Requirements for the Degree of

Doctor of Philosophy

in the College of Arts and Sciences

Georgia State University

2020

Copyright by  
Garnett Brendan Cross  
2020

# OPTOELECTRONIC AND TRANSPORT PROPERTIES OF INDIUM NITRIDE

by

GARNETT BRENDAN CROSS

Committee Chair: Alexander Kozhanov

Committee: Vadym Apalkov

Douglas Gies

Sidong Lei

Electronic Version Approved:

Office of Graduate Studies

College of Arts and Sciences

Georgia State University

May 2020

## DEDICATION

I want to dedicate this work to my wife and kids. Becca thank you for pushing me to do what I wanted to, even when I wasn't sure it was worth it or felt that I couldn't carry on. Danny, Andy, Davy and Gid, I hope that you see this as an example, pursue what you want, even if it doesn't make sense, God has a plan for each of you.

I would like to thank my parents, Gevin and Shona Cross for their support through this time. They never stopped believing I could do it, even as I came close to giving up sometimes. I would like to thank my parents-in-law, Don and Pam Prouty as well, their constant affirmation and holiday conversations re-invigorated me, and having family around always distracted the kids so I could have a breather.

My work friends also helped pull me through this. Thank you, Mark for always being around for me to complain to about apparatus, programming and science. I always appreciated being able to bounce ideas off you and that you listened even if I spouted nonsense to "help" with your problems. Thank you, Zaheer for always complimenting me and making me feel a bit better about the little bits that I could contribute to your work. Thank you Alireza and Sampath for your wisdom and patience with me as I struggled to find my path. And last, but not least, thank you Tim for always helping me focus, the first two years of this would not have been nearly as enjoyable without your company. And the bonus of getting to bug you over the last three years whenever I needed to vent has been a blessing. I must also thank all the grad students in our department, it is always nice to have someone to talk to when I am at work, I have enjoyed getting to know all of you.

Thank you, Alex for stepping in at a time of crisis in my life and providing guidance and helping to round me out as a researcher, even when it did not make sense in your career.

I especially want to thank Vivian Dietz and Vincent Woods. With the passing of Dr. Dietz they both went out of their way to support my life and career as they were going through grief that I cannot imagine.

I could not ask for better people in my life, thank you all for making me a part of yours.



## ACKNOWLEDGEMENTS

I would like to acknowledge the work of all the members of this research group as I have been able to build upon the work of so many talented individuals. I would especially like to acknowledge the work of Mark Vernon, Zaheer Ahmad, Daniel Seidlitz and Indika Kankanamge, my contemporaries and people who directly helped me publish my work. I would like to acknowledge my two primary advisors, Nikolaus Dietz and Alexander Kozhanov, two men who shared their talent and expertise with me to make this work a success and for helping me to identify talents I didn't know I had. I would like to thank the researchers who have taken the time to inspect my work and push me to be better, Vadym Apalkov, Sidong Lei, Michael Williams and Douglas Gies. Lastly, I would like to thank Pete Walker and his staff for always being willing to help make my little projects work and keeping our equipment running.

This work was supported by the DOE grant NA-22-WMS-#66204 via PNNL subcontract and NSF grant #EAR-1029020.

## TABLE OF CONTENTS

<b>ACKNOWLEDGEMENTS .....</b>	<b>III</b>
<b>LIST OF TABLES .....</b>	<b>VII</b>
<b>LIST OF FIGURES .....</b>	<b>VIII</b>
<b>LIST OF ABBREVIATIONS .....</b>	<b>XIII</b>
<b>1 INTRODUCTION.....</b>	<b>1</b>
<b>1.1 History of InN.....</b>	<b>3</b>
<b>1.2 Physical structure of the group III-nitrides.....</b>	<b>11</b>
<b>1.3 Growth of group III-nitrides.....</b>	<b>14</b>
<i>1.3.1 Metal-Organic Chemical Vapor Deposition (MOCVD) .....</i>	<i>14</i>
<i>1.3.2 Migration Enhanced Plasma Assisted (MEPA-) and Plasma Assisted (PA-) MOCVD .....</i>	<i>15</i>
<b>1.4 Dissertation overview.....</b>	<b>17</b>
<b>2 EXPERIMENTAL METHODS .....</b>	<b>18</b>
<b>2.1 Sample growth.....</b>	<b>18</b>
<i>2.1.1 MOCVD growth system.....</i>	<i>18</i>
<i>2.1.2 MEPA-/PA-MOCVD .....</i>	<i>24</i>
<b>2.2 Film Characterization.....</b>	<b>27</b>
<i>2.2.1 Optical microscopy .....</i>	<i>27</i>
<i>2.2.2 Reflectance spectroscopy.....</i>	<i>29</i>

2.2.3	<i>Raman spectroscopy</i> .....	36
2.2.4	<i>Atomic Force Microscopy</i> .....	40
2.2.5	<i>X-ray Diffraction</i> .....	43
2.2.6	<i>Transport measurement</i> .....	44
3	<b>KINETICALLY STABILIZED HIGH TEMPERATURE GROWTH OF INDIUM NITRIDE</b> .....	48
3.1	<b>Introduction</b> .....	48
3.2	<b>Samples</b> .....	51
3.3	<b>Results</b> .....	53
3.3.1	<i>Raman spectroscopy</i> .....	53
3.3.2	<i>FTIR spectroscopy and modelling the film thickness</i> .....	58
3.3.3	<i>Atomic Force Microscopy</i> .....	61
3.3.4	<i>X-ray Diffraction</i> .....	64
3.3.5	<i>Hall measurements</i> .....	66
3.4	<b>Discussion</b> .....	68
3.5	<b>Further Work</b> .....	70
3.6	<b>Conclusion</b> .....	72
4	<b>OPTOELECTRONIC MODELLING OF THIN LAYER INDIUM NITRIDE AND MULTILAYER STACKS</b> .....	73
4.1	<b>Background</b> .....	74

4.1.1	<i>Multi-layer stack modelling – Generalized Transfer Matrix Method</i> .....	74
4.1.2	<i>Multi-layer stack modelling – Anisotropic media</i> .....	78
4.1.3	<i>Dielectric functions and tensors</i> .....	80
4.2	<b>MATLAB Script for fitting FTIR data</b> .....	83
4.3	<b>FTIR Modelling Results</b> .....	85
4.4	<b>Conclusion</b> .....	88
5	<b>CONCLUSIONS</b> .....	89
5.1	<b>High-temperature growth of InN</b> .....	89
5.2	<b>FTIR modelling of InN and multilayer structures</b> .....	90
	<b>REFERENCES</b> .....	92
	<b>APPENDICES</b> .....	104
	<b>Appendix A Mathematica Script to find the Matrix representations of the Reflected field</b> <b>(<math>E_r</math>) and Refracted Field (<math>E_t</math>), as a function of the incident field (<math>E_i</math>)</b> .....	104
	<b>Appendix B MATLAB Program to model reflectance data and compare it to experimental</b> <b>Data</b> .....	105

## LIST OF TABLES

Table 1-1 Lattice constants for aluminum, gallium and indium nitride .....	13
Table 3-1 List of samples and relevant growth parameters used to study the effect of High temperature on InN growth in MEPA-MOCVD .....	53
Table 3-2 Raman shifts of E <sub>2</sub> -(high) and A <sub>1</sub> -LO phonon modes with their widths.....	56
Table 3-3 Parameters used to model the reflectance of measured samples.....	60
Table 3-4 Statistics collected from the AFM scan data .....	64
Table 4-1 Table of Fitting parameters for FTIR model .....	83
Table 4-2 Initial values for FTIR reflectance model. Note: $\theta_c$ is limited to values between 0 and $\pi/2$ .....	85
Table 4-3 Model parameters found in fitting program .....	87

## LIST OF FIGURES

Figure 1-1 Bandgap and lattice constant of the III-Nitride system in comparison to other III-V materials.[13] .....	2
Figure 1-2 Plot of the stability of InN in an N <sub>2</sub> atmosphere, taken from [33]. Open circles represent the presence of metallic In on sample after exposure to graphed conditions. ....	4
Figure 1-3 InN film thickness as a function of time for the nitridization of InP [36] .....	6
Figure 1-4 SEM photograph and RHEED patterns for growth of InN by MOCVD [17] .....	8
Figure 1-5 Photoluminescence spectra of InN grown by metal-organic MBE (solid line carrier concentration of $9 \times 10^{18} \text{ cm}^{-3}$ ) and plasma assisted MBE (dashed line carrier concentration of $1.2 \times 10^{19} \text{ cm}^{-3}$ )[74] .....	10
Figure 1-6 Representation of Wurtzite structure. Grey spheres represent the group III metal, small yellow spheres represent nitrogen. Dashed lines represent III-metal – N bonds. Shading represents different layers. ....	12
Figure 1-7 Unit cell for group III-Nitrides/wurtzite structure, showing a, b and c vectors, in the wurtzite structure the magnitude of a and b are the same. ....	13
Figure 2-1 Sketch of modified Emcore/Veeco D125 MOCVD reactor .....	19
Figure 2-2 Picture of MOCVD Reactor showing gas tubing and optical pyrometer entering the top of the reactor. The large tube off to the right is the gate valve toward the load-lock. ....	20
Figure 2-3 Growth reaction diagram at substrate surface for GaN.....	21
Figure 2-4 Growth control and feedback parameter plot recorded for a typical GaN growth run. ....	23
Figure 2-5 AFM scans of GaN template grown on sapphire substrates by MOCVD. ....	24

Figure 2-6 Picture of the MEPA-/PA-MOCVD reactor showing the plasma source on top and load-lock and gate valve on the right .....	25
Figure 2-7 Schematic of the MEPA-PA-MOCVD reactor .....	26
Figure 2-8 Microscope images of GaN, InN and AlGaIn. a) GaN without any visible defects. b) 3-dimensional growth of GaN. c) clustering on InN surface. d) substrate related defects creating imperfections in an AlGaIn film. e) Strain cracking in AlGaIn film. ....	28
Figure 2-9 Schematic for an electromagnetic wave interacting with a material. Representations are provided for P (TM) and S (TE) polarization. ....	30
Figure 2-10 Sketch of NIRS setup for collecting the elastic scattering of light at near-normal incidence .....	34
Figure 2-11 Picture of apparatus for UV-visible near-normal incidence reflectance spectroscopy .....	34
Figure 2-12 Sketch of the mechanism of an FTIR spectrometer .....	35
Figure 2-13 Picture of the Nicolet 6700 FTIR spectrometer with Pike Map300 sample stage. ...	36
Figure 2-14 Picture of custom Raman spectrometer.....	38
Figure 2-15 Sketch of a Raman spectrometer.....	39
Figure 2-16 Figure containing data analyzed with and without compensating for errors in the orientation of optical elements compared to data from a professional confocal Raman spectrometer.....	40
Figure 2-17 Sketch of the mechanism for the operation of the AFM.....	41
Figure 2-18 Picture of the Veeco Multimode AFM.....	42
Figure 2-19 Diagram of X-rays reflecting off consecutive layers of crystal lattice. ....	43

Figure 2-20 Sketch of a sample set up for measuring Van der Pauw technique. Samples can be connected through any of the numbered contacts.....	44
Figure 2-21 Possible geometries for Hall measurements, including Hall bar (a) test bridge 5(b), and van der Pauw geometries (c and d) [109].....	45
Figure 2-22 Block diagram of Hall coefficient and resistivity measurement apparatus.....	47
Figure 3-1 Plot of InN stability as a function of nitrogen pressure. Plot from [66] including data from [122]. .....	49
Figure 3-2 A schematic representation of one cycle of the growth phase. ....	52
Figure 3-3 Raman spectra of the sample grown at 929°C with (red) lines indicating individual phonon modes and (green) whole spectra multi-peak fitting.....	54
Figure 3-4 Raman spectra for all samples in this experiment, Dashed lines indicate phonon modes that should be visible in this orientation. ....	55
Figure 3-5 FWHM of the E2(high) phonon peak as a function of temperature. ....	56
Figure 3-6 Raman data from 2000 to 2600 $\text{cm}^{-1}$ showing no significant peak associated with InN. ....	57
Figure 3-7 FTIR reflectance spectrum measured on InN sample grown on c-plane Sapphire.....	58
Figure 3-8 IR spectrum showing the data and model over the fitted range for sample 1165, grown at 929 °C.....	59
Figure 3-9 Growth rate as a function of growth temperature, showing a peak growth rate at 873°C. The growth rate measurement error is negligibly small as compared to the data symbol size. ....	60
Figure 3-10 AFM scans of sample 1170.....	61
Figure 3-11 AFM scans of sample 1162.....	61



Figure 3-12 AFM scans of sample 1166.....	62
Figure 3-13 AFM scans of sample 1165.....	62
Figure 3-14 AFM scans of sample 1167.....	63
Figure 3-15 XRD data of InN grown at 825 °C. Spectrum demonstrates presence of InN. The peak at 33° has not been identified as [149] claims it belongs to InN and [150,151] identify it as belonging to In. The peak at 40° also remains unidentified.....	65
Figure 3-16 Resistivity for thin (<75 nm) InN samples on Sapphire, growth temperatures are labelled. Resistivity of sample 1165, grown at 816 °C, is shown for detail of resistivity as a function of measurement temperature (x-axis). ....	66
Figure 3-17 Free electron concentration for each sample as a function of temperature. The electron concentration of sample 1165 plotted separately to show detail as a function of temperature. ....	67
Figure 3-18 Mobility of each sample as a function of temperature, and for sample 1165 to show detail.....	67
Figure 3-19. Temperature dependence of the E2(high) (empty squares for sharp peak, solid squares for broad peak) and A1(LO) phonon mode peak FWHM (triangles). Dashed line illustrates the trend. ....	68
Figure 3-20 Arrhenius plots for resistivity for all samples and for sample 1165 to calculate activation energy from slope.....	70
Figure 3-21 Surface topography and tapping probe phase difference on sample 1166.....	71
Figure 4-1 Field components for generalized transfer matrix method at an interface. Note the arrows are not propagation or field vectors, but rather indicative of the approximate direction of field propagation associated with each electric field.....	74

Figure 4-2 Field components for a propagation matrix of the generalized transfer matrix method .....	75
Figure 4-3 Field components for a 3-layer stack. ....	75
Figure 4-4 Surface parallel components of the electric and magnetic strength fields. ....	78
Figure 4-5 Experimental reflectance and modelled reflectance for sample 1167 .....	86

## LIST OF ABBREVIATIONS

AFM	Atomic Force Microscopy
CCD	charge-coupled device
HPCVD	High Pressure Chemical Vapor Deposition
IR	InfraRed
FTIR	Fourier Transform InfraRed Spectroscopy
MOCVD	Metal-Organic Chemical Vapor Deposition, also OMCVD
MOVPE	Metal organic vapor phase epitaxy
NIRS	Normal Incidence Reflectance Spectroscopy, can be any wavelength, used to refer to UV/Visible spectroscopy in this work
OMCVD	Organometallic Chemical Vapor Deposition, also MOCVD
MBE	molecular beam epitaxy
MIS	Metal-insulator-semiconductor, referring to material multilayer structure
MEPA-MOCVD	Migration Enhanced Plasma assisted MOCVD
RF	radio frequency
PLD	pulsed laser deposition
SIMS	Secondary Ion Mass Spectrometry
TMA	Tri-Methyl Aluminum
TMG	Tri-Methyl Gallium
TMI	Tri-Methyl Indium
XRD	X-ray Diffraction
LO	Longitudinal Optical – referring to phonons
MO	Metalorganic
TO	Transverse Optical – referring to phonons
TM	Transverse Magnetic – magnetic field parallel to surface
TE	Transverse Electric – electric field parallel to surface
UV	Ultraviolet

## 1 INTRODUCTION

The group III-nitrides are a class of binary semiconductor materials, combining nitrogen with aluminum, gallium, or indium to form aluminum nitride (AlN), gallium nitride (GaN) and indium nitride (InN). This material class has the distinction of being high-mobility, thermally stable, structurally similar and with a wide range of bandgaps.

These materials are well-known for electronic and optoelectronic devices that can serve as detectors, photovoltaics or light sources. The group III-nitrides are also being tested in different forms as quantum dots, nano-wires, [1–6] that can be used for light generation and tagging of microscopic particles. These materials can be engineered to exhibit tunable plasmonic resonance for the generation of strong local electromagnetic fields [7].

One of the most common forms of optoelectronic devices that are based on the group III-nitrides are blue light emitting diodes (LEDs) [8–13] and blue lasers [14] now commonly used in Blu-ray players. Isamu Akasaki, Hiroshi Amano and Shuji Nakamura were awarded the Nobel Prize in 2014 for their work on energy efficient blue LEDs, based on group III-nitride materials. Other optoelectronic device applications include quantum cascade lasers [15], versatile light sources that are capable of being tuned to different wavelengths as opposed to a single wavelength laser, and photovoltaic devices, potentially one of the most important fields of application for InN [16–21].

GaN is also used in the fabrication of high electron mobility transistors (HEMTs) [22]. These transistors can operate in higher temperature environments, allowing them to be used in high power electronics. These devices are also energy-efficient, which is important in electric power delivery in mobile applications. Recently, this application became a reality as vehicles move away from combustion toward electric power.

The structural similarity of the III-Nitride class materials means that these materials theoretically can be alloyed, and their properties will mix, allowing for a variation from the distinct properties of the three materials to a continuum of properties across the ranges spanned by each of the III-nitrides. The bandgaps of the group III-nitrides are 6.2 eV, 3.4 eV, and 0.67 eV for AlN, GaN, and InN respectively. GaN and AlN both have wide bandgaps, this means that individually they both are only relevant for high energy applications. With their light emission and absorption both being in the ultraviolet (UV) part of the spectrum these materials have proven to be useful for optoelectronic application in the UV range or as excitation sources for other photoluminescent materials. Having InN with a bandgap in the infrared (IR) should allow alloying it with GaN or AlN to produce ternary alloys (InAlN or InGaN). With the bandgap of the materials varying based on the indium, these materials would be suitable for optoelectronic applications operating at wavelengths ranging from infrared and ultraviolet, as can be seen in Figure 1-1. Being able to make a material that can be tuned to be sensitive to any part of the visible spectrum of light would be the beginning of an exciting time in consumer electronics at least.

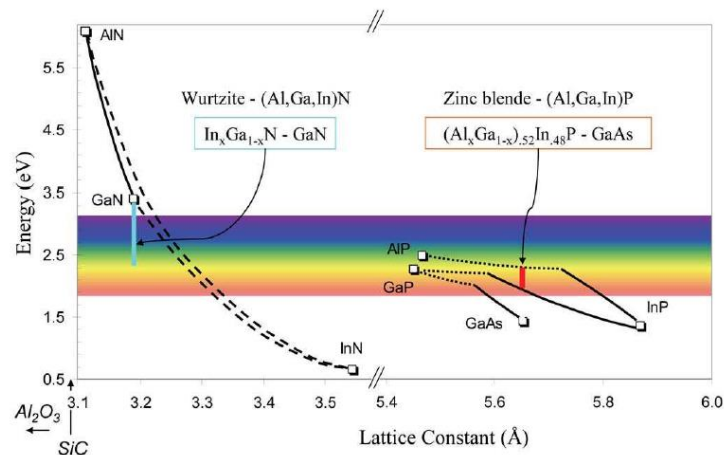


Figure 1-1 Bandgap and lattice constant of the III-Nitride system in comparison to other III-V materials.[13]

Even more interesting from the applications point of view would be utilization of InN/GaN and InN/AlN based heterostructures, that would allow utilizing advantages of 2D electron gas in these materials. While growth of InN on GaN and AlN is well established, growing GaN and AlN on top of InN presents a known challenge. Growth of AlN and GaN is typically performed at conditions resulting in InN decomposition. In this work I present research results demonstrating InN stability at higher temperatures, an extension of the growth parameter window of indium nitride so there is an overlap with the growth parameter windows of the other group III-nitrides. I also present a method to monitor the crystal properties, carrier concentration and layer thickness of the group III-nitrides as they are grown.

## 1.1 History of InN

Indium Nitride was first synthesized just over 80 years ago, with it only really being researched for the last 50 years due to interest in semiconductors. Challenges in the production of high quality, crystalline InN led scientist to understand its bandgap was significantly larger than its actual value. Accurately measuring the bandgap in 2002 revived interest in the material. In this section I review the key points in the history of the synthesis of Indium nitride with a secondary focus on the measurement of its infrared properties as they pertain to my work.

Indium nitride was first documented in 1938 as a fine black powder formed from the reaction of Hexafluoroindate,  $(\text{NH}_4)_3\text{InF}_6$ , and Ammonia, with Brauer describing the structure as wurtzite [23,24]. Samsonov [25] references two other methods of InN powder and small crystal growth by the reaction of InCl with ammonia [26] in 1959, and InO with ammonia [27] in 1963. In 1962, Sclar [28] predicted a bandgap for InN of 2.55 eV using the ionic and covalent radii of the constituent materials, which seemed to be in good agreement with previously published work by Popper [29]. It was also in good agreement with the 2.4 eV measured by Ormont in 1959 [30,31].

In 1963 a study by Alekseevski reported the absence of superconductivity in InN above 1.38 K, even though GaN demonstrated a superconducting phase transition at  $T_c = 5.85$  K [32].

In 1970 MacChesney et al. used InN, produced using the same methods as Juza and Hahn [23], to study the thermal stability of InN as a function of temperature. They published a heat of formation for InN of -34.2 kcal/mole between 795 and 945 K (522-672 °C), with the highest temperature demonstrating stability only under approximately  $10^8$  Pa of nitrogen as seen in Figure 1-2. One of the interesting statements made by MacChesney et al. [33] was an off-handed remark that due to InN having theoretically the lowest melting temperature, it would be the easiest of the group III-nitrides to grow and analyze, something that has not proved true.

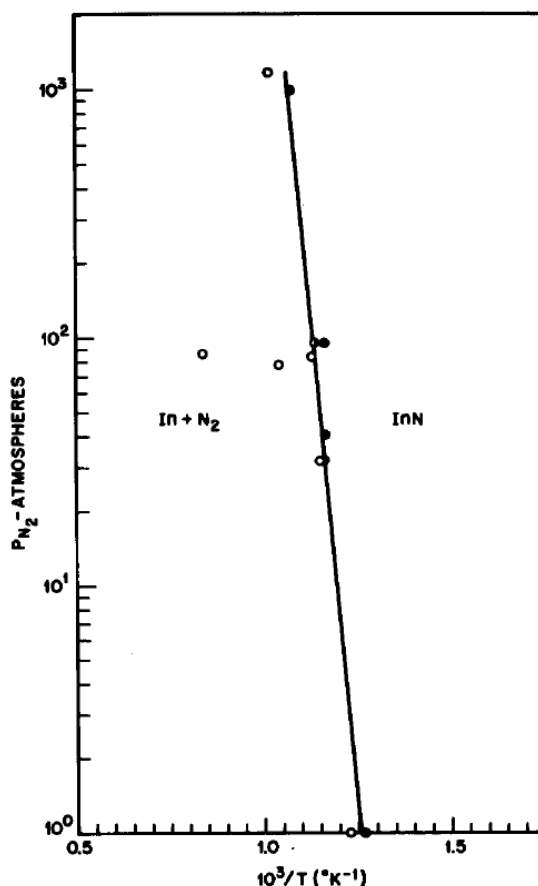


Figure 1-2 Plot of the stability of InN in an N<sub>2</sub> atmosphere, taken from [33]. Open circles represent the presence of metallic In on sample after exposure to graphed conditions.

In 1972 [34] and 1975 [35] two groups did further work in producing indium nitride through the RF-sputtering of indium-coated and pure indium cathodes. Hovel and Cuomo [34] did report synthesis of InN at 600°C at pressures of 20 mTorr, outside the thresholds established for decomposition by MacChesney et al. [33]. They theorized that their growth was stable under the conditions they used due to the ionized nitrogen involved in the reaction. Both studies also report synthesizing polycrystalline InN. Hovel and Cuomo grew on sapphire and silicon substrates and report room temperature resistivities of  $3\text{-}5 \times 10^{-3} \Omega\cdot\text{cm}$ , free electron concentrations of  $5\text{-}8 \times 10^{18} \text{ cm}^{-3}$  and mobilities of  $250 \pm 50 \text{ cm}^2\text{V}^{-1}\text{s}^{-1}$  [34]. Puychevri r and Menoret [35] grew InN using the same method on glass and quartz substrates and report resistivities of  $10^{-3}\text{-}10^{-2} \Omega\cdot\text{cm}$ , and mobilities on the order of  $50 \text{ cm}^2\text{V}^{-1}\text{s}^{-1}$ . They also reported a bandgap of 2.07 eV at room temperature.

InN was formed through the nitridation of InP in 1980 by Yamaguchi [36]. In this work InP wafers were heated in an ammonia at 1 atm for times ranging from 1 hour up to 64 hours. He then studied the thickness of the InN layer as a function of nitridation time and temperature, noting a linear relationship between the nitridation time and temperature below 590°C. At 590°C and 620°C layer thickness initially increased with time but then the layer thickness started following a quadratic curve (Figure 1-3), correlated with decomposition of InN observed by MacChesney et al. [33]. Yamaguchi also studied current-voltage and capacitance-voltage relationships of InN in a metal-insulator-semiconductor (MIS) arrangement finding resistivities on the order of  $10^{11}$  to  $10^{12} \Omega\cdot\text{cm}$ .



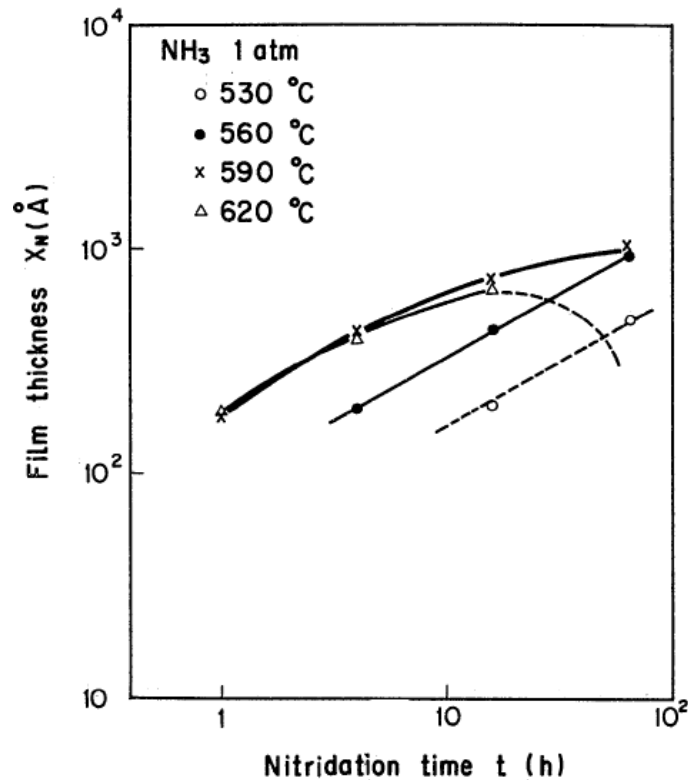


Figure 1-3 InN film thickness as a function of time for the nitridization of InP [36]

The 1980s brought reports of multiple investigations of the optical, [37–39] structural, [40,41] and electrical [42] properties of InN grown by sputtering. The InN bandgap was again updated by Tansley and Foley as 1.89 eV [37]. They also measured mobilities of  $5000 \text{ cm}^2 \text{V}^{-1} \text{s}^{-1}$  [42]. Work was also done to formalize the theory of the band structure of InN [43,44]. In 1988, Sullivan and Parsons were first to report on the optical properties of InN grown by DC-sputtering and they specify a bandgap of 1.7 eV [38]. Westra et al. analyzed the impurities present in DC-sputtered InN determining an oxygen content of 11% [45]. They were concerned with the formation of  $\text{In}_2\text{O}_3$  and determined that it was not present at this level of contamination. Westra et al. also measured carrier concentrations of  $7 \times 10^{19} - 2 \times 10^{20} \text{ cm}^{-3}$  and mobilities of  $4 - 10 \text{ cm}^2 \text{V}^{-1} \text{s}^{-1}$  [45]. They noted no significant differences from previously reported values [34,35,46]. The end of the 1980's brought about the first mention of the epitaxial growth of InN by microwave-excited

metalorganic vapor phase epitaxy (MOVPE) by Wakahara and their collaborators [47–49]. They grew InN on sapphire substrates between 400 and 600 °C using the metalorganic precursor TriMethylIndium (TMI) and microwave excited N<sub>2</sub>. Tansley et al. [50] proposed another method of growth called photodissociative deposition, in which light energy is used to break down ammonia so that GaN and InN could potentially be grown at the same temperature as InN.

In 1989 the Johns Hopkins Applied Physics Laboratory published a summary of “Metal Nitride Semiconductors for Optical Applications” [51]. This was published right before the volume of publications regarding group III-nitrides drastically increased in the 1990s.

In 1991 and 1992 a novel method of interacting ion beams was used to fabricate InN. However their results did not demonstrate good quality growth nor stoichiometrically correct InN [52,53]. Guo et al. [54] repeated studies on the thermal stability of InN, this time using monocrystalline InN generated by microwave-excited MOVPE. They held the InN in an N<sub>2</sub> atmosphere and produced similar results to MacChesney et al. [33], with InN decomposing through the desorption of nitrogen, above temperatures of 550°C. Hoke et al.[55] also introduced the concept of plasma assisted molecular beam epitaxy (MBE) for the formation of InN in 1991, growing InN on GaP at 350°C.

In 1993 Munoz and Kunc [56] predicted the rock salt phase and zincblende structures for InN based on calculation and experiments on GaN and AlN by others, seemingly unaware that earlier that year Strite et al. [57] grew InN, using plasma assisted MBE, that demonstrated the first instance of the zincblende structure. In 1994 the rock salt phase was found experimentally [58]. In 1994 Grzegory et al. documented the formation of 50 μm InN crystallites by the nitridation of indium at high pressures (20 kBar). Growth temperatures needed to be outside the stable parameters found previously for this process to yield InN.

The metalorganic chemical vapor deposition (MOCVD) growth of InN was first reported by Yamamoto et al. They deposited InN on silicon and sapphire at temperatures of 450°C and pressures of 76 and 760 Torr. Yamamoto et al. also attempted two stage growth, a thin layer deposited at 76 Torr followed by the main deposition at 760 Torr [17]. This method demonstrated their best results in crystal quality according to reflection high-energy electron diffraction (RHEED) as can be seen in Figure 1-4.

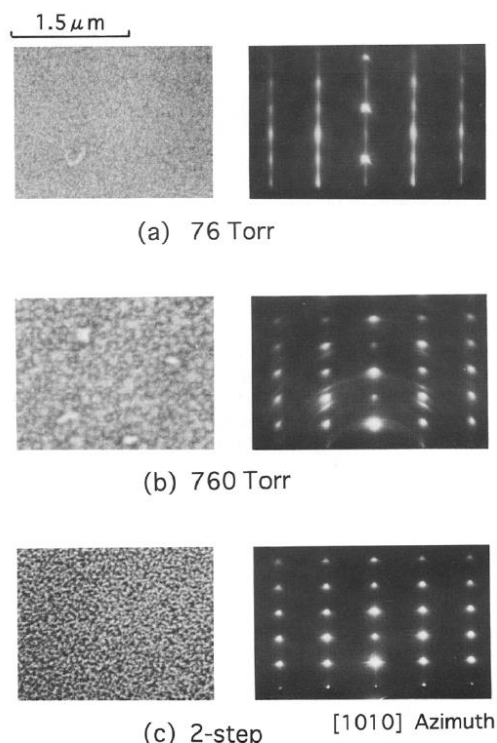


*Figure 1-4 SEM photograph and RHEED patterns for growth of InN by MOCVD [17]*

Sato and Sato [59] reported the growth of InN by hydride vapor phase epitaxy in 1994 that they described as “similar to those of most other reports”. They grew InN on sapphire at temperatures of 440 to 530 °C. For a more thorough review of group III-nitride growth through this point, please see Neumayer and Ekerdt [60]. A theoretical study at this time also predicted the

mobility of InN to be  $30000 \text{ cm}^2\text{V}^{-1}\text{s}^{-1}$  [61], making InN an attractive material to study and potentially commercialize.

Atomic layer epitaxy was then reported in 1995 by Inushima et al. [62], growing 280 nm of InN in 11 hours. Growth was performed under atmospheric pressure at 440 °C. The concept of nitridation of InP was revisited by Ren et al. [63] and Pan et al. [64]. They bombarded InP with ionized atomic and molecular nitrogen, respectively. Ren et al. demonstrated the presence of InN that was polycrystalline and non-uniform. Pan et al. were also able to synthesize InN and demonstrated a negative relationship between nitridation and angle of incidence of the  $\text{N}_2$  ion beam but no change in nitridation as a function of ionization energy in the range they studied [64]. Sato and Sato [65] also refined RF-sputtering using atomic nitrogen plasma, stating that there is no surface degradation compared to other plasma sources.

In 1996 Ambacher et al. [66] revisited the stability of InN, and other III-nitrides. This time the study used InN grown by MOCVD. Polycrystalline InN and epitaxial GaN and AlN were heated up in a vacuum and the desorption from the surface was monitored. They reiterate that the nitrogen partial pressure required to maintain stable InN increases exponentially above 630 °C.

Reports were made in 1999 of growth on molten indium [67], and sputtering growth of InN at temperatures as low as 100°C [68]. Pulsed laser deposition (PLD) was also explored and produced lower unintentional doping [69]. The idea of breaking down the ammonia by pre-heating it in MOCVD was suggested [70], and the concept of migration-enhanced epitaxy was proposed by Lu et al. [71] based on work done by Horikoshi on GaN [72]. In 2001 Cumberland et al. [73] demonstrate a method of solid-state production of InN. In their work they reacted  $\text{InI}_3$ ,  $\text{Li}_3\text{N}$ ,  $\text{LiNH}_2$  and  $\text{NH}_4\text{Cl}$  through an exothermic reaction inside a heat-dissipating reaction cell to avoid decomposition.

In 2002, the interest in InN was reignited with the bandgap of InN being measured at 0.69 eV at 300 K [74] (see **Error! Reference source not found.**). This finding sparked controversy, as authors claimed that the bigger bandgap previously reported was due to polycrystalline or poor quality material. Wu et al. [75] published an article in support of a narrower bandgap, and Butcher et al. [76] continued with reporting larger bandgap material. Qian and collaborators [77,78] published work on Infrared reflectivity and Raman results and also cited the larger bandgap.

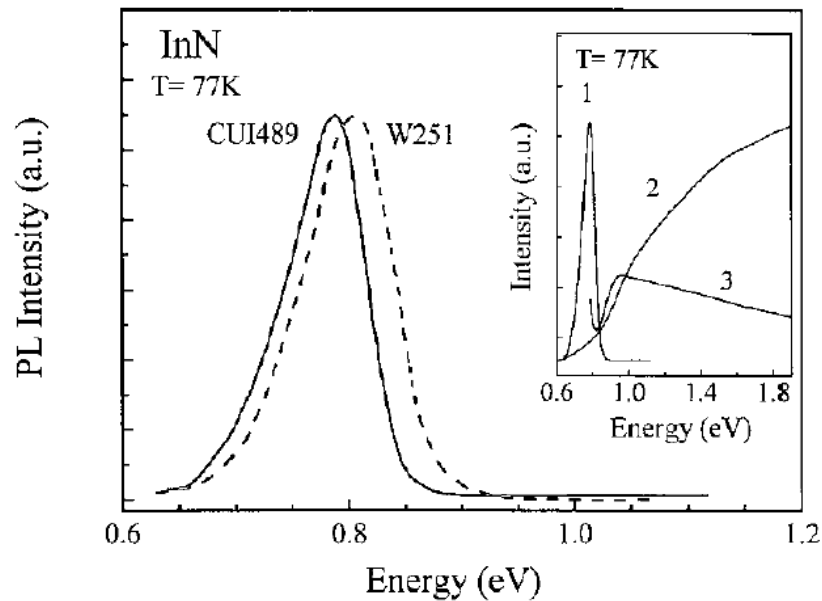


*Figure 1-5 Photoluminescence spectra of InN grown by metal-organic MBE (solid line carrier concentration of  $9 \times 10^{18} \text{ cm}^{-3}$ ) and plasma assisted MBE (dashed line carrier concentration of  $1.2 \times 10^{19} \text{ cm}^{-3}$ )[74]*

Nag [79] made a very convincing argument against what has since become the accepted value. He based his theory on the relationship between electron effective mass and the bandgap exhibited by II-VI and III-V materials. Butcher again visited the controversy in 2005 [80], demonstrating clearly that for MBE grown InN the bandgap appears to be  $\sim 0.7 \text{ eV}$ , and bandgaps that had been reported

above that most likely originate from the Moss-Burstein effect [81], the shifting of the absorption edge due to free electrons occupying the lowest conduction levels.

Other refinements to growth have been made, such as laser break down of the ammonia in MOVPE [82], and the addition of a two-step process to grow a buffer layer to aid lattice transitions [83]. The next big development in the InN growth techniques was the MOCVD modification to grow material at high-pressure [84]. Typical pressures achieved in such systems are 1 to 19 Bar, which expands the InN growth parameter window to higher growth temperatures [84–87]. Ruffenach et al. also give a review of the changes in MOVPE (MOCVD) growth that are very beneficial to this work [88]. They also cite the issue of hydrogen contributing to the decomposition [89,90] and doping [91] of InN.

The work outlined above shows that there is a significant interest in the growth of InN. InN has been produced at sufficiently good quality to find a bandgap of 0.7 eV and develop nanostructures that are of research interest. However, the problem of achieving commercially viable growth rates for epitaxial film and growing InN at growth parameters similar to GaN and AlN still exists.

## **1.2 Physical structure of the group III-nitrides**

Group III-nitrides are most commonly found to have the wurtzite crystal structure. However, these materials can also be found in a zincblende [57,92] and rock salt form [58,93–95]. The wurtzite structure is a hexagonal close-packed lattice with a two atom basis. A representation of the structure can be seen in Figure 1-6.

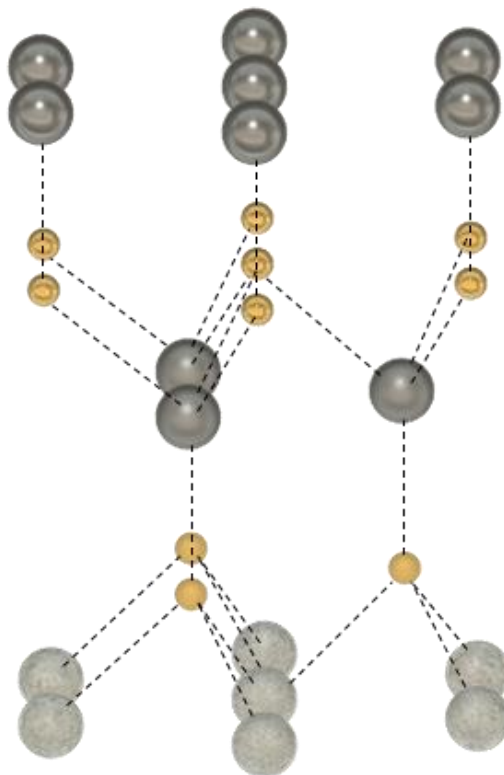


*Figure 1-6 Representation of Wurtzite structure. Grey spheres represent the group III metal, small yellow spheres represent nitrogen. Dashed lines represent III-metal – N bonds. Shading represents different layers.*

The unit cell of the crystal contains 4 atoms as shown in Figure 1-7. The wurtzite structure belongs to the  $C_{6v}^4$  point group in Schoenflies notation ( $P6_3mc$  in Herman-Mauguin notation). This means the crystal has six-fold rotation symmetry in the plane and six mirror planes that contain the rotation axis. However, this does not apply to the entire crystal structure. The Herman-Mauguin notation better identifies the space group by adding the screw component of the rotation necessary

to accurately describe the crystal and by specifying the presence of a translational symmetry perpendicular to the  $c$  axis.

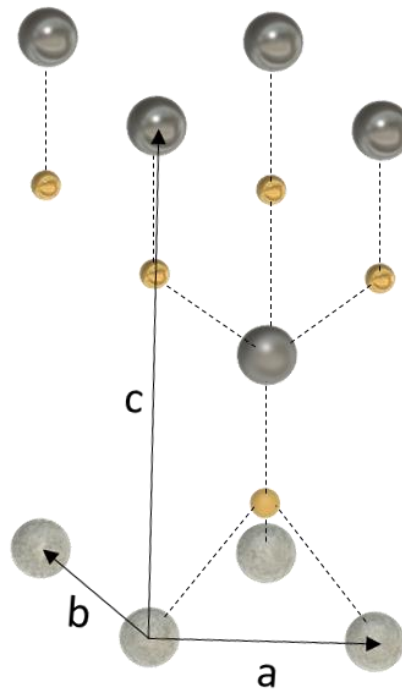


*Figure 1-7 Unit cell for group III-Nitrides/wurtzite structure, showing  $a$ ,  $b$  and  $c$  vectors, in the wurtzite structure the magnitude of  $a$  and  $b$  are the same.*

The lattice constants  $a$  and  $c$  of the group III-nitrides are listed in the Table 1-1 below.

*Table 1-1 Lattice constants for aluminum, gallium and indium nitride*

Material	$a$ (Å)	$c$ (Å)
Aluminum Nitride [96]	3.111	4.981
Gallium Nitride [97]	3.189	5.185
Indium Nitride [98]	3.539	5.708

As can be seen from Table 1-1, the increase in atomic mass of the group III metal is associated with an increase in lattice spacing as would be expected.



The  $C_{6v}^4$  group can be represented by a sum of four irreducible representations - two A1, two B1, two E1 and two E2 representations. In a character table for this group the only linear modes are A1, E1 and E2, and we would expect this to correlate with the optically active resonances, assuming the correct light polarization as discussed in sections 2.2.3, 3.3.1 and chapter 4.

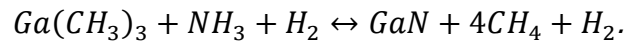
### 1.3 Growth of group III-nitrides

InN and GaN growth has evolved from the fabrication of powders by melting indium (or gallium) in flowing ammonia to plasma-assisted molecular beam epitaxy (PA-MBE), in which the group III metal is melted and moved to a target where it can interact with ionized nitrogen from a plasma source, effectively growing a monolayer of material at a time to produce bulk materials.

A more common method used in semiconductor manufacturing is chemical vapor deposition (CVD). In this method, precursor chemicals for both the group III metal and nitrogen are carried in a pneumatic system from their respective reservoirs to a reaction chamber where the substrate for deposition is held at conditions favorable for a precursor decomposition and chemical reaction to form the desired material.

#### 1.3.1 Metal-Organic Chemical Vapor Deposition (MOCVD)

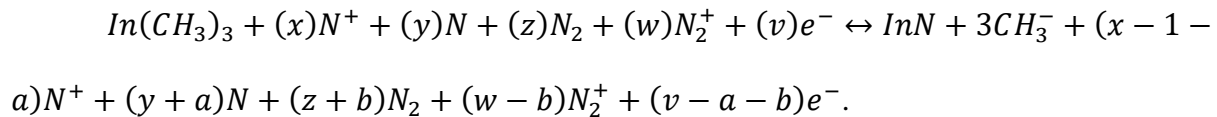
In MOCVD the metal precursor for the growth of group III-nitrides is typically the metal attached to three methyl or ethyl groups, although other metalorganics do exist. The precursor of nitrogen is typically ammonia. In this case for the stoichiometry of the reaction hydrogen is also necessary in the growth reactor to facilitate the reaction. The chemical reaction for the MOCVD growth of GaN can be written as follows:



For this reaction to be balanced toward producing GaN, the partial pressure of all the reactants and temperature at the substrate surface need to be controlled so that it is kinetically favorable for GaN to form. And if a specific form of GaN is desired, refinements to those pressures and the temperature and feed-rates of the precursors will need to be made. This process is typically and effectively used for growth of AlN and GaN. These chemical reactions occur at fairly fast rate, and film growth rates on the order of 1  $\mu\text{m/hr}$  have been observed. GaN is also grown at pressures of around 100 Torr in MOCVD which is another advantage of this growth technique over MBE, which requires ultra-high vacuum conditions. While the high growth rates and relatively high growth pressure are distinct advantages of MOCVD over MBE, the large parameter space available to MOCVD makes the growth process more challenging to establish.

### ***1.3.2 Migration Enhanced Plasma Assisted (MEPA-) and Plasma Assisted (PA-) MOCVD***

The use of ammonia in the growth of materials using MOCVD can be another limiting factor, particularly for InN, as it may release hydrogen which is associated with decomposition and high carrier-concentration [89–91]. Ammonia is also a very inefficient source of nitrogen for InN as its decomposition rate is very low at the temperatures normally used to synthesize InN [99]. Another method of obtaining nitrogen for reaction is to introduce ionized nitrogen directly into the growth reactor using nitrogen plasma. This growth technique is called plasma assisted MOCVD (PA-MOCVD). Using ionized nitrogen as precursor can also simplify the chemistry at the substrate surface. In this case the reaction becomes:



In this reaction molecular nitrogen is ionized, forming molecular ions, atomic nitrogen, atomic nitrogen ions, and the electrons that were stripped to make the ions. The only chemistry happening is the dissociation of the indium from the methyl groups to bond with the atomic nitrogen ion. According to Ahmad et al. [100] the atomic ions are main plasma species that react with the indium once it dissociates. The other species present in the growth reactor are, at this point, not understood to affect the reaction.

Now as well as the partial pressures and temperature associated with a reaction in the direction of InN, we also need to consider the relative concentrations of ions introduced by the plasma source. While the InN synthesis chemistry may be easier, considering the additional variables introduced by the plasma does not simplify the physics of this problem. It may however be a way to shift the reactions into a different growth regime due to different energies associated with the constituents of the reaction.

The concept of migration enhancement is to allow more time for the migration of reactants to energetically favorable positions on the growth surface. This could improve the material quality before completing the reaction and stabilizing the surface [71]. In this method, the two precursors are alternately placed on the substrate. Typically, the metalorganic (MO) precursor, such as TMI, is injected into the growth system and approaches the substrate. High substrate temperature supplies sufficient thermal energy to dissociate In from the methyl groups. Free In atoms then migrate on the growth surface to find a bonding site. After completion of the In monolayer growth, the nitrogen is then injected into the reactor, and the nitrogen can bind with the indium to stabilize and join the crystal structure of the material. This process is what gives migration enhanced plasma assisted MOCVD (MEPA-MOCVD) its name, and it is the experimental process that I will be exploring in this work.

## 1.4 Dissertation overview

The rest of this dissertation will be split into three portions. Chapter 2 will discuss the methods for growth and characterization. Chapter 3 and chapter 4 will discuss the work carried out for this dissertation. Chapter 3 will cover the analysis done of InN samples grown at 750 – 957 °C that lead to the conclusion that, using MEPA-MOCVD, InN could be grown above previously reported decomposition temperatures. Chapter 4 will detail the method of modelling Infrared reflectance to better characterize GaN/AlGaIn heterostructures, and InN, and the downfalls of current models. Chapter 5 summarizes the findings in chapters 3 and 4 and provides some ideas for future directions of study.

## 2 EXPERIMENTAL METHODS

InN films were grown on sapphire or GaN substrates using migration enhanced plasma assisted MOCVD or plasma assisted MOCVD. For InN grown on GaN, an approximately 1500 nm undoped GaN template grown by MOCVD was used for as a substrate. After fabrication GaN templates and InN films were characterized using Raman spectroscopy, optical microscopy, FTIR reflectance spectroscopy and near UV-visible near-normal incidence spectroscopy. If samples are of particular interest, the surface of the sample was characterized with atomic force microscopy (AFM), and X-ray diffraction (XRD) was used to get a better measure of its crystallinity. This chapter will give a summary of both the growth and the measurement techniques used in this study.

### 2.1 Sample growth

#### 2.1.1 MOCVD growth system

The growth of group III-Nitrides is complicated by the lack of an affordable lattice matched substrate. GaN is one of the substrates that provides the closest lattice matching for InN growth. GaN templates were grown in the MOCVD growth system using a two-step process [101]. C-plane sapphire substrates with a 0.2° offcut were used to promote growth and surface quality [102,103]. There are commercially available c-plane GaN templates as well as single-crystalline substrates, but currently they are prohibitively expensive for general experimentation.

A modified Emcore/Veeco D125 reactor was used for MOCVD growth of GaN templates. A schematic of the growth reactor is shown in Figure 2-1. The modifications included a wafer carrier that can hold three 2-inch diameter wafers. Sapphire wafers (or samples to be overgrown) are placed in the wafer carrier in the load-lock. The load-lock is flushed with N<sub>2</sub> and evacuated three times to reduce oxygen contamination in the reactor. After the load-lock is finally pumped down to match the pressure in the growth reactor the load-lock gate valve is opened to transfer the

loaded wafer carrier into the reactor to be placed on the spindle. The resistive substrate heater elements are placed below the wafer carrier, concentric with the spindle. A heatshield placed below and around the heater is used to protect the chamber from radiative heat as well as to protect the heating element from material deposition. The heater can heat the wafer carrier to temperatures of 1150 °C. The heater is made of two resistive elements that are separately controlled to heat the inner and outer region of the wafer carrier to control the uniformity of surface temperature across a wafer.

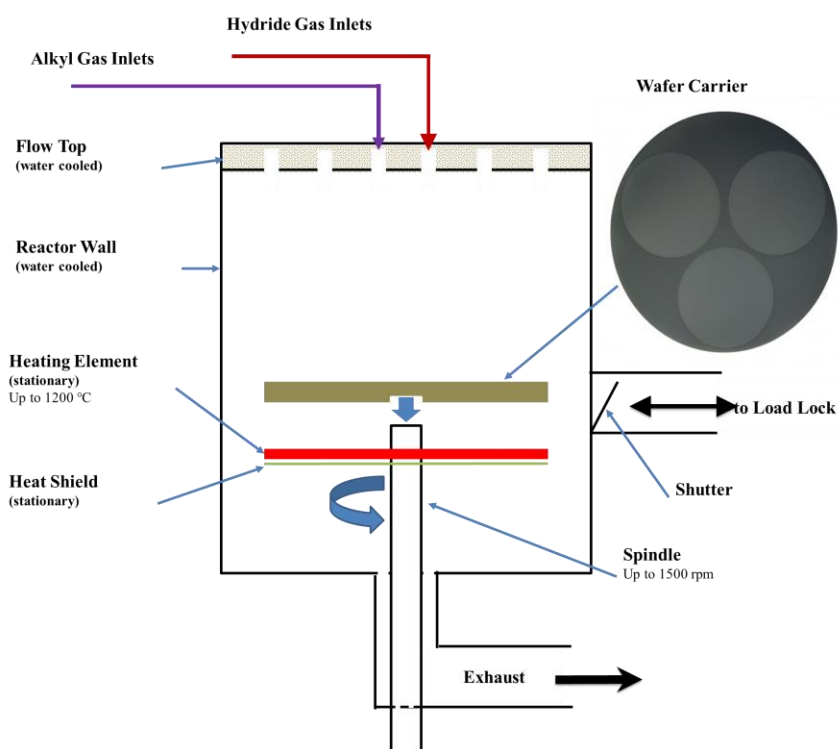


*Figure 2-1 Sketch of modified Emcore/Veeco D125 MOCVD reactor*

The spindle can reach rotation rates of 1500 rpm. Rotating the wafer carrier at this rate during the growth process defines the precursor gas flow dynamics. A boundary gas layer rotating with the wafer carrier is formed above the wafer, in which the chemical reaction to form the film occurs. InN precursor gasses are flowing into the growth reactor through a showerhead - a gas

distribution plate with holes for gas flow into the reactor that are staggered to control the flow distribution. There are two showerheads at the top of the reactor. The top showerhead is for the ammonia and hydrogen. Nitrogen is also injected through it to ensure proper flow rates in the reactor. It has three separate sets of nozzles, grouped to control the radial distribution of the flow. The lower showerhead controls metal-organic and carrier gas distribution. It is divided into two different sets of nozzles grouped to control the radial distribution as well. Each gas line is equipped with flow control valves, shut-off valves, and flowrate sensors to monitor and control the flow. The metal-organic precursor (Tri-methyl gallium, TMG, for the growth of GaN) is carried to the reactor by a flow of  $N_2$  that is bubbled through the liquid TMG stored in a chiller to control its evaporation rate.

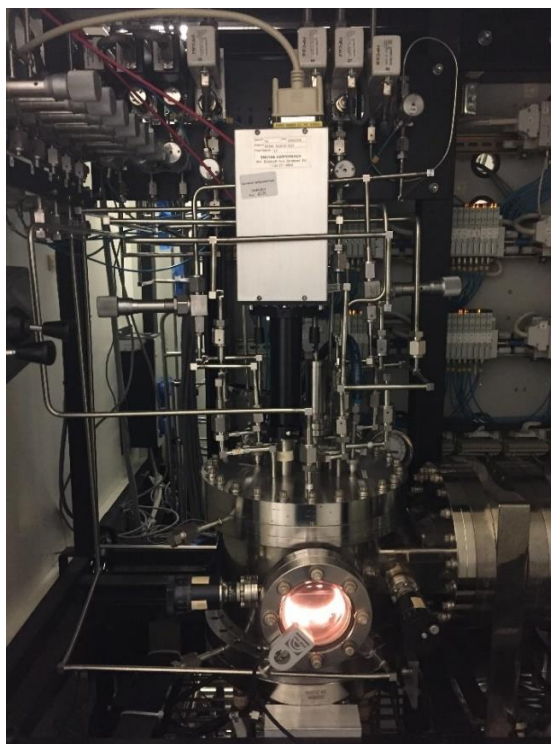


*Figure 2-2 Picture of MOCVD Reactor showing gas tubing and optical pyrometer entering the top of the reactor. The large tube off to the right is the gate valve toward the load-lock.*

The growth process is schematically shown in Figure 2-3. In this process the precursors are carried to the top of the boundary layer. At this point the MO,  $NH_3$  and  $H_2$  start interacting due

to the added thermal energy from the heated substrate carrier. The added energy causes the breakdown of some of the MO and the separation of nitrogen from some of the ammonia, allowing the chemical reactions to occur to stabilize the resulting methyl groups into methane and to form bonded III-N groups that can find energetically favorable sites on the substrate to adsorb to. Another parameter that can be controlled is the rotation rate of the substrate carrier. This rate will control the thickness of the boundary layer, regulating the time for chemical reaction and adsorption into the crystal structure.

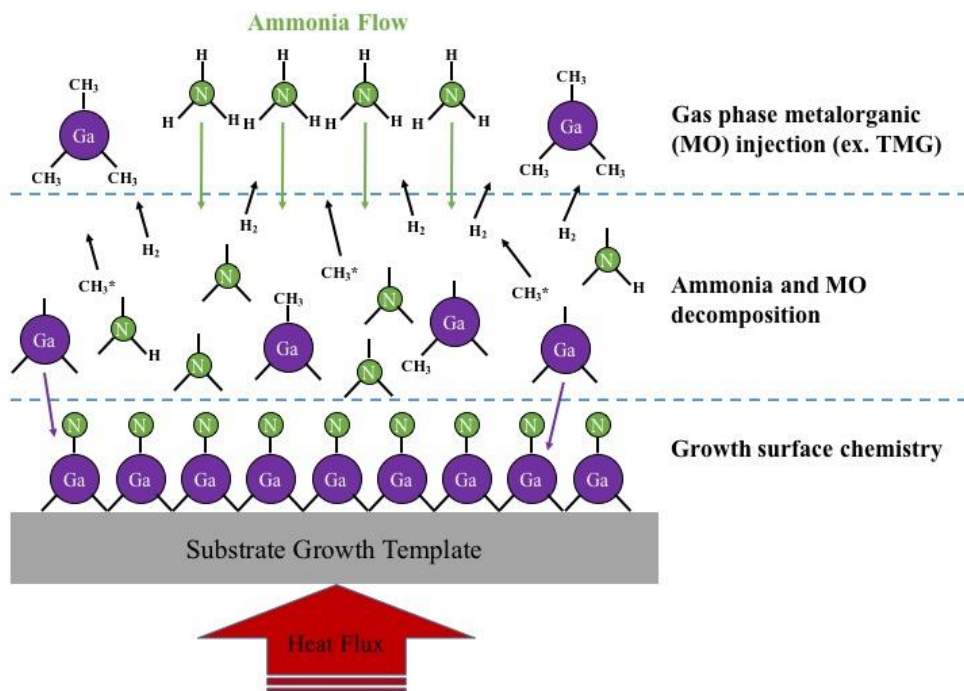


*Figure 2-3 Growth reaction diagram at substrate surface for GaN*

Three temperature sensors are used to measure the substrate temperature. Two thermocouples placed between the heatshield and the wafer carrier provide control feedback. The third temperature measurement is made by an optical pyrometer mounted at the top of the reactor, measuring the surface temperature of the wafers. The pyrometer is used to measure the actual



sample temperature during growth. The growth system is also equipped with an optical sensor that measures the reflectance of the wafers during growth to estimate sample thickness and growth rate.

Growth is monitored and controlled by a computer running proprietary software for the reactor. The typical process of GaN template growth runs as follows. The sapphire substrate is cleaned by heating it under a hydrogen flow to help reduce oxygen contamination on the wafer and in the reactor. Then the sample is heated to 1100°C to nitridate the surface, first under hydrogen flow to remove some of surface oxygen in the sapphire and then under nitrogen to fill those vacancies. A nucleation layer of GaN is then deposited on the nitridated sapphire at about 520°C and 675 mBar. Then the substrate temperature is raised to growth temperature to recrystallize the deposited GaN under an ammonia and nitrogen flow. While the pressure is still high the TMG flow is restarted to create a three-dimensional layer of GaN that can be overgrown. Finally, the pressure is dropped to growth pressure, about 260 mBar, and epitaxial growth is achieved, spreading out and overgrowing the 3-dimensional crystals grown on the nucleation layer. This process is documented from sensors monitoring the reactor and processes as shown for an example in Figure 2-4.

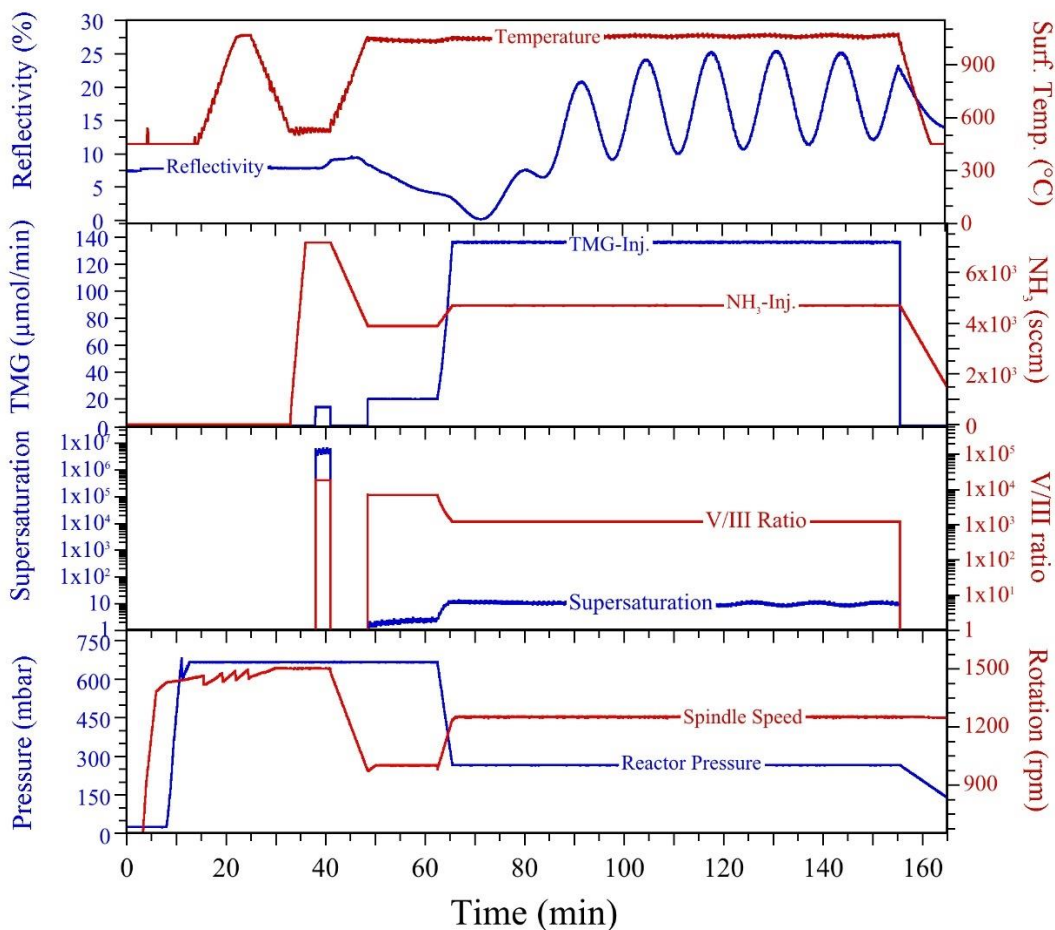
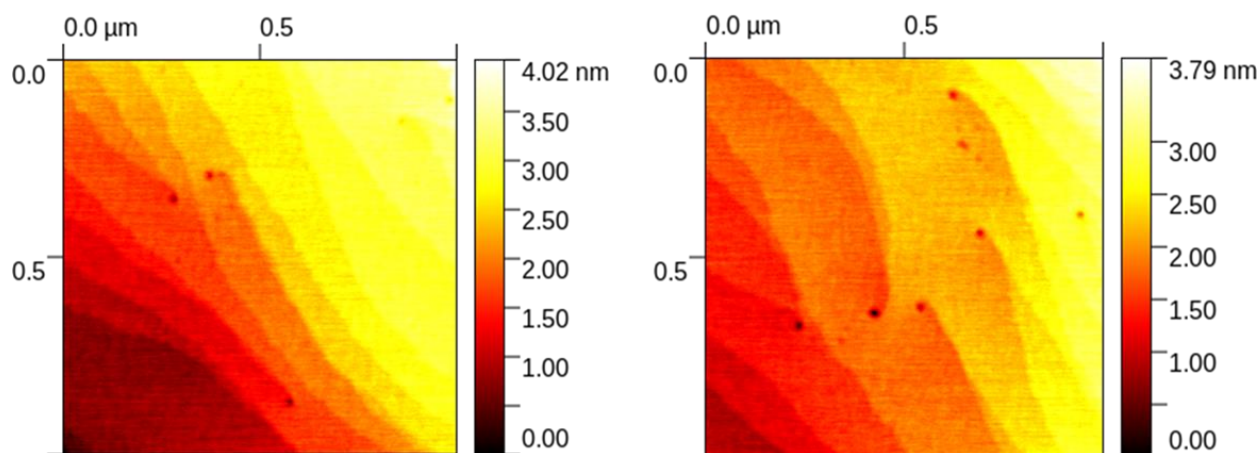


Figure 2-4 Growth control and feedback parameter plot recorded for a typical GaN growth run.

Atomic force microscopy scans of these GaN templates reveal an atomically flat surface with typical vicinal steps and screw-dislocation defects. The defect densities of  $\sim 10^8 \text{ cm}^{-2}$  in GaN templates grown as described above are favorable compared to similar commercially available templates. AFM images of GaN can be seen in Figure 2-5. These templates can now be used as substrates for other growth, such as device or experimental heterostructures. Since GaN and InN have the same wurtzite structure and the lattice mismatch is 9.9%, it also makes a good substrate for the growth of InN [104].



*Figure 2-5 AFM scans of GaN template grown on sapphire substrates by MOCVD.*

### **2.1.2 MEPA-/PA-MOCVD**

As can be seen in section 1.1, the growth of high quality InN is possible but challenging in MBE systems. The downsides of these systems are still the low growth temperature, incompatible with alloying with other III-nitrides, and growth rates that are not commercially viable.

In order to attempt overcoming the restriction in growth temperature necessary for alloying and in an attempt to increase deposition rates, I am exploring plasma as a source for ionized nitrogen, eliminating the need for ammonia and the high-temperatures associated with cracking it and the hydrogen that may degrade InN.

A custom-built reactor is used for migration enhanced plasma assisted (MEPA-), or plasma assisted (PA-) MOCVD in our facility (see Figure 2-6). Similar to the process for MOCVD, this reactor has a load-lock that the wafer carrier can be accessed through. This reactor is capable of using a 4-inch wafer carrier and usually is used with a wafer carrier that holds two 2-inch half-wafers. Nitrogen flushing and evacuation is also performed for purging and reducing oxygen

contamination in the reactor before the carrier is transferred to the reactor where it is placed on the spindle.



*Figure 2-6 Picture of the MEPA-/PA-MOCVD reactor showing the plasma source on top and load-lock and gate valve on the right*

This reactor has a single element heater. Temperature is controlled by setting the heater power. The substrate temperature was calibrated with a thermocouple placed in the center of the spindle that supports the wafer carrier. This thermocouple was calibrated to the sample surface temperature with the same pyrometer used in the MOCVD reactor.

The nitrogen precursor used for InN growth in this reactor is ionized nitrogen, generated by the MEAgrow plasma source with a 600 W 13.56 MHz RF power. Nitrogen gas flows through the plasma source, gets ionized, and injected into the growth chamber. The reactor also has two injection ports for other gases, typically used for hydrides, one at the exit of the plasma source and another just above the substrate. These are not in use for the projects described in this work. The MO inlet is a showerhead situated between the plasma source and wafer carrier. The MO is transported into the reactor by evaporation in a carrier gas, typically N<sub>2</sub>. The substrate carrier in

this reactor rotates at a slow rate of 20 – 30 rpm (as compared to the MOCVD system) to ensure even coverage, rather than to control the reaction near the surface. A schematic of this can be seen in Figure 2-7.

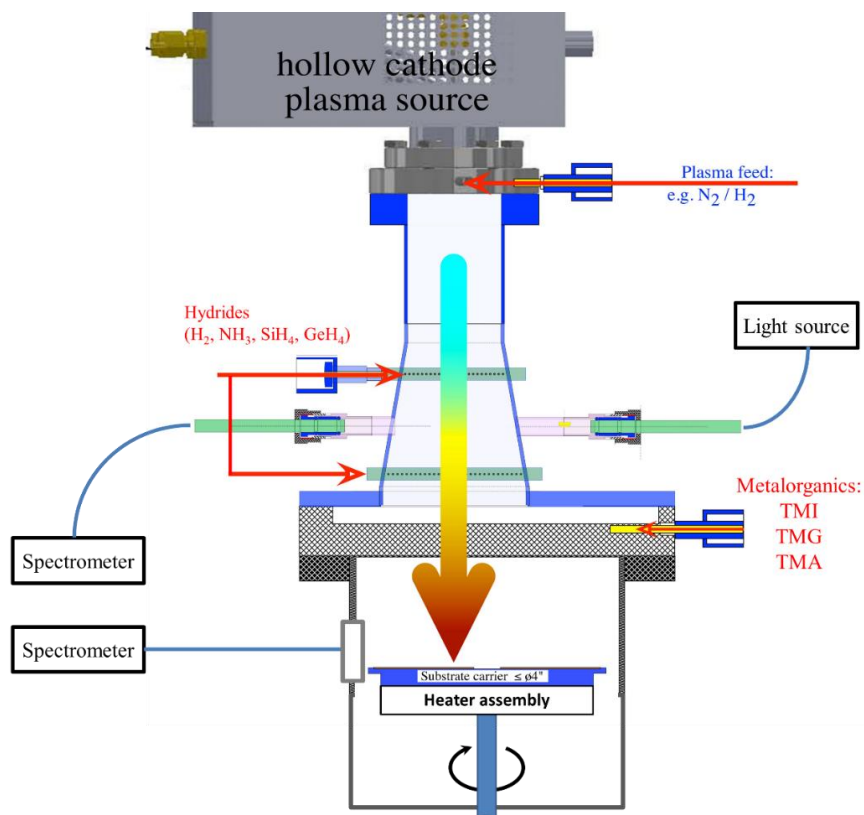


*Figure 2-7 Schematic of the MEPA-PA-MOCVD reactor*

The substrate carrier can be heated up to 1100°C. It provides necessary thermal energy to decompose the MO precursor (TMI). Ideally, in this reactor the precursor and ionized nitrogen will travel from their inlets and react at or near the substrate surface where the MO has the energy to decompose. This is a parameter that needs to be controlled, because theoretically the ionized gas could impart energy to the MO causing it to decompose above the surface and react with the available nitrogen forming III-N molecules in gas which may not have the energy to find ideal sites for adsorption onto the substrate. Methods to control the gas phase reactions include

decreasing the reactor pressure in order to increase the mean-free path of the precursors, or to alternate the injection of each precursor so they are spatially (and temporally) separated until they are deposited onto the substrate.

The reactor is also equipped with a wire grid whose potential relative to the wafer carrier can be controlled. For this work the grid was insulated from any connection and allowed to be at a floating potential. Optical access is also available to perform emission spectroscopy of the plasma or to measure transmission spectra across the reactor that can be used to determine the gas composition. Growth in this reactor will be discussed in Chapter 3 and is also discussed in literature [100,105–107].

## **2.2 Film Characterization**

After the samples are grown, information regarding the structure, surface quality and thickness need to be found in order to provide feedback on the growth. The sample is inspected with an optical microscope for micron-scale (and larger) defects. The Raman spectrum is measured to verify the crystallinity of the sample. UV-visible near-normal incidence spectroscopy is performed to get an estimate of sample thickness and roughness through modelling. FTIR spectroscopy is done to cross-check the UV-visible spectroscopy and Raman measurements or to find thickness and roughness if it cannot be found by UV-Visible spectroscopy. If a sample needs additional characterization, then X-ray diffraction (XRD) can be measured to analyze the crystal structure, and the surface can be measured using atomic force microscopy.

### ***2.2.1 Optical microscopy***

The first step in characterization is to visually inspect the sample. An optical microscope equipped with digital camera is used to capture images of the surface to identify any large defects. Defects that can be immediately identified using the microscope include strain-related cracking,

the deposition of clusters on the surface, large scale defects that are usually related to the substrate, and improper growth, and large-scale 3-dimensional structures. Example images of such defects are shown in Figure 2-8.

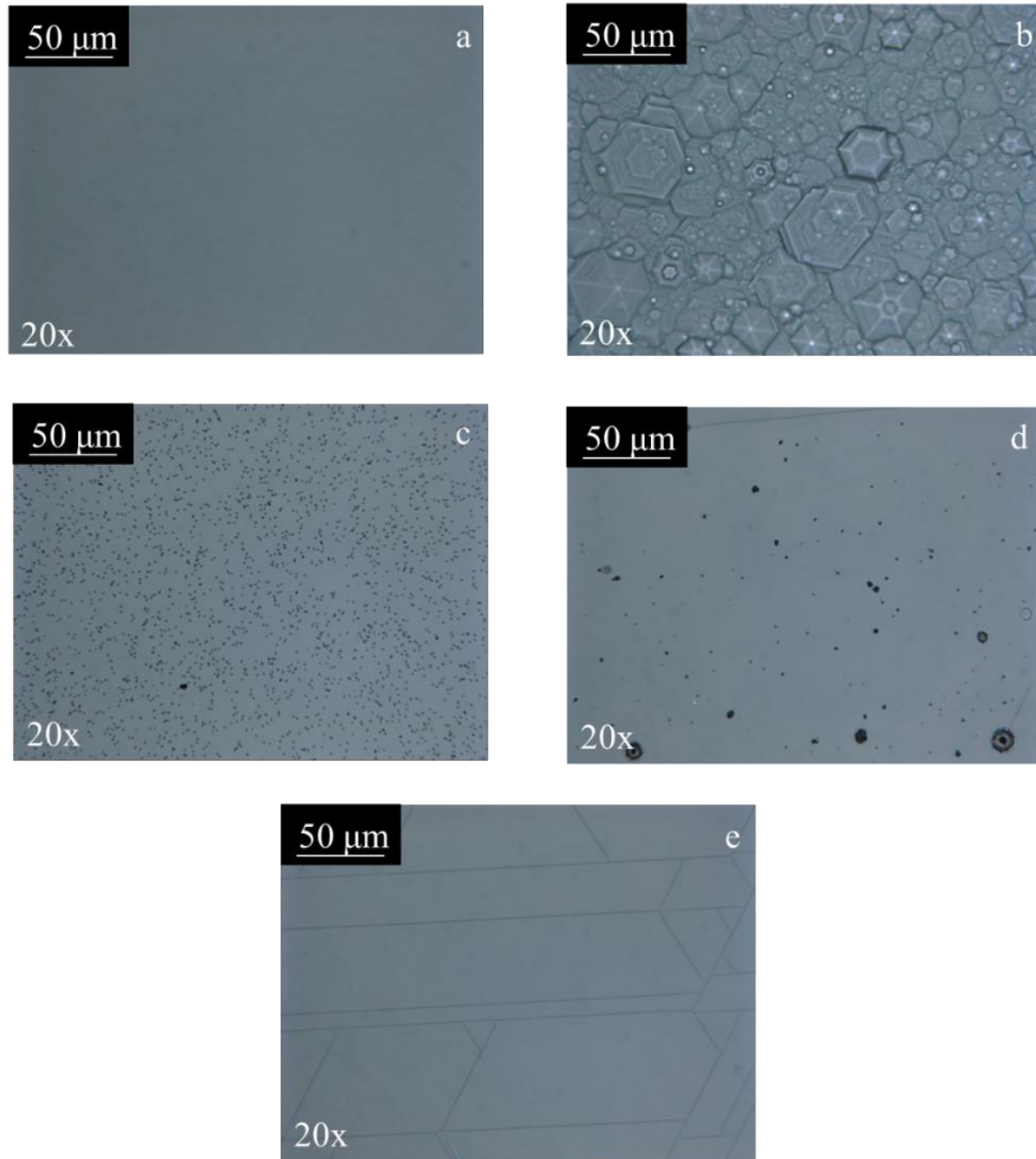


*Figure 2-8 Microscope images of GaN, InN and AlGaN. a) GaN without any visible defects. b) 3-dimensional growth of GaN. c) clustering on InN surface. d) substrate related defects creating imperfections in an AlGaN film. e) Strain cracking in AlGaN film.*

### 2.2.2 Reflectance spectroscopy

Reflectance data, when combined with modelling, can be used to find film thickness and surface and interface roughness. If appropriate models are used for the dielectric function, these models, when compared to data, can also provide information about the phonon modes of the material analyzed.

The interaction of electromagnetic waves with an interface can be described using the Maxwell equations.

$$\begin{aligned}\nabla \cdot \mathbf{B} &= 0 & \nabla \times \mathbf{E} + \frac{\partial \mathbf{B}}{\partial t} &= 0 \\ \nabla \cdot \mathbf{D} &= \rho & \nabla \times \mathbf{H} - \frac{\partial \mathbf{D}}{\partial t} &= \mathbf{J}\end{aligned}\tag{2.1}$$

Where  $\mathbf{D}$  is the electric displacement field,  $\mathbf{E}$  is the electric field,  $\mathbf{B}$  is the magnetic flux density (commonly called the magnetic field) and  $\mathbf{H}$  is the magnetic strength. The electric field is proportional to the displacement field,  $\mathbf{D} = \epsilon \mathbf{E}$  and the magnetic flux density is proportional to the magnetic strength  $\mathbf{B} = \mu \mathbf{H}$ , where  $\epsilon$  is the permittivity (also called the dielectric function) and  $\mu$  is the permeability of the material housing the field.

In order to simplify our understanding of this problem we assume that there is no charge on the surface, so  $\rho = 0$ , and that there are no currents for the field to interact with,  $\mathbf{J} = 0$ . We also assume that the fields take on the form  $Ae^{i(\mathbf{k} \cdot \mathbf{x} - \omega t)}$ .



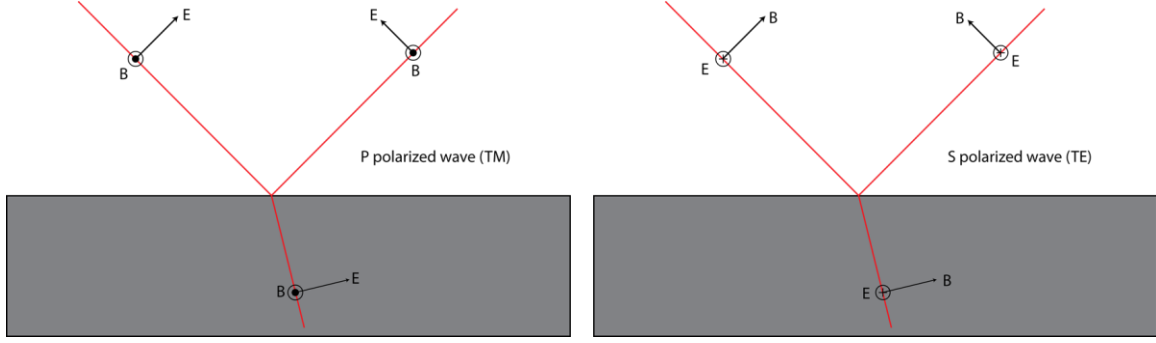


Figure 2-9 Schematic for an electromagnetic wave interacting with a material. Representations are provided for P (TM) and S (TE) polarization.

Figure 2-9 shows a schematic view of the interface we are discussing. The positive  $z$ -direction is toward the top of the page, the  $x$ -direction is to the right and  $y$ -direction is into the page, forming a right-hand basis. Material 1 is the top material and material 2 is on the bottom. For convention, each component of the fields discussed below are labeled as being in material 1 or 2 and travelling in the positive or negative  $z$ -direction.

Using the integral forms of the Maxwell equations shows us the surface-normal components of the net displacement and net magnetic field are the same on both sides of the interface. In equation form, we write  $D_{-z1} + D_{+z1} = D_{+z2}$  and  $B_{-z1} + B_{+z1} = B_{+z2}$ . Likewise the components of the electric field and magnetic strength parallel to the surface are also equal,  $E_{-x,y1} + E_{+x,y1} = E_{+x,y2}$  and  $H_{-x,y1} + H_{+x,y1} = H_{+x,y2}$ .

Using the exponential form of the fields, the two Maxwell equations with a curl can be simplified to

$$\mathbf{k} \times \mathbf{E} = i\omega\mathbf{B} \quad \mathbf{k} \times \mathbf{B} = -i\omega\mathbf{E} \quad (2.2)$$

so each component of the magnetic field can be rewritten as a function of the corresponding electric field.

$$\mathbf{B} = \frac{\mathbf{k} \times \mathbf{E}}{\omega} \quad (2.3)$$

Assuming the material is well oriented this generates six equations for the relationships between the electric and magnetic fields at the interface

$$\begin{aligned}
\epsilon_1 E_{-z1} + \epsilon_1 E_{+z1} &= \epsilon_2 E_{-z2} \\
(k_{x1} E_{-y1} - k_{y1} E_{-x1} + k_{x1} E_{+y1} - k_{y1} E_{+x1}) &= (k_{x2} E_{-y2} - k_{y2} E_{-x2}) \\
E_{-x1} + E_{+x1} &= E_{-x2} \\
E_{-y1} + E_{+y1} &= E_{-y2} \\
\frac{1}{\mu_1} (k_{y1} E_{-z1} - k_{z1} E_{-y1} + k_{y1} E_{+z1} + k_{z1} E_{+y1}) &= \frac{1}{\mu_2} (k_{-y2} E_{-z2} - k_{-z2} E_{-y2}) \\
\frac{1}{\mu_1} (k_{z1} E_{-x1} - k_{x1} E_{-z1} - k_{z1} E_{+x1} - k_{x1} E_{+z1}) &= \frac{1}{\mu_2} (k_{z2} E_{-x2} - k_{x2} E_{-z2})
\end{aligned} \tag{2.4}$$

It should be noted that  $k$  is a function of the material. Since  $v = \omega/k$  and  $v = (\epsilon\mu)^{-1/2}$ , solving for  $k$  gives:  $k = \sqrt{\epsilon\mu} \omega$ . We can also make some eliminations due to the wavevector having zero component in the  $y$ -direction and the  $x$ -component of the wavevector having to be the same above and below the interface (Snell's law),

$$\begin{aligned}
\epsilon_1 E_{-z1} + \epsilon_1 E_{+z1} &= \epsilon_2 E_{-z2} \\
E_{-x1} + E_{+x1} &= E_{-x2} \\
E_{-y1} + E_{+y1} &= E_{-y2} \\
\frac{1}{\mu_1} (-k_{z1} E_{-y1} + k_{z1} E_{+y1}) &= \frac{1}{\mu_2} (-k_{z2} E_{-y2}) \\
\frac{1}{\mu_1} (k_{z1} E_{-x1} - k_{x1} E_{-z1} - k_{z1} E_{+x1} - k_{x1} E_{+z1}) &= \frac{1}{\mu_2} (k_{z2} E_{-x2} - k_{x2} E_{-z2})
\end{aligned} \tag{2.5}$$

This leaves us with what seems to be five equations, and six unknowns. However, the electric field and wavevector in the z-direction and x-direction are geometrically linked to the field and wavevector respectively if there is a component of the field with p-polarization.

$$\begin{aligned}
\epsilon_1 E_{-1} \sin(i) + \epsilon_1 E_{+1} \sin(i) &= \epsilon_2 E_{-2} \sin(r) \\
E_{-1} \cos(i) - E_{+1} \cos(i) &= E_{-2} \cos(r) \\
E_{-y1} + E_{+y1} &= E_{-y2} \\
\frac{1}{\mu_1} (-k_{z1} E_{-y1} + k_{z1} E_{+y1}) &= \frac{1}{\mu_2} (-k_{z2} E_{-y2}) \\
\frac{1}{\mu_1} (-k_1 E_{-1} \sin^2(i) - k_1 E_{-1} \cos^2(i) - k_1 E_{+1} \sin^2(i) - k_1 E_{+1} \cos^2(i)) \\
&= \frac{1}{\mu_2} (-k_2 E_{-2} \sin^2(r) - k_2 E_{-2} \cos^2(r))
\end{aligned} \tag{2.6}$$

In this case, both the first and last equation are can be simplified to the same form, so we are left with four equations with four unknowns. We are also going to rename some variables for simplicity. The reflected (r) and refracted (transmitted) (t) electric fields are going to be renamed from  $E_{+1}$  and  $E_{-2}$  to  $E_r$  and  $E_t$ , and the  $E_{-1}$  to  $E_i$ , where  $i$  is for incident. The x-z field is going to be called the  $p$  field because of the parallel (p-)polarization, and the y field is going to be called the  $s$  field because of the perpendicular (s-)polarization, so the equations become

$$\begin{aligned}
\sqrt{\frac{\epsilon_1}{\mu_1}} (E_p + E_{rp}) &= \sqrt{\frac{\epsilon_2}{\mu_2}} E_{tp} \\
(E_p - E_{rp}) \cos(i) &= E_{tp} \cos(r) \\
E_s + E_{rs} &= E_{ts} \\
\sqrt{\frac{\epsilon_1}{\mu_1}} (E_s - E_{rs}) \cos(i) &= \sqrt{\frac{\epsilon_2}{\mu_2}} (E_{ts}) \cos(r)
\end{aligned} \tag{2.7}$$

These four equations can be solved together to form matrices for the reflected and refracted fields in terms of the incident fields. If the material is not oriented such that the material axes line up with the laboratory axes defined above then the dielectric can be considered a tensor, and all these above equations need to be adjusted appropriately.

Maintaining the assumption of appropriate sample orientation, matrix relationships for the reflected field and transmitted field at the interface can be derived. Those relationships can be found in chapter 4. This formulation follows the work of Jackson, Chapter 7 [108].

The coefficients found in this method that relate the reflected, refracted and incident light are called the Fresnel coefficients:

$$\begin{aligned} r_{s,p} &= \frac{E_{rs,rp}}{E_{s,p}} \\ t_{s,p} &= \frac{E_{ts,tp}}{E_{s,p}} \end{aligned} \tag{2.8}$$

The square of these values are the reflectance and transmittance at an interface respectively.

The reflectance of a sample can be directly measured as the intensity of light being reflected from a sample. Two instruments measuring reflectance were used to analyze the samples.

The first is a UV/visible spectrometer (Ocean-optics MAYA-2000) coupled with a bifurcated fiber to allow the coupling of a light source to illuminate a sample with one fiber and to collect light with the second fiber to the spectrometer. Due to the proximity of the source and collection aperture the collected light can be considered co-linear, so we direct the light along the surface normal to simplify analysis of the collected spectrum and eliminate the effect of

polarization on measurements. A sketch of the apparatus can be seen in Figure 2-10 and a picture of the apparatus can be found in Figure 2-11.

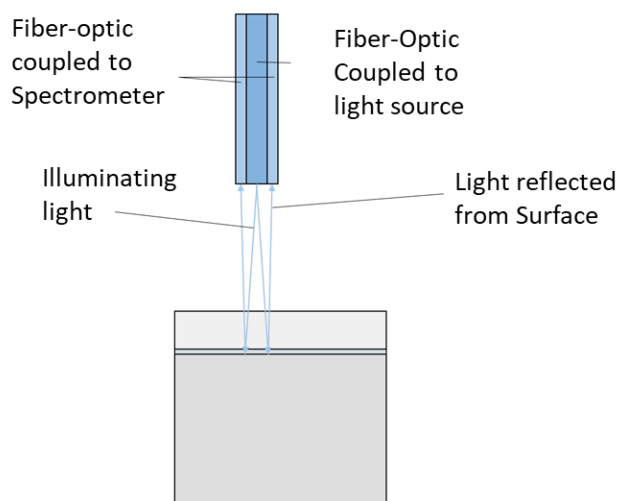


*Figure 2-10 Sketch of NIRS setup for collecting the elastic scattering of light at near-normal incidence*

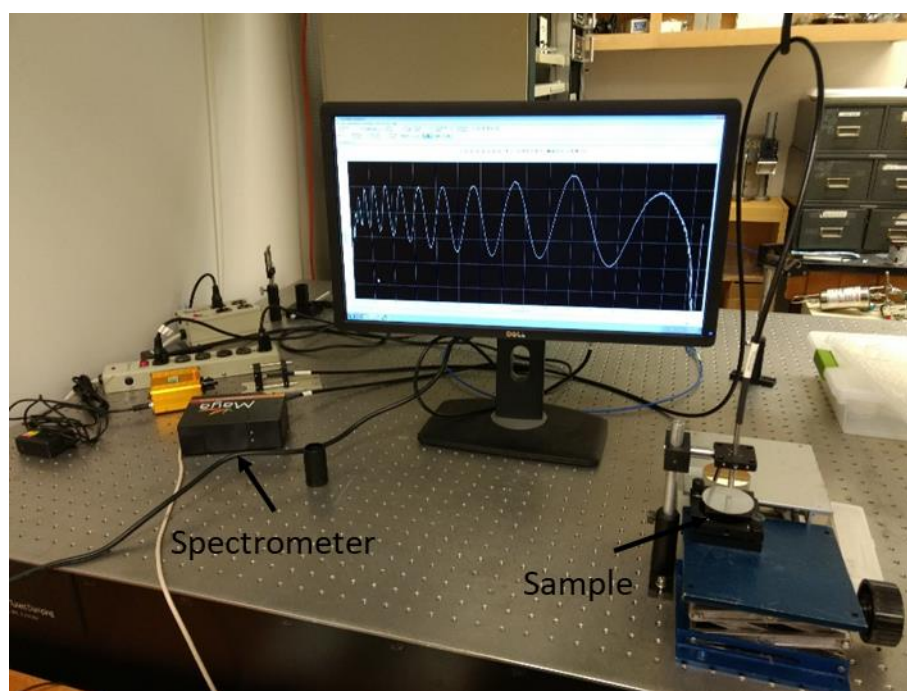


*Figure 2-11 Picture of apparatus for UV-visible near-normal incidence reflectance spectroscopy*

The second device to measure sample reflectance is a Thermo-Fisher Nicolet 6700 Fourier Transform InfraRed (FTIR) spectrometer. It is equipped with a Pike Map300 sample stage for measuring spectra at multiple locations on a sample consistently. The operating principle behind the FTIR spectrometer is that broadband light is used to illuminate the sample and the light reflected from the sample is then aligned with the incident light in an interferometer. One of the arms of the interferometer is actuated so that the light reaching the detector is the interference of the incident and reflected beam, while the path length of the incident is adjusted to obtain interference data in wavelength space, as seen in Figure 2-12. This data is then Fourier-transformed to convert the data to frequency space revealing the spectroscopic data.

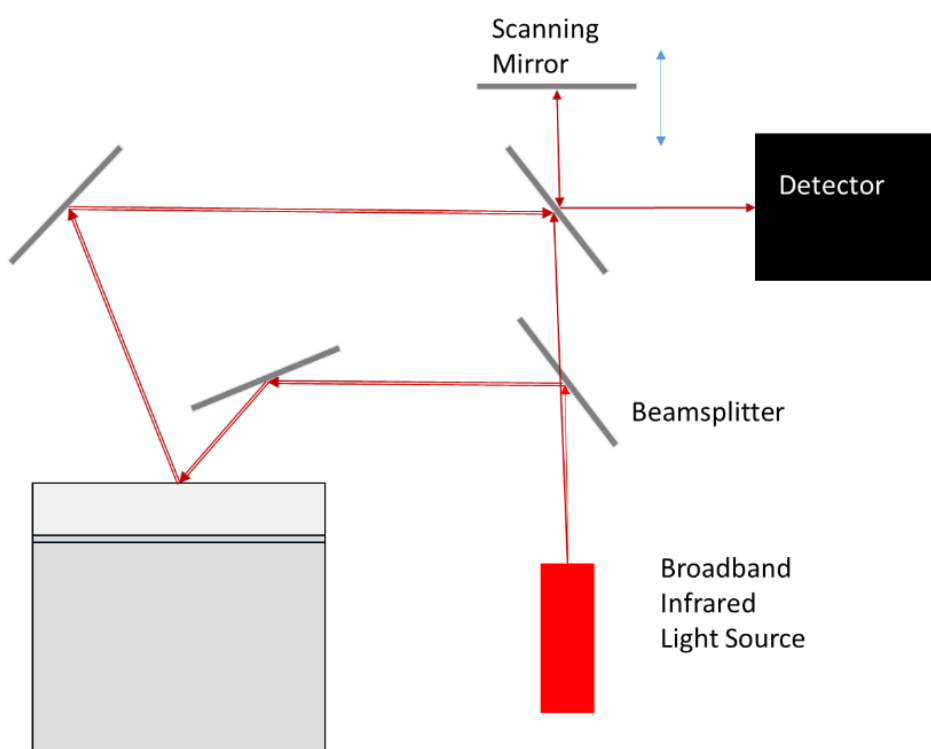


*Figure 2-12 Sketch of the mechanism of an FTIR spectrometer*

The FTIR spectrometer combined with the specified sample stage are capable of measuring sample reflectance or transmittance. Reflectance mode was used in the experiments described in

this thesis as all samples are grown on single-side-polished substrates. The light is incident on the sample at a fixed angle of  $20^\circ$ . In order to compensate for atmospheric absorption, a reference spectrum from a gold-plated mirror mounted at the same surface height on the sample stage is collected prior to each FTIR measurement.

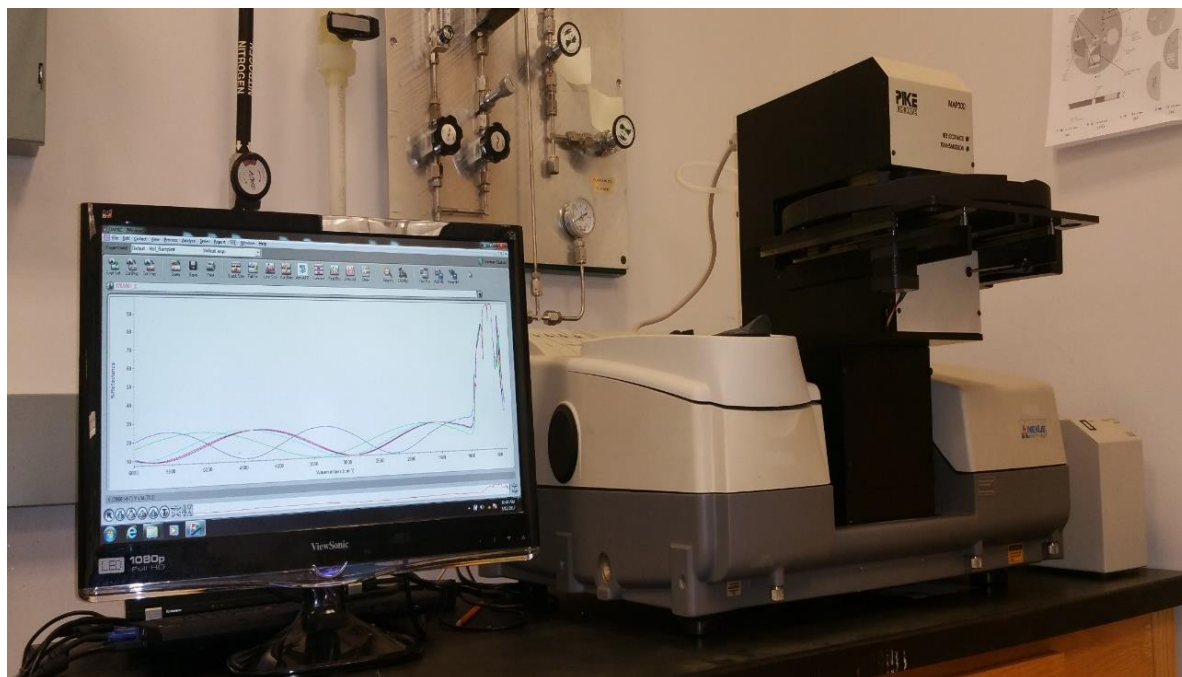


*Figure 2-13 Picture of the Nicolet 6700 FTIR spectrometer with Pike Map300 sample stage.*

### **2.2.3 Raman spectroscopy**

In order to verify the presence of the material of interest, we need to have some unique response that this material exhibits. The wurtzite crystal structure and lattice spacing of InN are unique, so if the effect of these were found we could state with certainty that InN is present on our sample.

Raman spectroscopy is a measurement of the inelastic scattering of light from a sample. Typically the light that we observe coming off a material is either reflected directly due to the interaction of light as discussed in section 2.2.2. or it is absorbed due to exciting the band gap and

due to an electron decaying back from the conduction band to the valence band. The light emitted is at the bandgap of the material. There is also another class of scattering called Stokes and anti-Stokes scattering.

Stokes scattering is the emission of light that is lower in energy than the absorbed light due to the non-radiative loss of energy to the excitation of a phonon mode or other vibration mode of a material. These phonon modes depend on the structure of the material. As we are energizing our material, the sample reflects elastically, but it also excites the vibrational modes of the bond in the crystal structure we are examining. The energy that is then scattered has decreased by the amount of energy necessary to excite the vibrational mode. This change in energy is called the Raman shift. The energy necessary to excite a phonon is unique to that phonon. If the Raman shifts for a certain material are found, then it can be concluded that material is present.

A Raman setup was constructed using a continuous frequency-doubled Nd:YAG laser, operating at 532 nm. The light from the laser was then focused using a 100x microscope objective directly onto the sample. Light reflected from the sample was collected using the same objective and then focused onto the entrance slit of the two-meter long monochromator. A step filter is placed in front of the entrance to monochromator to eliminate the elastically reflected light from the laser and any light with a higher energy, in other words, any wavelength shorter than 532 nm. Light is diffracted inside the monochromator with an 1800 lines/mm grating. The diffracted light is then collected on a liquid nitrogen cooled 1300 pixel wide charge-coupled device (CCD) array to store and analyze. A picture of the apparatus and sketch of the operating principle for the Raman spectrometer can be seen in Figure 2-14 and Figure 2-15.



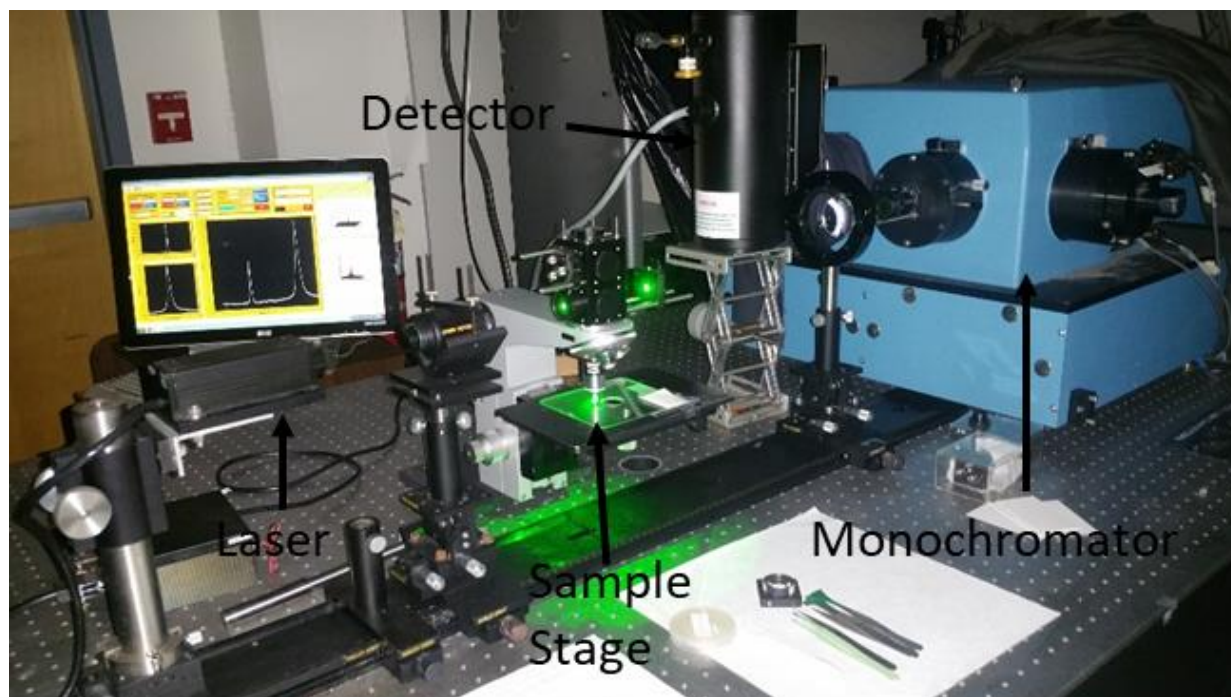


*Figure 2-14 Picture of custom Raman spectrometer*

Since the Raman spectrometer is a custom-built unit, it is essential that it is calibrated properly. I calibrated the spectrometer using the spectral emissions of helium and nitrogen discharge tubes. The two things that needed to be calibrated in the monochromator are the angle of the diffraction grating relative to the CCD, and the position of the beam center on the diffraction grating. In order to align the beam to the center of the diffraction grating, all filters were removed, and the ionized helium light source was placed at the entrance slit to the monochromator. The diffraction grating was rotated to measure each spectral line of the light. The difference, measured in pixels, between the center of the CCD and the measured spectral peak were collected to establish how the difference in position changed as a function of wavelength.

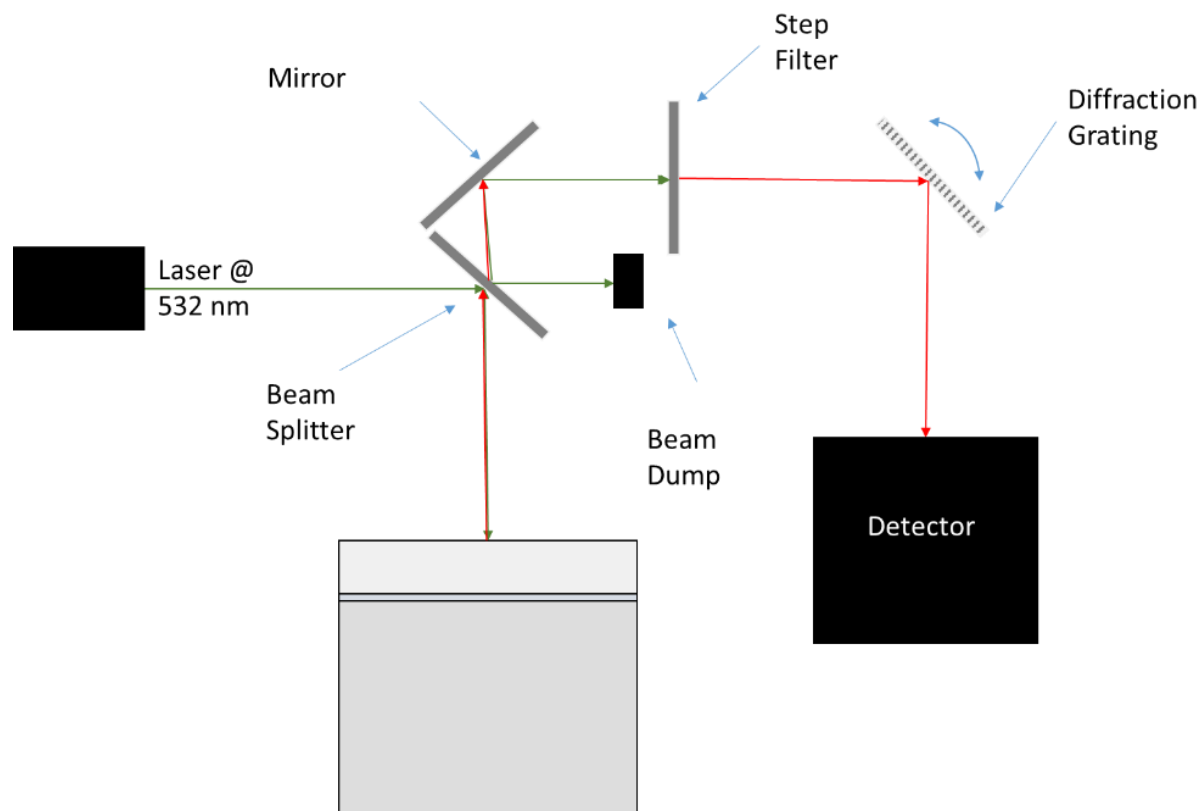


*Figure 2-15 Sketch of a Raman spectrometer*

The second calibration step included compensation for was the angle between the CCD and incoming beam. Without this calibration, a Raman shift would have different values dependent on the position on the CCD, as the spectral resolution of a pixel was not constant across the CCD. In order to measure this effect, a spectral doublet was found in the spectrum of ionized nitrogen. Since the spectral spacing of the doublet was known we could measure its pixel spacing as it was measured at different positions on the CCD and compensate for any variances detected. The results of these two tests were factored into the post-processing of Raman shift data, and a comparison of spectra aligned with other sources of Raman shift data is shown in Figure 2-16.

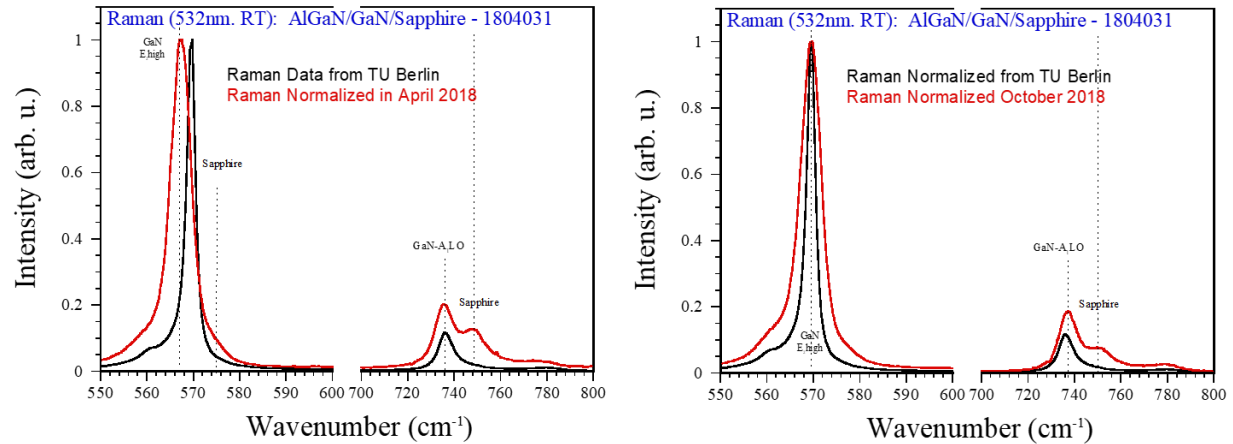


*Figure 2-16 Figure containing data analyzed with and without compensating for errors in the orientation of optical elements compared to data from a professional confocal Raman spectrometer.*

#### **2.2.4 Atomic Force Microscopy**

An atomic force microscope (AFM) allows the direct measurement of the surface of a material. In this technique a sharp probe is placed on the sample and rastered over the sample. The movement of the sample is recorded and converted into a 3D image of the surface of the material.

The AFM can operate in many modes, but the two that are typically used for measuring the surface topology of a sample are contact- and tapping-mode. In contact mode the tip interacts directly and constantly with the surface. In order to record such fine motions, the probe tip is positioned at the end of a thin flexible cantilever. During the surface scan the cantilever is deformed by the forces exerted on the tip by the sample. That deformation is measured by the reflection of light off the top of the cantilever as illustrated in Figure 2-17. In order to extend the life of the tip and ensure more accurate measurements, the sample position is adjusted up or down so the cantilever is ideally kept in a relaxed state and in contact with the surface. The up and down motions of the sample are what is recorded as the height of the surface. This process is performed continuously as the sample is moved back and forth in order to measure a line profile and then up

or down as multiple line profiles are collected to form a three-dimensional data set representative of the surface of the sample. This mode works well for hard samples with slow-changing features, but if there are large changes in height that occur rapidly then the probe tip can be damaged.

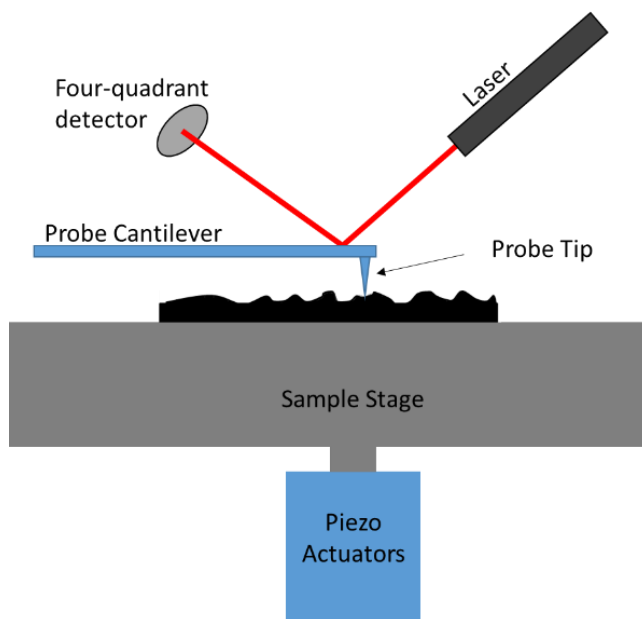


*Figure 2-17 Sketch of the mechanism for the operation of the AFM*

In tapping mode, the tip oscillates, in the vertical direction, at just below the resonant frequency of the probe and instead of measuring the direct deflection of the reflected beam the amplitude of the oscillation is used as a proxy for contact with the surface. This mode is preferred for samples that are softer or if there are rapid changes in the surface that is being measured. Since we are not certain of our sample surface (even though we expect lattice layers) we work in tapping mode to make accurate measurements of our surface.

The AFM can be used to measure surface roughness, identify defects and directly measure lattice spacing. Other effects that can be measured are the localized magnetic and electric fields, and conductivity. The downside of our particular instrument is that it requires wafers to be cleaved to fit on the measurement stage.

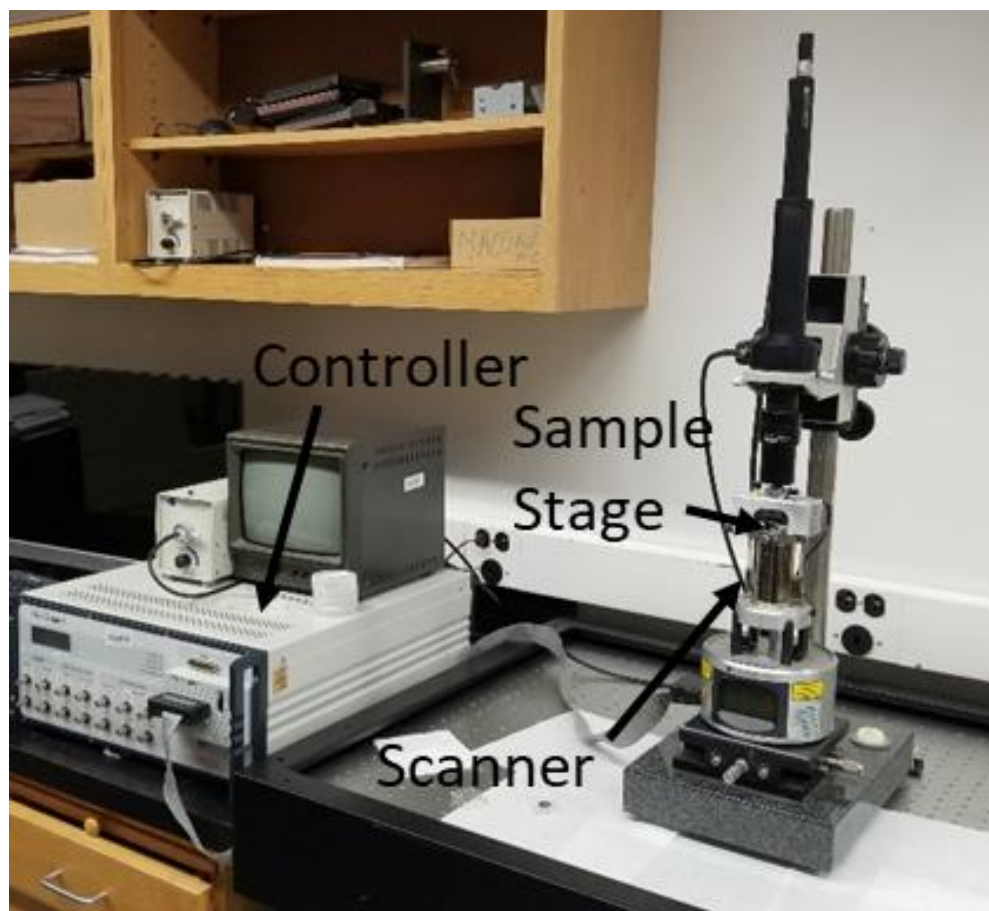


*Figure 2-18 Picture of the Veeco Multimode AFM*

Measurements presented in this thesis were made using a Veeco Multimode AFM, with Nanoscope V controller and Multimode IV scanner stage, as can be seen in Figure 2-18. In order to measure the fine detail of grainy samples a conical AFM probe was used to make measurements. Two types of tip were used, NuNano Scout 350R and  $\mu$ Masch HQ:NSC15/AL BS, both tapping-mode tips with a resonant frequency above 300 KHz, and tip radius less than 10 nm.

### 2.2.5 X-ray Diffraction

X-ray diffraction is the measurement of crystal structure by the diffraction of high-energy electromagnetic waves by the atomic planes in a lattice. As photons interact with atoms in a lattice they are reflected. The interference of the reflected photons is measured.

The constructive interference is achieved when the path length difference of the two photons is equal to a multiple of the wavelength of the incident light. The signal from the interaction between many photons and multiple layers of the crystal lattice creates an angular distribution of responses. A diffractogram is recorded by controlling changes in the incident X-Ray beam angle as well as the detector angular placement a diffractogram is recorded.

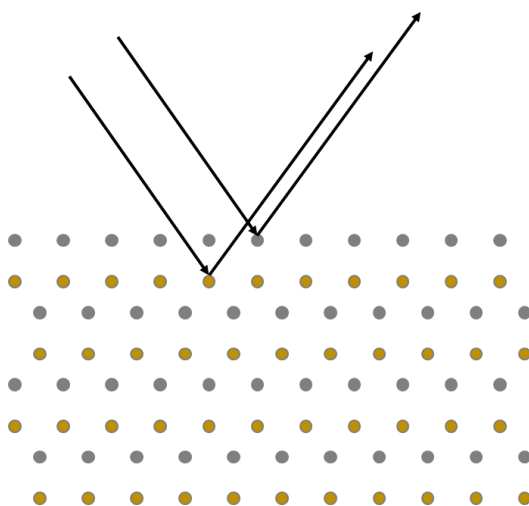


*Figure 2-19 Diagram of X-rays reflecting off consecutive layers of crystal lattice.*

Selected samples were characterized by the X-ray diffraction using a Panalytical X'Pert PRO X-ray diffractometer with a Cu tube running at 45 kV and 40 mA. The XRD was made available to us by Dr. Daniel Deocampo the Department of Geosciences at Georgia State University. While the diffractometer available in his laboratory is not optimal for thin film measurements, it still is capable of  $\theta$ - $2\theta$  scan measurements that provide sufficient details on the InN film crystal structure.

### 2.2.6 Transport measurement

Measuring charge transport properties of semiconductors can provide valuable information on the crystal structure and charge scattering defects. It also provides an assessment of its potential applications in electronics and optoelectronics. Hall effect and resistivity measurements are capable of providing this information.

Hall effect is the measurement of the magnetic field influence on a current flowing through a sample. The effects of the magnetic field on the sample can be related to the number of free carriers in the material as well as the carrier mobility.

Electronic transport measurements of samples were performed in a van der Pauw arrangement as demonstrated in Figure 2-20.

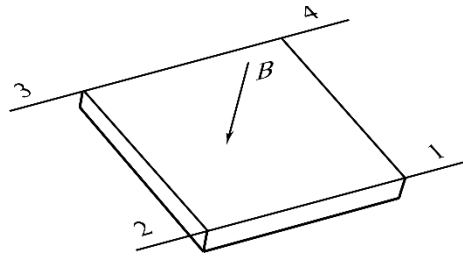


*Figure 2-20 Sketch of a sample set up for measuring Van der Pauw technique. Samples can be connected through any of the numbered contacts.*

Van der Pauw Hall geometry allows the measurement of Hall effect in samples with arbitrary shape (c and d in Figure 2-21). Van der Pauw [109] was first to describe this method of

measuring the resistivity and Hall coefficient, which was later refined by other researchers [110–112].

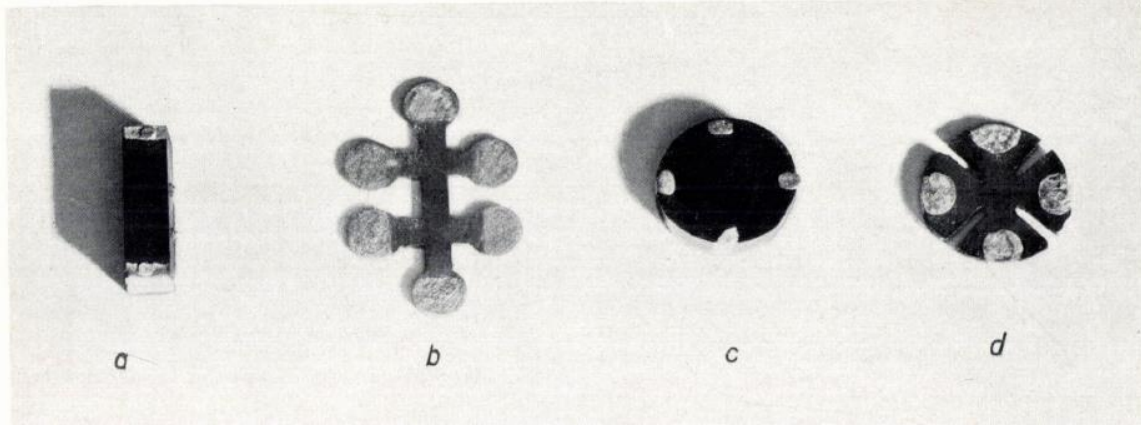


*Figure 2-21 Possible geometries for Hall measurements, including Hall bar (a) test bridge 5(b), and van der Pauw geometries (c and d) [109]*

Using the van der Pauw method to find the resistivity for each sample, data were collected with zero magnetic field. Current was passed through each adjacent pair of contacts, while the potential difference was measured at the opposite two adjacent contacts. For example the current was passed through contacts 1 and 2, while the potential difference was measured between 3 and 4. To mitigate thermoelectric effects the current was then driven the opposite direction through contacts 1 and 2 and the potential difference between 3 and 4 was measured again. Each resistance is calculated by dividing the potential difference measured, by the current driving it on the opposite side, for example  $R_{1243} = V_{12}/I_{43}$ . For each sample this generates 8 resistance values. The forward and backward resistance values,  $R_{1243}$  and  $R_{2134}$  for example, are averaged, leaving four values,  $R_{12}$ ,  $R_{23}$ ,  $R_{34}$ , and  $R_{41}$  where

$$R_{12} = \frac{R_{1243} + (-R_{2134})}{2}. \quad (2.8)$$

Van der Pauw stated the sheet resistance should be solved from the transcendental equation



$$e^{-\frac{\pi t}{\rho} R_v} + e^{-\frac{\pi t}{\rho} R_h} = 1 \quad (2.9)$$

where  $t$  is the sample thickness,  $\rho$  is the resistivity and  $R_v$  and  $R_h$ , are two adjacent resistance values, for example  $R_{12}$  and  $R_{23}$ . Subsequently Ramadan et al. [112] produced a simplified relationship for the resistivity.

$$\rho = \frac{\pi t}{\ln 2} \frac{R_v + R_h}{2} f \quad (2.10)$$

Where  $f$  is the form-factor which can be found using the relationship below

$$\frac{R_v - R_h}{R_v + R_h} = \frac{f}{\ln 2} \cosh^{-1} \frac{e^{\ln 2 / f}}{2} \quad (2.11)$$

The average resistance values found above can then be separated into two pairs of resistance values that are made of adjacent contacts. These two resistivity values are averaged to produce the resistivity of the sample.

For the Hall coefficient measurements, the current is passed on one diagonal ( $I_{24}$ ) and the potential is measured on the other,  $V_{13}$ . The Hall coefficient is then calculated as  $R_{H1324} = V_{13}t/I_{24}B$ . Similar to the resistivity, the current is passed through in the other direction as well to mitigate the effects of the thermal effects on the contacts. The same measurements are made using the alternate diagonal path to produce two values for the Hall coefficient which can be averaged.

This technique was implemented by assembling the Hall measurement setup in our lab. InN/sapphire and InN/GaN/sapphire samples were cleaved from wafers into 6 mm and 10 mm squares and mounted into the ARS DE-202SI closed cycle cryostat that allowed measurements in the 8-300 K temperature range. GE Varnish was used to mount samples. The cryostat is equipped with 4 sample wires which were soldered to the sample using indium solder to insure ohmic contacts [113]. A custom-built 4×4 matrix multiplexer was used to commutate the current supply and voltage measurement wires required by the van der Pauw geometry. An Agilent E3641A DC power supply was used as a sample current source. Current was calculated from voltage

measurements on a  $149\ \Omega$  reference resistor placed in series with the sample. Voltages on sample and reference resistor were measured using Keithley 2000 multimeter. Measurement diagram is schematically shown in Figure 2-22.

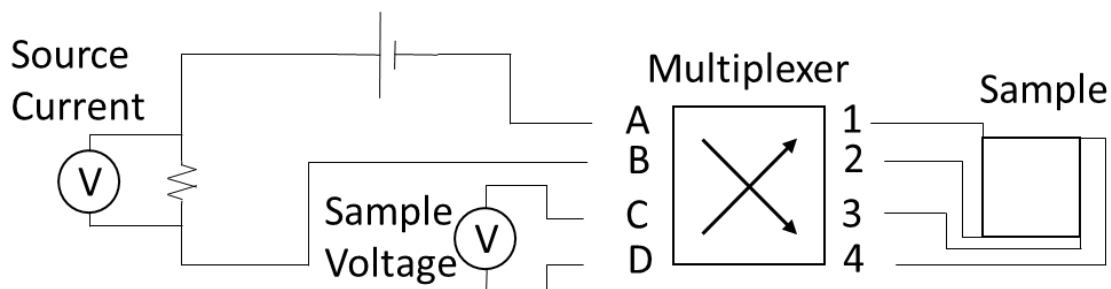


*Figure 2-22 Block diagram of Hall coefficient and resistivity measurement apparatus.*

The cryostat with the sample was mounted to position the sample in the pole gap of electromagnet allowing up to 1.6 T magnetic flux densities. The magnet was equipped with custom-built field direction switch and Agilent N8759A power supply. The magnetic field was measured with a Hall probe placed in front of the sample.

LabVIEW virtual instruments were created to control all parts of the Hall measurement system and collect data.

The sample thickness is found by simulating the Infrared Reflection response and comparing it to the FTIR data as discussed in Chapter 4.

### **3 KINETICALLY STABILIZED HIGH TEMPERATURE GROWTH OF INDIUM NITRIDE**

#### **3.1 Introduction**

Growth of semiconductor heterostructures plays the key role in optoelectronic device fabrication. While heterostructures comprised of AlN and GaN and their alloys are well studied, incorporation of InN in nitride-based semiconductor heterostructures is challenging. One of the known challenges is the lattice mismatch between the InN, GaN or AlN. The difference in lattice constants can cause strain in the material as the layers get thicker, lattice defects will form to compensate for and release the strain. A second challenge is the overgrowth of InN by AlN and GaN due to the differences in decomposition and growth temperature.

The alloying of the group III-nitrides is one of the most important areas of research in semiconductors at this time, as laid out in chapter 1. Growing InN in conditions which are appropriate for GaN and AlN is a known problem that is yet to be solved. In a typical MOCVD reactor TMA and/or TMG are introduced into a high temperature environment that has a significant ammonia and hydrogen content, allowing for chemical reactions to produce free indium and pyrolysis to provide atomic nitrogen ions to form the desired material. However, these precursors degrade the quality of the InN and might be related to its low temperature decomposition and high free electron concentration [88–90].

InN typically decomposes, when heated above 500 to 700 °C [54,66,89,114–120], through the loss of nitrogen leaving indium droplets or clusters in the lattice (see Figure 3-1). This decomposition is related to the free energies of indium and nitrogen combined being lower than the free energy of InN, unless the nitrogen partial pressure is 3 to 5 orders of magnitude higher than typically associated with MOCVD growth of GaN and AlN [66,89,121].

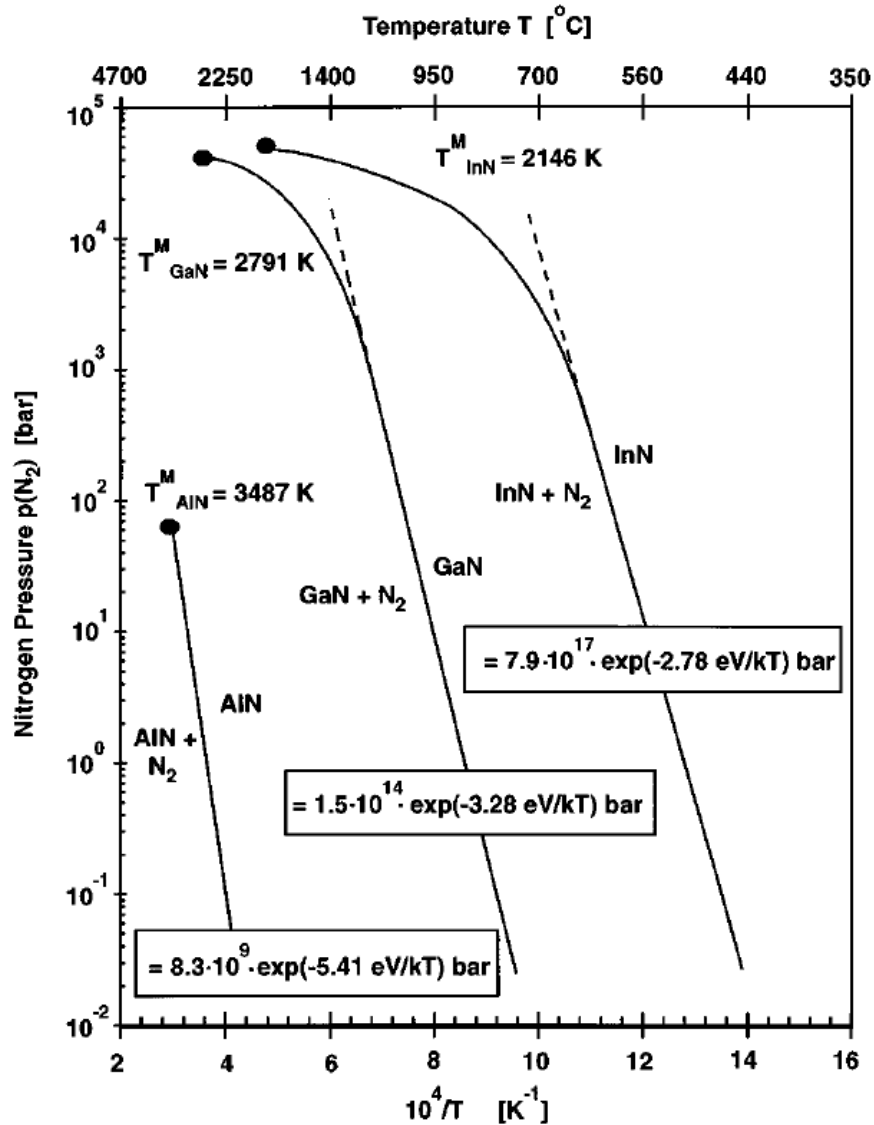


Figure 3-1 Plot of InN stability as a function of nitrogen pressure. Plot from [66] including data from [122].

InN growth on AlN and GaN substrates is typical and often preferred as the lattice mismatch for these materials is lower than for many other common substrates. The associated temperature differences can be ignored because the substrate can be cooled prior to InN deposition. The overgrowth of InN by GaN or AlN at this point often degrades the InN as the latter needs to reach the temperatures necessary to grow the new material. This makes the growth of

heterostructures of III-Nitrides very difficult. One of the methods used to synthesize InN at temperatures high enough to be compatible with aluminum and gallium nitride is high-pressure CVD (HPCVD) [84,105,123–125].

The decomposition of InN can be modified by using higher pressures due to the constant enthalpy associated with this process [33,66]. The drawbacks to using high pressure growth are the decreased growth rate due to the reduced mean free path leading to gas phase chemical reactions and three-dimensional growth propagation, the possibility of loss of containment when dealing with gases under pressure, and the particle dynamics associated with higher pressures place more constraints on the reactor design [105].

Plasma-assisted MBE (PA-MBE) [126–129] and plasma-enhanced atomic layer deposition (ALD) [130] have been shown to overcome some of these challenges. Using ionized nitrogen in PA-MBE offers improved InN crystal quality over conventional MBE growth methods [131]. MOCVD growth of InN could provide higher growth rates and would not require ultra-high vacuum.

In this chapter I explore migration-enhanced plasma-assisted (MEPA) MOCVD growth of InN at temperatures above its decomposition point. The concept of migration enhancement is that with the continuous deposition of indium and nitrogen there is the potential for improper placement of atoms on the growth surface due to rapid reaction. Migration enhancement seeks to mitigate that effect in two ways. First it adds time for the indium atoms to find energetically favorable locations to settle, ideally bonded to nitrogen in the lattice that already exists. Then, when the ionized nitrogen is injected into the system, it stabilizes those indium atoms by extending the lattice with further nitrogen bonds, the increased kinetic energies of the plasma-activated nitrogen species stabilizing the growth surface [72,105,132]. We analyze InN films grown using MEPA-MOCVD

on sapphire substrates at growth temperatures ranging from 700°C up to 957°C, which is well above the reported decomposition temperature of InN.

InN growth was attempted on sapphire wafers using the MEPA-MOCVD system at wafer temperatures ranging from 700 to 957 °C, extending the viable deposition temperature of InN in the same range as the typical MOCVD growth temperature windows of AlN and GaN. In order to verify the growth of InN, Raman scattering from those samples were measured to establish the presence of InN on the wafer. Following that the FTIR and Ultraviolet and Visible spectra were measured to compare to modelled spectra to find the thickness of InN on the wafer.

The surface quality of InN was checked via AFM. Surface measurements were correlated with features observed in Raman spectra. Further evidence of the presence of InN on the wafers was obtained through X-ray diffraction which was performed to verify the quality of the InN. The presence of InN was confirmed but questions on the presence of indium impurities remain.

### **3.2 Samples**

Five samples were grown in the MEPA-MOCVD reactor. Samples were grown on one half of a two-inch diameter c-plane (0001) sapphire wafer. These wafers are obtained with a 0.2° offcut, toward the m-plane, in order to better match the lattice spacing of GaN, which is a negligible effect for the growth of InN directly.

Each sample was subject to the same pre-processing. The first step in the growth process was to “clean” the wafer at 441°C with hydrogen plasma, from the plasma source at the top of the reactor. This step was needed to remove excess oxygen from the reactor and to etch away any surface oxides on the wafer. After cleaning, the substrate temperature was raised to 555°C, and the reactor pressure was set to 4.1 Torr, and a seed (transition) layer of InN was deposited on the wafer. For the buffer layer a plasma power of 350 W was used and a TMI flow of 250 sccm set in order

to deposit a disordered thin layer of material. The purpose of this layer is to create a transition from the sapphire lattice to an InN lattice [83].

After the seed layer was deposited, the temperature of the wafer was raised to the growth temperature under a constant flow of TMI (25 sccm) and nitrogen plasma (150 W). Once growth temperature was reached the growth procedure commenced. The heating then recrystallizes the disordered InN forming crystallites that can be overgrown to form epitaxial layers.

During the growth phase the plasma power and TMI flow were alternately pulsed to create the conditions for migration-enhancement. First the TMI was set to the upper flow rate of  $10.2 \mu\text{mol}/\text{min}$  in a  $\text{N}_2$  flow of 250 sccm for a period of one second and then it was reduced to a rate of  $0.4 \mu\text{mol}/\text{min}$  in 10 sccm of  $\text{N}_2$  for 19 seconds. For the activated nitrogen source, a nitrogen flow of 750 sccm passed through the plasma source with the plasma power switching between 50 W for the first 6 seconds of the cycle and 400 W for the last 14 seconds. This creates a 20 sec process that was repeated for the length of the growth phase. Figure 3-2 shows a representation of the flows in the reactor during this process.

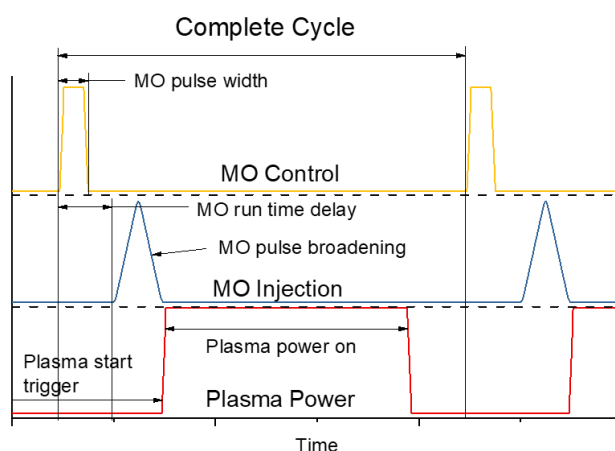


*Figure 3-2 A schematic representation of one cycle of the growth phase.*

Growth was carried out at a reactor pressure of 4.1 Torr for all samples. At the end of the growth cycle the plasma was stopped and the sample was cooled to room temperature in N<sub>2</sub> flow, at which point the wafer was removed from the MEPA MOCVD system.

A list of the samples and their growth parameters can be found in Table 3-1.

*Table 3-1 List of samples and relevant growth parameters used to study the effect of High temperature on InN growth in MEPA-MOCVD*

Sample	Growth Temp. (°C)	N <sub>2</sub> plasma flow (sccm)	Upper plasma power (W)	Lower plasma power (W)	Upper TMI flow (μmol/min TMI)/(sccm N <sub>2</sub> )	Lower TMI flow (μmol/min TMI)/(sccm N <sub>2</sub> )	Growth time (min)
1162	816	750	400	50	10.2/250	0.4/10	120
1165	929	750	400	50	10.2/250	0.4/10	120
1166	873	750	400	50	10.2/250	0.4/10	120
1167	957	750	400	50	10.2/250	0.4/10	120
1170	700	750	400	50	10.2/250	0.4/10	122

### 3.3 Results

#### 3.3.1 Raman spectroscopy

Room temperature Raman spectroscopy in backscattering geometry was used to investigate the structural composition of grown films. A 500 mW, 532 nm laser was used as an excitation source. Figure 3-3 shows a typical spectrum measured on sample 1165 and the peaks extracted using a multi-peak fit of the experimentally acquired Raman spectra for the samples in this study. The data were analyzed using Fityk, [133] using a Gaussian function for each expected peak and optimizing the fit using the Levenberg-Marquardt method [134,135].



The peak located at  $575\text{ cm}^{-1}$  is attributed to the  $E_g$  mode of the sapphire substrate [136]; the peaks located near  $490\text{ cm}^{-1}$  and  $587\text{ cm}^{-1}$  are related to the InN  $E_2(\text{high})$ , and  $A_1(\text{LO})$  phonon modes respectively [137,138]. The presence of the InN  $E_2(\text{high})$  and  $A_1(\text{LO})$  phonon modes indicates that wurtzite InN is present. The FWHM of the  $E_2(\text{high})$  peak can be an indicator for the crystalline quality of the InN, as the peak represents the aggregate response of the lattice that is excited, each phonon excitation contributes to the Stokes emission and the larger the variability in the lattice the more spread out in frequency space the Stokes response will be. The FWHM of the  $A_1(\text{LO})$  mode similarly contains contributions from the phonon-plasmon interaction and point defects [139,140].

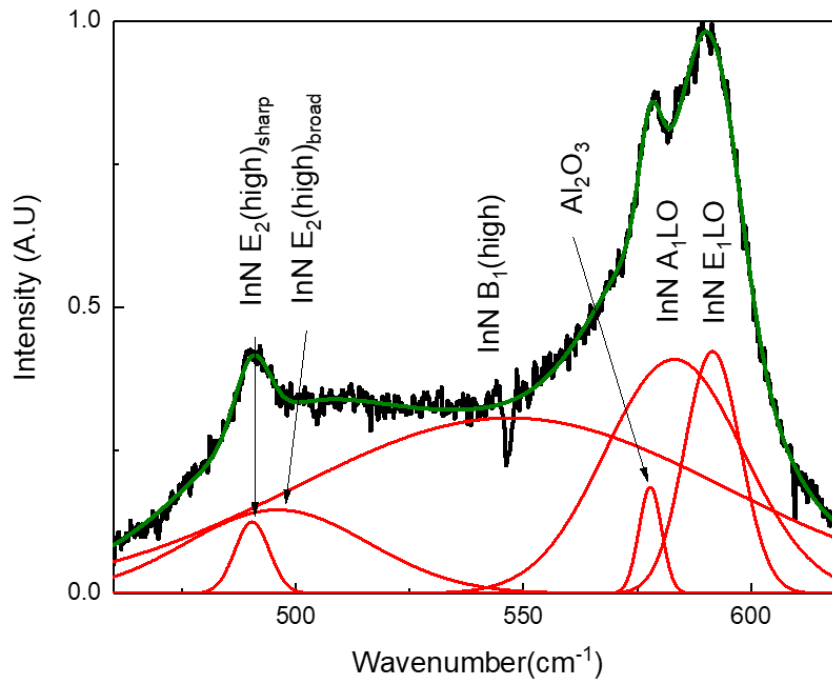
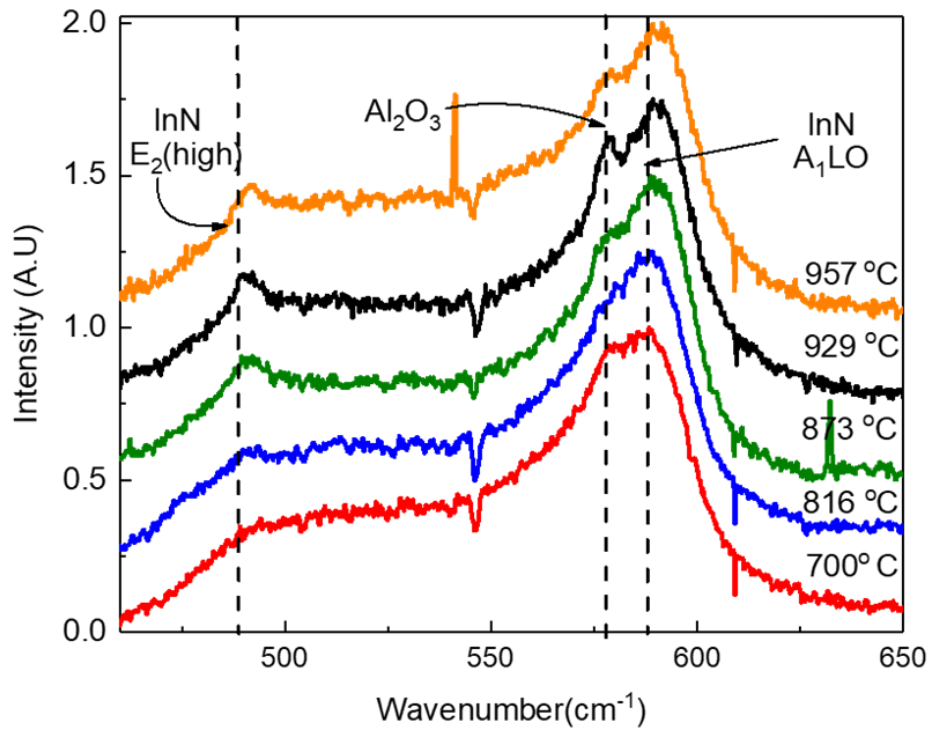


Figure 3-3 Raman spectra of the sample grown at  $929^{\circ}\text{C}$  with (red) lines indicating individual phonon modes and (green) whole spectra multi-peak fitting.

The presence of the  $E_1$  and  $B_1$  “invisible” modes does not form part of the basis for discussion of the presence of InN. If the material was a single crystal and aligned so that the c-axis

was vertical, the vibrations corresponding to these phonons would not be in an orientation that could be excited. Since they are present I can say that this material is most likely polycrystalline and disordered [141,142].



*Figure 3-4 Raman spectra for all samples in this experiment, Dashed lines indicate phonon modes that should be visible in this orientation.*

The full-width at half of the maximum (FWHM), amplitude, and peak positions of the  $E_2(\text{high})$  and  $A_1\text{LO}$  peaks were recorded for comparison purposes and to provide insight into the quality of the crystallinity and free carriers and are shown in Table 3-2.

It is typical for a single-phase highly crystalline material to exhibit only one phonon peak of each type, but as can be seen in Figure 3-3 in order to provide a reasonable fit of the data a second  $E_2(\text{high})$  phonon mode needed to be modelled. This can be the case when the material is

composed of a mix of two crystallographically different material types, each exhibiting unique phonon responses. As can be seen in Figure 3-4, the sharp  $E_2$  peak was not present on all samples grown.

*Table 3-2 Raman shifts of  $E_2$ -(high) and  $A_1$ -LO phonon modes with their widths.*

Phonon Mode	Growth Temp (°C)	Sample	Peak Shift (cm <sup>-1</sup> )	FWHM (cm <sup>-1</sup> )	Peak Shift Error (cm <sup>-1</sup> )	FWHM error (cm <sup>-1</sup> )
$E_2$ - sharp	873	1166	490.342	10.2796	0.905776	0.61232
$E_2$ - sharp	929	1165	490.455	8.85637	0.126846	0.367116
$E_2$ - sharp	957	1167	490.972	7.84196	0.218494	0.661666
$E_2$ - broad	700	1170	497.432	42.5783	0.259023	1.539216
$E_2$ - broad	816	1162	496.499	46.0219	0.433478	0.725274
$E_2$ - broad	873	1166	492.339	36.0678	0.330384	2.36946
$E_2$ - broad	929	1165	496.002	47.0299	0.535556	3.27288
$E_2$ - broad	957	1167	495.029	33.781	0.552214	2.02878
$A_1$ -LO	700	1170	577.508	9.24569	0.199979	0.775442
$A_1$ -LO	816	1162	576.345	11.7122	0.509933	1.344858
$A_1$ -LO	929	1166	577.184	7.52174	0.106268	0.428112
$A_1$ -LO	929	1165	577.89	5.85825	0.076348	0.226026
$A_1$ -LO	957	1167	577.551	7.30589	0.207147	0.612214

The FWHM of the two  $E_2$ (high) phonon modes exhibit different effects due to increasing growth temperature. There is no real trend for the broad peak, but the FWHM of the sharp peak does decrease as the growth temperature increases as can be seen in Figure 3-5.

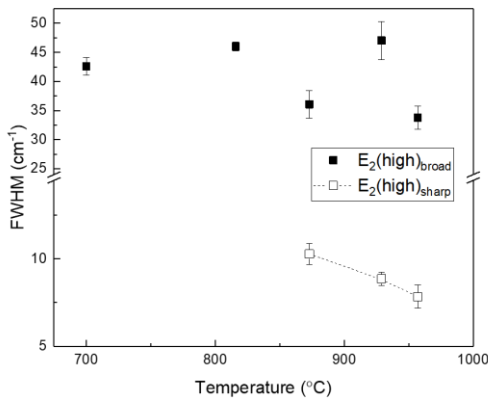


*Figure 3-5 FWHM of the  $E_2$ (high) phonon peak as a function of temperature.*

Due to some uncertainty in the interpretation of X-ray diffraction data there questions as to the presence of indium in these samples. This was addressed by performing Raman measurements in the 2000 to 2600  $\text{cm}^{-1}$  wavenumber range in search for peaks associated with metallic indium. The measurements system used to perform these measurements was made available by Dr. Sidong Lei at the Department of Physics and Astronomy, GSU. A 514 nm excitation source was used. Results of these measurements performed on the sample grown at 957°C is shown in Figure 3-6. The analyzed sample was grown at the temperature at which we would most likely see decomposition. The Raman spectrum did not reveal any notable peaks at 2215  $\text{cm}^{-1}$ . These results indicate that there is not a significant presence of metallic indium in the grown samples [143]. The two peaks observed below 2200  $\text{cm}^{-1}$  are related to the absorption dips seen in the FTIR data around the same spectral range [144].

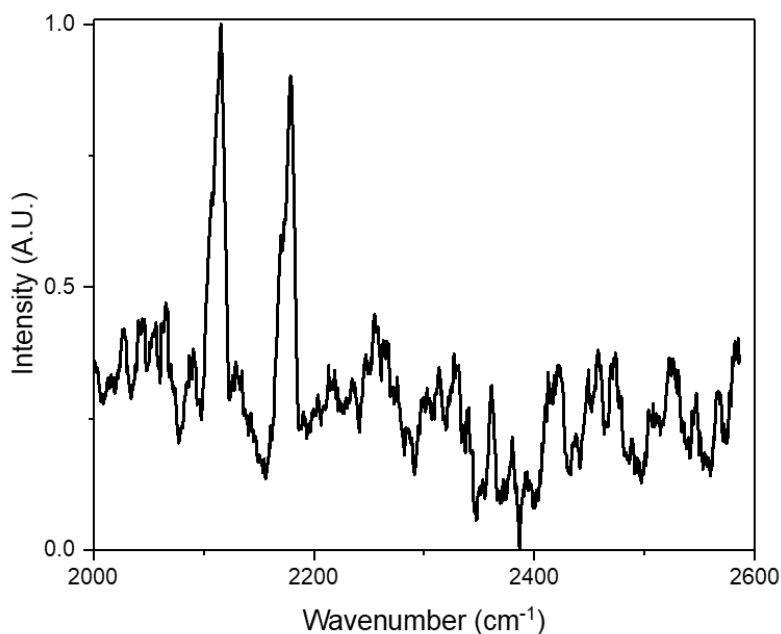


*Figure 3-6 Raman data from 2000 to 2600  $\text{cm}^{-1}$  showing no significant peak associated with InN.*

### 3.3.2 FTIR spectroscopy and modelling the film thickness

FTIR spectra were collected for all the samples. Film thickness was determined by fitting interference fringes in these spectra using the multi-layer stack modelling method described in [106,145]. Figure 3-7 shows the Infrared reflectance for the samples in this experiment.

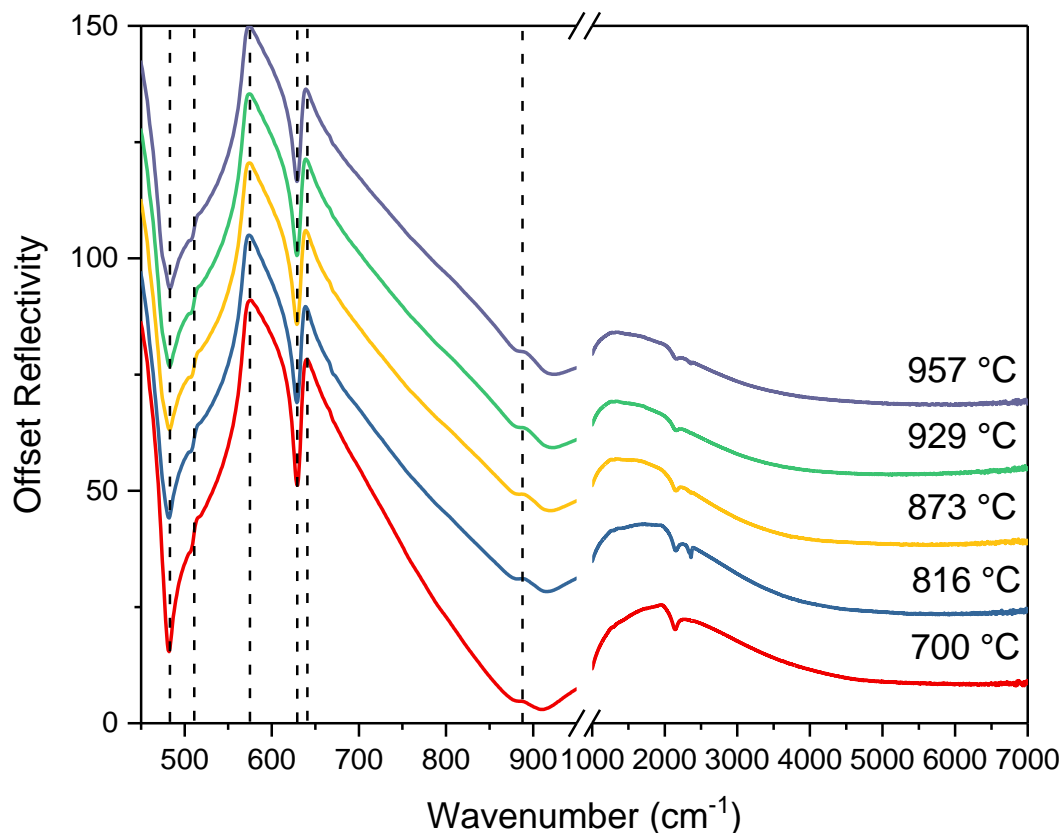
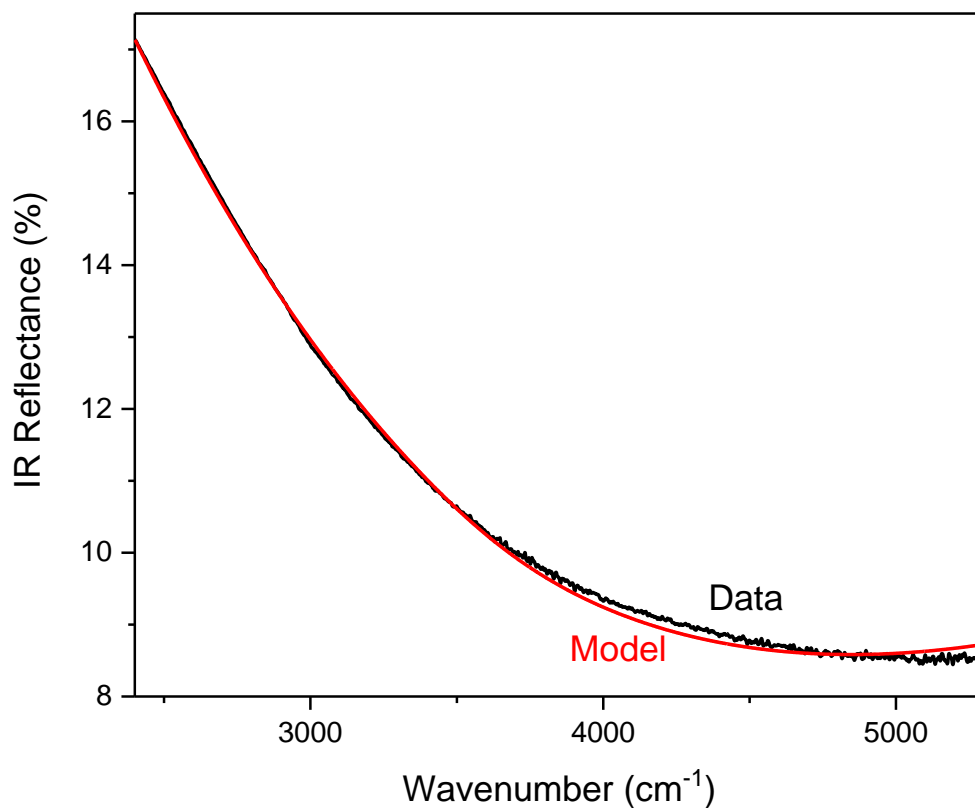


Figure 3-7 FTIR reflectance spectrum measured on InN sample grown on *c*-plane Sapphire.

The InN film and sapphire substrate phonon features were observed in the 450  $\text{cm}^{-1}$  to 2200  $\text{cm}^{-1}$  range. The absorption dips near 2150  $\text{cm}^{-1}$  are typically associated with an impurities such as additional nitrogen or carbon and oxygen [146]. Further work would be necessary to

establish what these features are attributed to. No phonon-related spectral feature trends were observed for InN films grown at different temperatures.

Sample thicknesses were extracted by fitting the reflectance data within the  $2400\text{ cm}^{-1}$  to  $5300\text{ cm}^{-1}$  spectral range, thus ignoring the possible effect of absorption above the bandgap (above  $5400\text{ cm}^{-1}$ ), although according to Bhuiyan et al. [147] for a polycrystalline film the bandgap has a significantly higher value. Figure 3-8 shows the modelled portion of the spectrum with the data for sample 1165.



*Figure 3-8 IR spectrum showing the data and model over the fitted range for sample 1165, grown at 929 °C*

Sample reflectance matched InN films modelled with thicknesses of 20-70 nm. Corresponding growth rates varied within 10-35 nm/hr with the maximum growth rate at 873°C. There also seems to be a plateau in growth rate above that, but there are insufficient data to draw a conclusion about a growth rate above 900°C, with no clear trend with growth temperature variation as can be seen in Figure 3-9. While the optical thicknesses of grown films were less than half of the wavelength, the modelled reflectance was calculated as a far-field response. The parameters used in the model, and calculated growth rates are shown in Table 3-3.

*Table 3-3 Parameters used to model the reflectance of measured samples.*

Growth Temp (°C)	700	816	873	929	957
Sample Number	1170	1162	1166	1165	1167
Modelled. Thickness	$23.3 \pm 0.4$	$55.8 \pm 0.4$	$72.3 \pm 0.4$	$60.9 \pm 0.4$	$61.2 \pm 0.4$
Growth rate (nm/hr)	$11.7 \pm 0.2$	$27.9 \pm 0.2$	$36.2 \pm 0.2$	$30.5 \pm 0.2$	$30.6 \pm 0.2$
$\epsilon_{\infty}$	5.8	5.8	5.8	5.8	5.8

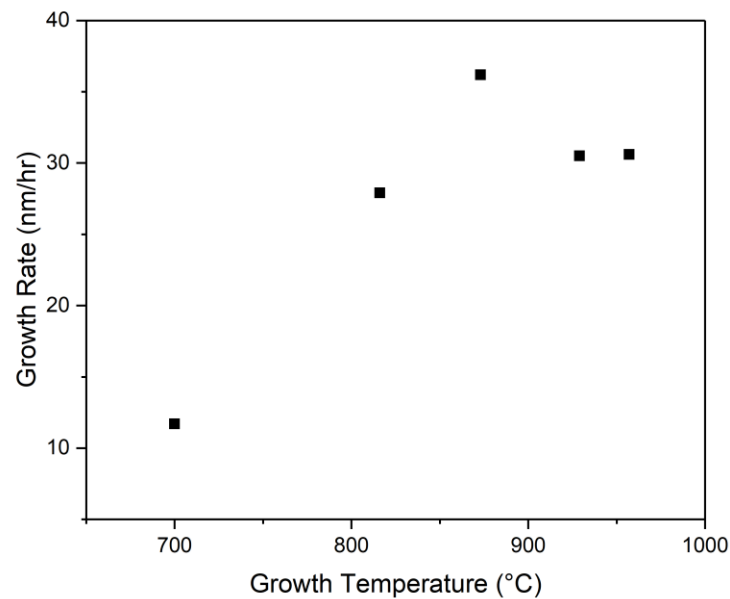


*Figure 3-9 Growth rate as a function of growth temperature, showing a peak growth rate at 873°C. The growth rate measurement error is negligibly small as compared to the data symbol size.*

### 3.3.3 Atomic Force Microscopy

AFM was used to analyze the surface morphology of the grown samples. Results of the AFM imaging are shown in Figure 3-10 to Figure 3-14. Scans of a large area ( $10\ \mu\text{m}^2$ ) and small area scans ( $1\ \mu\text{m}^2$ ) were made for inspection and to get surface measurements respectively.

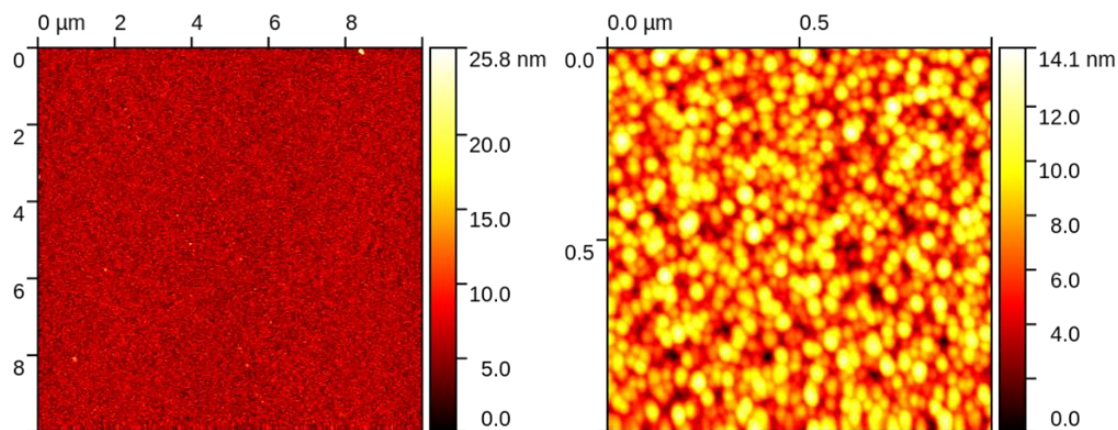


*Figure 3-10 AFM scans of sample 1170*

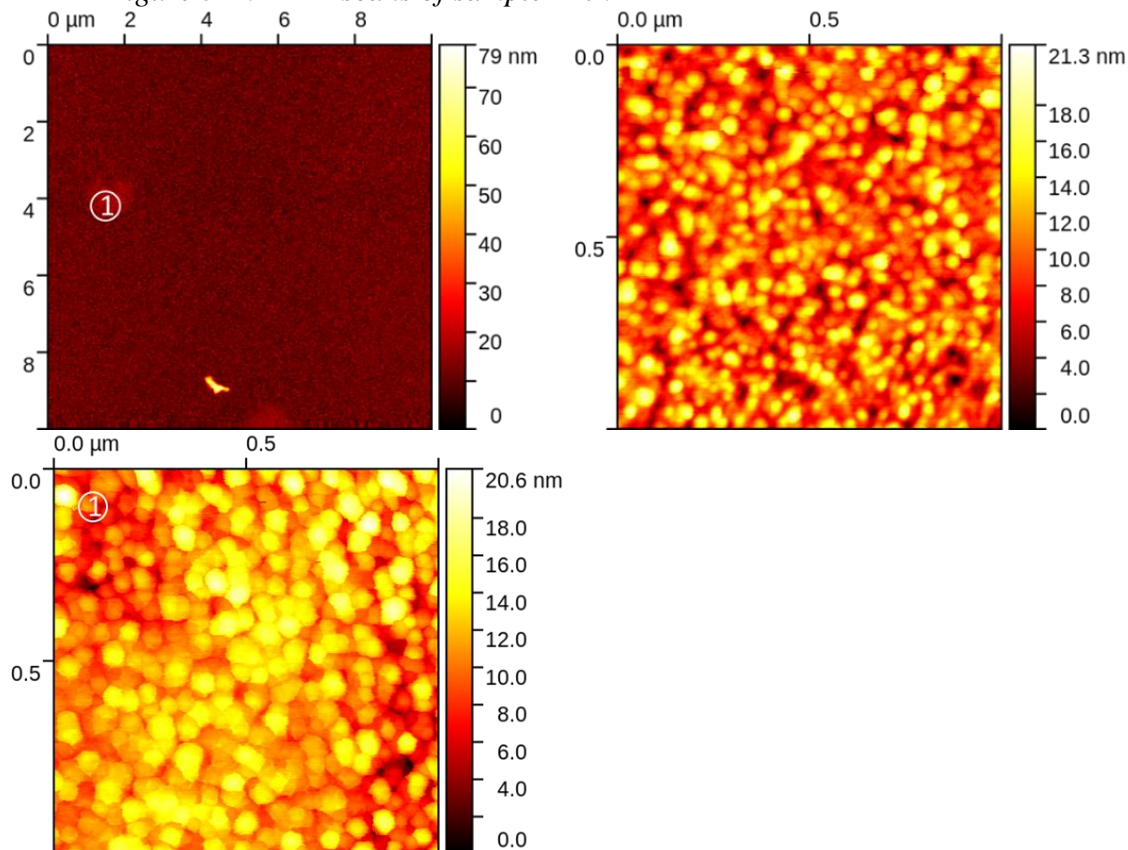


*Figure 3-11 AFM scans of sample 1162*



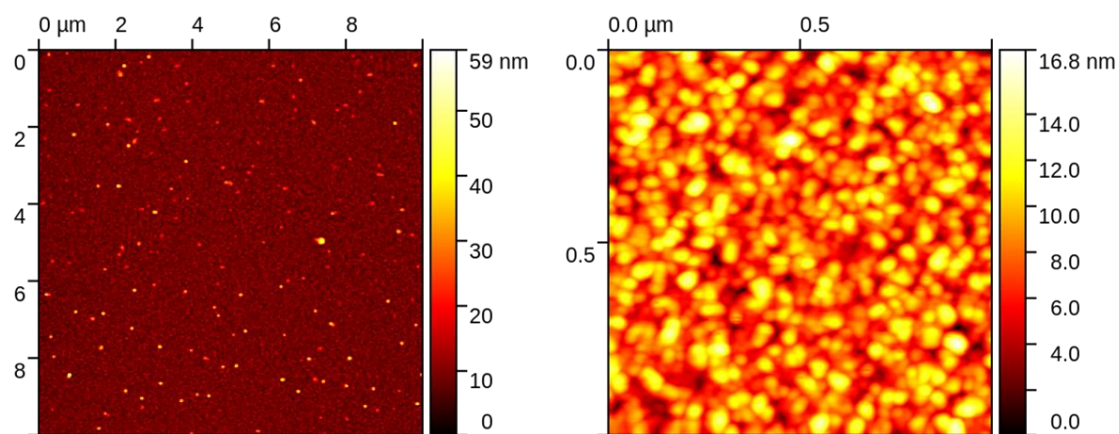


*Figure 3-12 AFM scans of sample 1166*

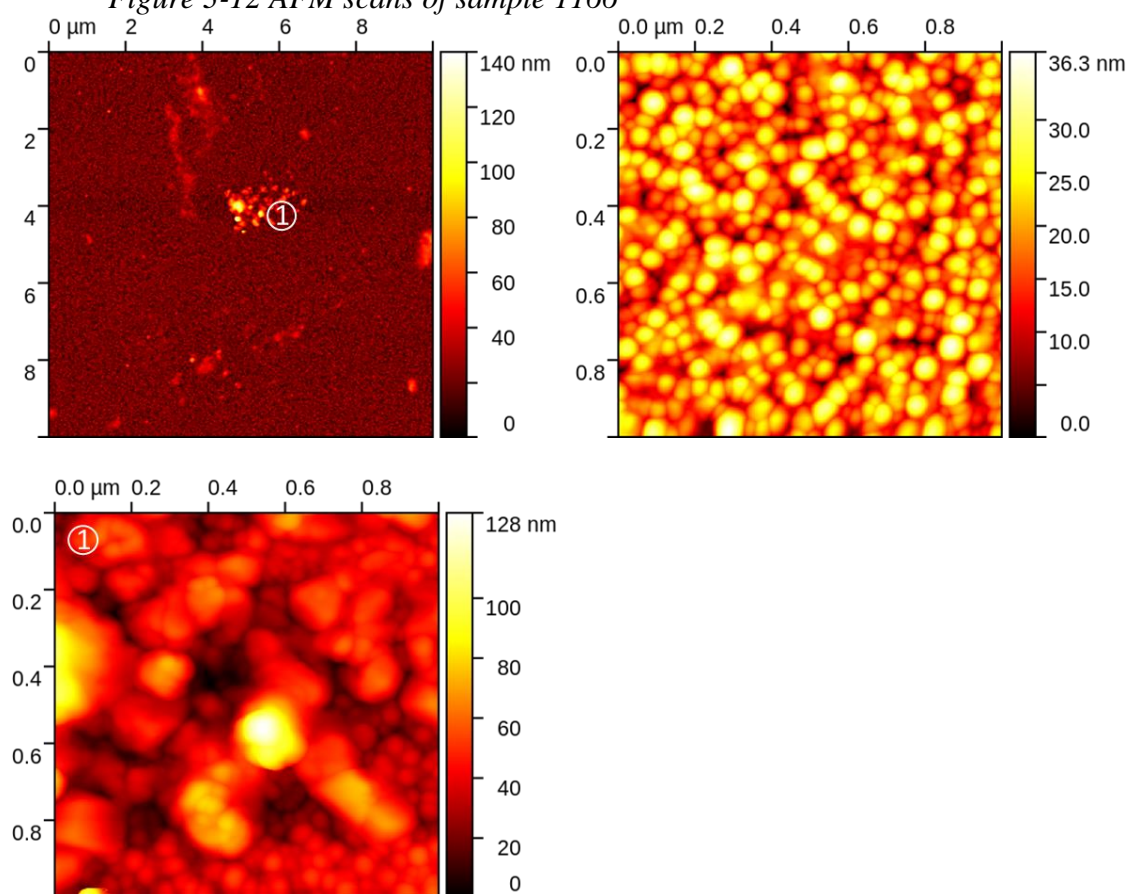


*Figure 3-13 AFM scans of sample 1165*

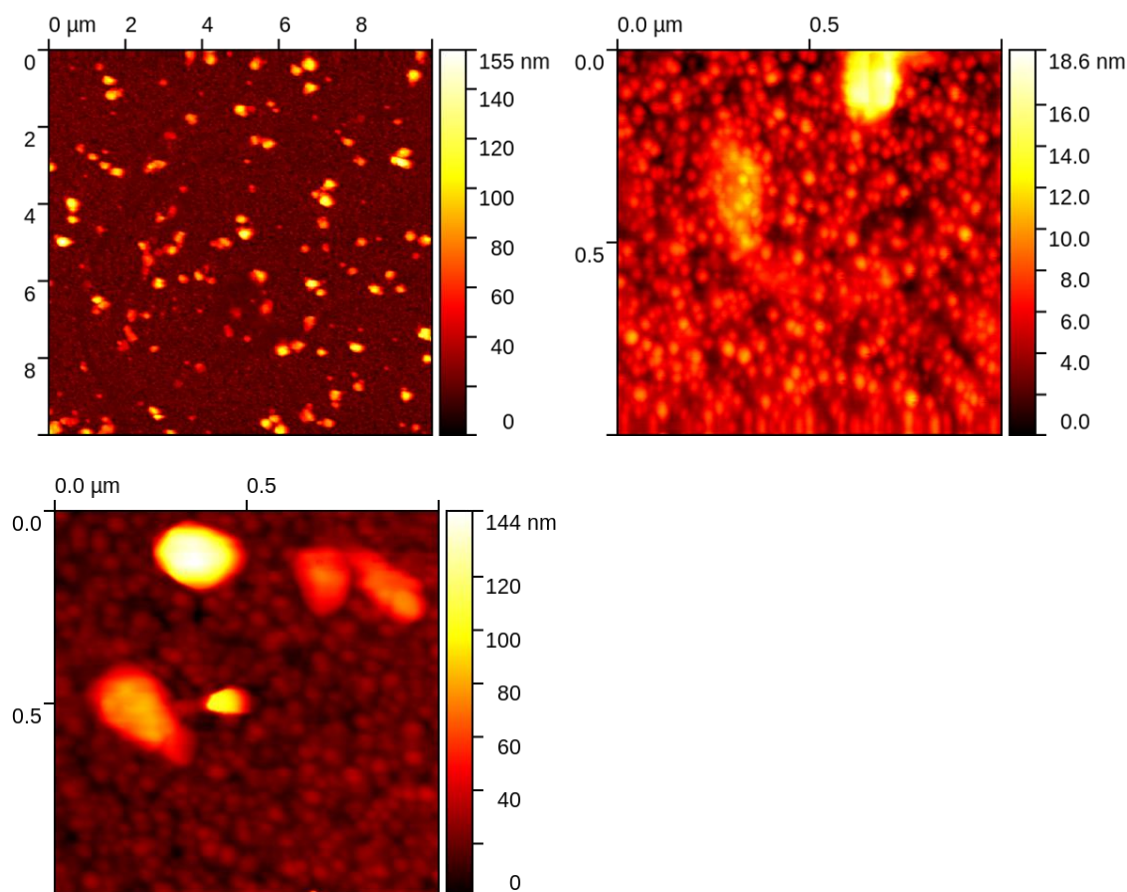


*Figure 3-14 AFM scans of sample 1167*

All grown samples demonstrate a grainy surface. The grains do not exhibit hexagonal facets as would be expected for highly crystalline InN. The grain median radius varies in the range of 8.7 – 11.6 nm. These statistics are found using Gwyddion, an open source AFM data analysis tool [148]. In order to work consistently the same procedure was followed with each 1  $\mu\text{m}$  “background” scan. Each AFM scan line was leveled using a trimmed mean with a trim fraction of 0.1. Next the data were filtered to reduce AFM noise, a median filter was applied with a size of 4 pixels. In order to collect information about grain size, grains were marked by threshold, using 8 steps, a drop size of 4% and a threshold of 7 square pixels. Segmentation was set up with 35

steps and a drop size of 1% and then the grain statistics were collected and can be found in Table 3-4.

*Table 3-4 Statistics collected from the AFM scan data*

Growth Temp (°C)	sample	AFM scan	Median Equivalent disc radius (nm)	RMS of eq. disc radius (nm)	Median grain height (nm)	RMS in height (nm)
700	1170	02051311	8.692	3.359	9.226	1.736
816	1162	02011111	9.746	4.281	12.41	2.63
873	1166	02061343	10.49	4.46	9.795	2.011
929	1165	12131701	11.01	4.72	21.83	5.42
957	1167	02151003	11.57	9.66	20.5	3.71

The convolution of the tip radius with the sample size must be remembered when comparing the radius with the median height. The thresholding process may also account for some of the differences between radius and height. The appearance of large grain structures (approximately 35 – 80 nm in radius) occur on samples grown at 873, 929 and 957°C. This change in structure could be considered similar to changes observed by Ploch et al.[1], but the growth temperatures are about 350°C higher than they reported. At the same time the large grain appearance coincides with appearance of the “sharp” E2(high) peak observed in Raman spectra.

### **3.3.4 X-ray Diffraction**

Structural properties of all grown films were evaluated using XRD measurements. Figure 3-15 shows a typical X-ray diffraction pattern measured on the sample 1166 grown at 873°C. For all analyzed samples, (0002) InN, (0004) InN and the (0006) Al<sub>2</sub>O<sub>3</sub> peaks were observed, located at 31.38°, 64.90°, and 41.85° respectively. Rotation in the  $\phi$  direction did not show significant

variation in the InN peak intensity, indicating a highly disordered crystalline film, affirming Raman results.

These results are similar to other diffraction measurements made of InN [149–151]. Gao et al. [149] identify the peak at  $33^\circ$  as belonging to InN, this would be expected since we identify our material as being polycrystalline and disordered. Moret et al [150].and Huang et al. [151] identify a peak near this location as belonging to In, which would also not be surprising. The physics behind this process is not fundamentally understood and some indium could be present in our material due to factors such as decreased partial pressure of ionized nitrogen during the cooling after growth leading to In droplets.

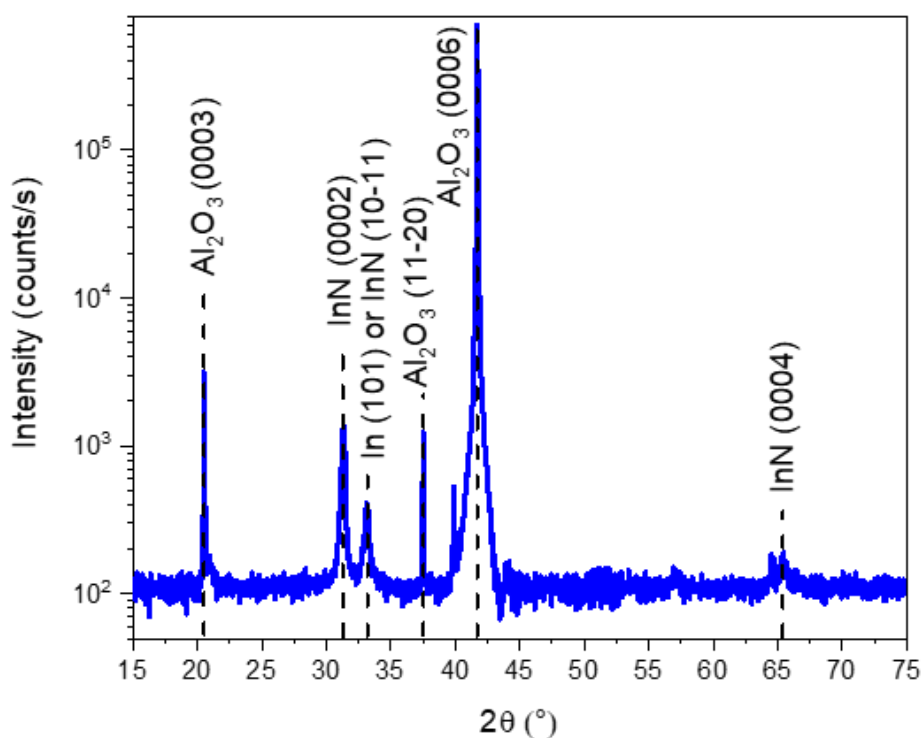


*Figure 3-15 XRD data of InN grown at  $825^\circ\text{C}$ . Spectrum demonstrates presence of InN. The peak at  $33^\circ$  has not been identified as [149] claims it belongs to InN and [150,151] identify it as belonging to In. The peak at  $40^\circ$  also remains unidentified.*

### 3.3.5 Hall measurements

In order to better understand the films that were grown charge transport measurements were made. Sample resistivity for these samples are shown in Figure 3-16.

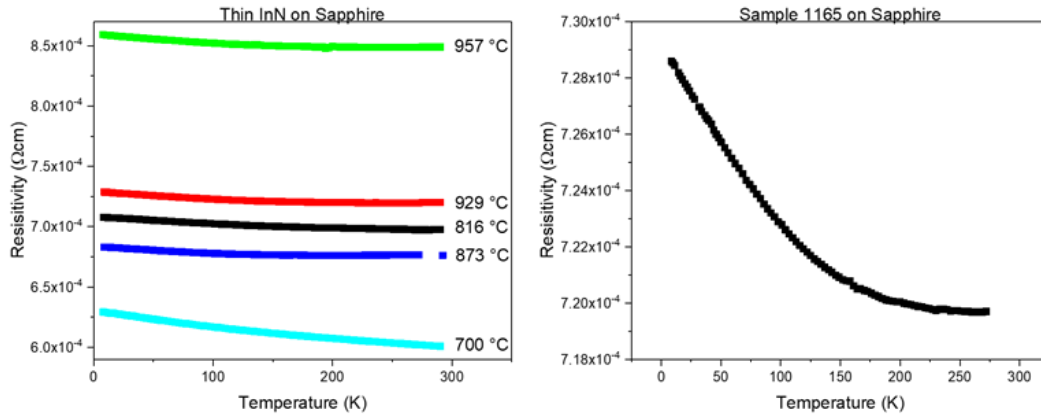


Figure 3-16 Resistivity for thin (<75 nm) InN samples on Sapphire, growth temperatures are labelled. Resistivity of sample 1165, grown at 816 °C, is shown for detail of resistivity as a function of measurement temperature (x-axis).

Except for sample 1166 there is an increase of resistivity with growth temperature. To better observe the relationship between resistivity and temperature the data for sample 1165 is plotted separately. The observed trends correlate with the properties expected of semiconductors, resistivity increases with decreasing temperature.

The Hall coefficient was measured at a field of approximately 0.5 T. Combining this information as described in section 2.2.6, the free electron concentration was found and is shown in Figure 3-17. Free electron concentrations range from  $1 - 9 \times 10^{20} \text{ cm}^{-3}$ . These values are high compared to the reported values for the highest quality PA-MBE grown samples, but fall within the acceptable range of free electron concentrations reported [147].

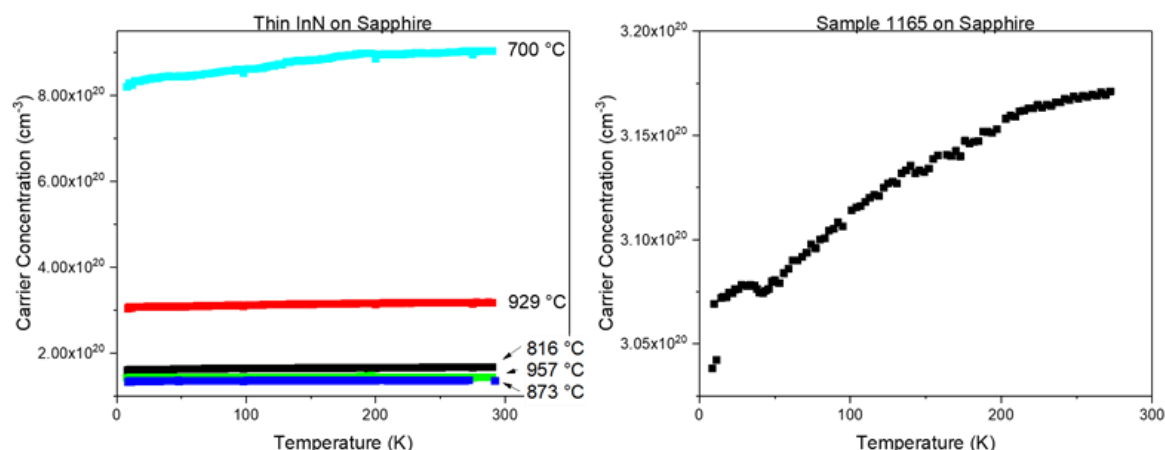


Figure 3-17 Free electron concentration for each sample as a function of temperature. The electron concentration of sample 1165 plotted separately to show detail as a function of temperature.

Electron mobility was also calculated and falls within those previously reported ranges [147], but nowhere near the theoretical values calculated, or maximum values measured. This is likely due to the high carrier concentration and the material not being a single crystal, but rather a grainy surface observed in AFM scans.

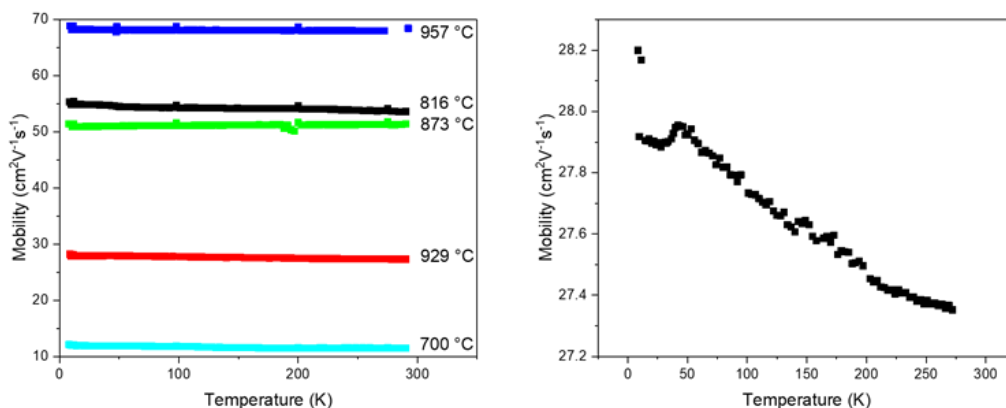


Figure 3-18 Mobility of each sample as a function of temperature, and for sample 1165 to show detail.

### 3.4 Discussion

Starting with the appearance of the  $A_1LO$  and  $E_2(\text{high})$  peaks in the Raman data for all samples we can safely say that InN is present on these samples grown above the decomposition temperatures previously reported. The two things that need to be addressed from the Raman results are the presence of the “hidden” modes, those phonon modes that should not be excited in this measurement orientation, and the second  $E_2(\text{high})$  peak needed to correctly model the data. Kontos et al. [40] and Davydov and Klochikhin [142] both report seeing these hidden modes in Raman spectra and attribute them to a disordered polycrystalline film. The FWHM values for the phonon peaks measure are plotted in Figure 3-19. No visible trend is observed for the broad  $E_2(\text{high})$  or  $A_1LO$  peaks, but there does seem to be a downward trend in the size of the sharp  $E_2(\text{high})$  peak.

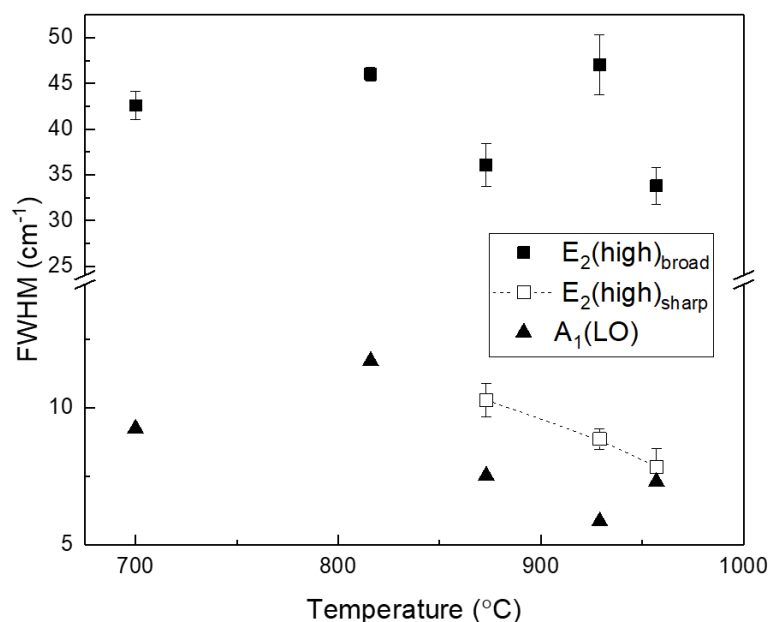


Figure 3-19. Temperature dependence of the  $E_2(\text{high})$  (empty squares for sharp peak, solid squares for broad peak) and  $A_1(LO)$  phonon mode peak FWHM (triangles). Dashed line illustrates the trend.

The AFM results presented attest to the polycrystalline nature of this film, adding to the plausibility that the “hidden” modes are due to this property of the film. A second result from AFM is the appearance of larger structures on the sample corresponding to the need to model a second sharp E2(high) peak. The downward trend in the FWHM of this peak could be a size related effect [152], meaning that the larger structures present in AFM scans are likely strain-relaxed InN crystallites.

The obtained XRD results are consistent with results previously reported [149–151] but the question as to the presence of In in the sample is something that needs to be explored in more detail. The lack of a peak in the additional Raman data collected indicates that indium might not be present. Either possibility is acceptable, it is just another challenge to deal with in the continued refinement of InN synthesis.

In combination with the infrared modelled thickness for the samples, the sheet resistance measurements give us the sample resistivity, which should be bound by an Arrhenius equation,

$$\rho = \rho_0 e^{\frac{E_A}{k_B T}}$$

Plots of the resistivity vs  $1000/T$  are presented in Figure 3-20. The left plot has a natural log scale on the y-axis, the right hand plot has the natural log of the resistivity plotted in order to find the slope of the graph. Using the slope the activation energy can be found,

$$\ln(\rho) = \frac{E_A}{k_B T} + \ln(\rho_0) = \frac{1000m}{T} + b$$

so, the activation energy is then:

$$E_A = 1000mk_B$$

For sample 1165 the activation energies found for the two slopes in the graph are  $6.04 \times 10^{-5}$  eV and  $1.83 \times 10^{-6}$  eV. Neither of these values are close to the bandgap for the materials, so



there are two possible sources for these energies. The first possibility is the presence of impurity or defect energies. The second possibility is the effect of a grainy surface, as can be seen in AFM this surface is not flat and InN does have electron accumulation on its surface [153–158]. These two factors can lead to hopping charge transport.

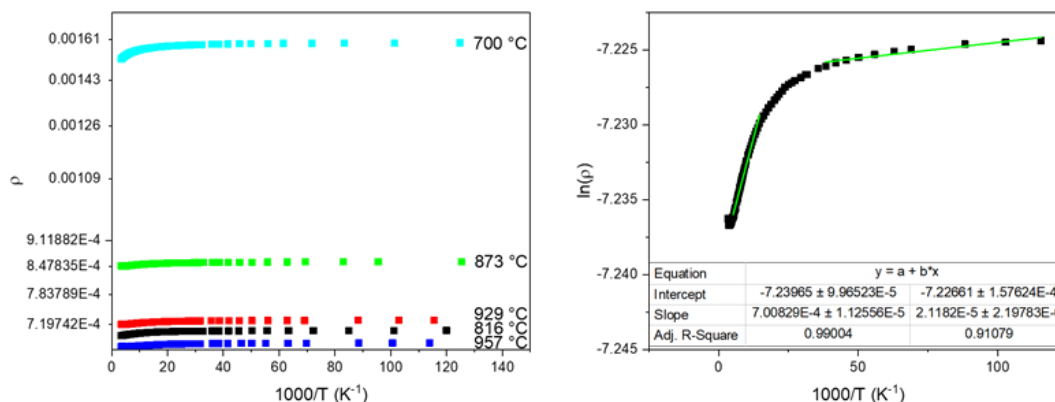


Figure 3-20 Arrhenius plots for resistivity for all samples and for sample 1165 to calculate activation energy from slope.

### 3.5 Further Work

There are unanswered questions relating to XRD, Hall and Raman measurements of InN grown above decomposition temperature.

Work needs to be done to identify the composition of the film, identifying impurities and working to identify whether metallic indium inclusions exist. If the metallic inclusions or other impurities exist, that could help to explain this seemingly impossible result of material being deposited above the previously accepted temperatures. If there are no impurities, then the process and thermodynamics of the synthesis of InN need to be explored for ionized precursors to better understand the process we are utilizing.

Work needs to be done to better measure the thickness of the material, because there are potential pitfalls to modelling the film reflectance. It is possible to physically measure film thickness and I think this should be pursued.

The electron transport properties of this film seem unique and deserve further study. Hopping charge transport and surface charge accumulation and impurity levels need to be explored to try and resolve these issues.

An additional curiosity emerged during the process of performing the AFM scans. It was observed that certain samples (1166 in particular, for this study) exhibit interesting surface effects when interacting with the AFM probe. Initially I observed this as a phase difference between high and low sections of the film. This results in the AFM scan looking like there were steps around the grains. Figure 3-21 shows these data.

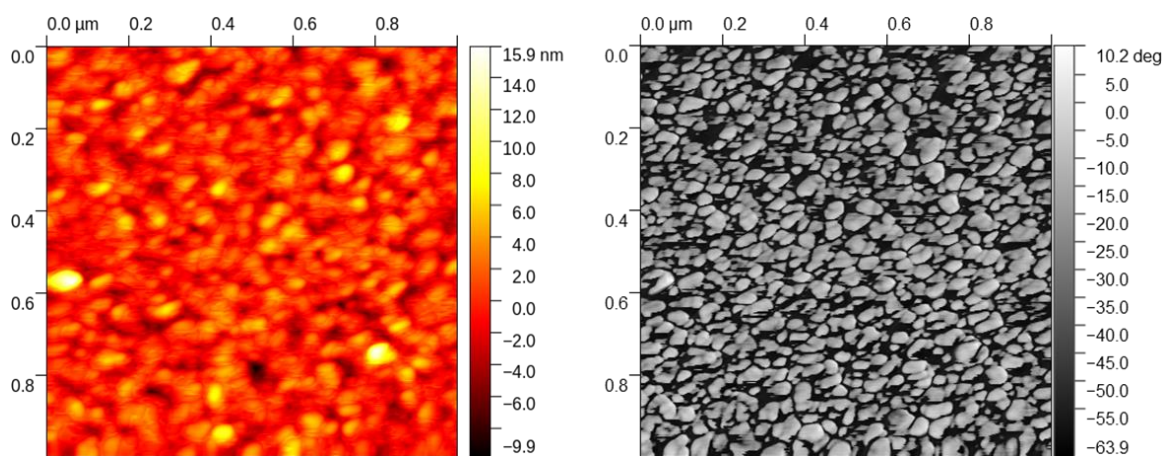


*Figure 3-21 Surface topography and tapping probe phase difference on sample 1166*

This effect disappeared over the course of an hour after grounding the sample to the AFM. I think it is likely due to polarization of the AFM tip due to a surface charge on the sample, and capacitance effects keeping the sample charged for a long time.

### 3.6 Conclusion

In summary, InN films were grown at temperatures varying from 700°C to 957°C using plasma-activated nitrogen as the group V precursor in the MEPA-MOCVD system. InN growth was confirmed by Raman Spectroscopy and XRD. Broad and sharp E<sub>2</sub>(high) Raman peaks were used to refine the model spectra for sample grown above 873°C. We attributed them to disordered small grain InN and coalesced crystalline large grain InN as revealed by the AFM. Hall transport measurements revealed that changes in free electron concentration and mobilities are independent of growth temperature and are likely defined by surface and possibly hopping electron transport.

We demonstrated indium nitride growth above its decomposition temperature, which gives more options to explore the growth of ternary alloys and heterostructures with GaN and AlN. The presence of impurities (possibly nitrogen per FTIR results), or the lack of hydrogen in the growth reaction could be factors allowing for growth above previously accepted decomposition temperatures, however the theoretical work describing the growth of InN using ionized nitrogen should be further explored. Further experimental work will need to be done to eliminate the effect of impurities and explore the growth parameter space to produce atomically flat films useful for semiconductor devices.

Work presented in this chapter was published in part in the Journal of Crystal Growth [107].

## 4 OPTOELECTRONIC MODELLING OF THIN LAYER INDIUM NITRIDE AND MULTILAYER STACKS

The measuring of semiconductor film can be accomplished using many methods. Secondary ion mass spectrometry (SIMS) uses an ion beam to bore into the material detecting changes in the ejected material to indicate material changes and measuring depth. Atomic force microscopy and stylus profilometry both physically measure the layer, but the layer needs to be etched away on part of the substrate to be able to measure the height difference of the material not etched away. These processes are destructive. Ideally, a non-destructive thickness measurement method would allow using grown material for other purposes. Implementing a non-destructive in-situ thickness measurements would allow sample growth progress monitoring. FTIR spectroscopy is a tool that could provide more information from in situ monitoring. FTIR spectroscopy generates a set of data that, if fitted with a theoretical material model, could give a measure of layer thickness, interface roughness, free electron concentration and phonon properties.

There have been several theoretical works studying optical response of thin films published by Kankanamge [106], Katsidis et al. [159,160], Schubert et al. [136,161], and Kasic et al. [162]. Kankanamge presented an extension of an isotropic, or single polarization light reflection model, treating each incident light polarization (s or p) as independent. Schubert and collaborators focus their modelling on understanding the ellipsometric data rather than applying their techniques to information obtained via infrared spectroscopy.

In this chapter I develop a theoretical model that can be used to fit the IR reflectance spectra of InN, or any other wurtzite material in form of a film. The measured (modelled) material can have any orientation with respect to the laboratory coordinate system and can be used with any linear light polarization.

## 4.1 Background

### 4.1.1 Multi-layer stack modelling – Generalized Transfer Matrix Method

The work in section 2.2.2 on the Fresnel coefficients,  $r$  and  $t$ , and reflectance can be extended to a multilayer stack of material. This is done by accounting for the phase change of the electric field along the optical path to calculate the effect on light passing through [159,160,163–167]. Katsidis et al. documents the method which they call the generalized transfer matrix method [160] and present a  $2 \times 2$  matrix to relate the incoming and outgoing fields at both interfaces of a layer of material. The components they model are the incoming and outgoing electric field. For an interface they define their matrix as

$$\begin{bmatrix} E_{im} \\ E_{rm} \end{bmatrix} = \frac{1}{t_{m,m+1}} \begin{bmatrix} 1 & r_{m,m+1} \\ r_{m,m+1} & 1 \end{bmatrix} \begin{bmatrix} E_{tm+1} \\ E_{bm+1} \end{bmatrix} \quad (4.1)$$

which can be written as:

$$\begin{bmatrix} E_{im} \\ E_{rm} \end{bmatrix} = \mathbf{S}_{m,m+1} \begin{bmatrix} E_{tm+1} \\ E_{bm+1} \end{bmatrix} \quad (4.2)$$

where  $E_i$  is the incoming field,  $E_r$  is the reflected field,  $E_t$  is the refracted field and  $E_b$  is the field approaching from the right as seen in Figure 4-1, and  $r_{m,m+1}$  and  $t_{m,m+1}$  are the Fresnel coefficients for the interface, as defined in chapter 2.

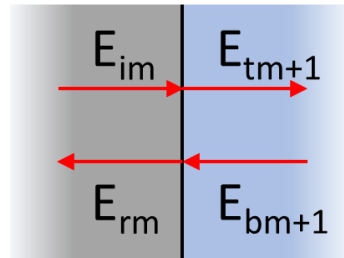


*Figure 4-1 Field components for generalized transfer matrix method at an interface. Note the arrows are not propagation or field vectors, but rather indicative of the approximate direction of field propagation associated with each electric field.*

Another element necessary for describing the propagation of fields through a material is the propagation matrix. This matrix defines the amplitude of each electric field as it reaches the next interface,  $E(d) = E(0)e^{iknd}$ , where  $d$  is distance the fields travel through the layer, the layer thickness and  $n$  is the index of refraction for the material. The product  $nd$  is called the optical thickness of the layer. So as can be seen in Figure 4-2, we have a representation of the field components in an isolated layer.

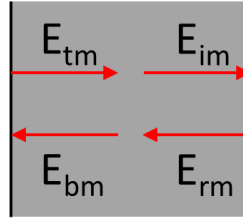


Figure 4-2 Field components for a propagation matrix of the generalized transfer matrix method

The transfer matrix across the  $m^{th}$  layer can then be written as:

$$\begin{bmatrix} E_{tm} \\ E_{bm} \end{bmatrix} = \begin{bmatrix} e^{ikn_md_m} & 1 \\ 1 & e^{-ikn_md_m} \end{bmatrix} \begin{bmatrix} E_{im} \\ E_{rm} \end{bmatrix} \quad (4.3)$$

By introducing the propagation matrix  $P_m$  equation (4.3) can be written as follows:

$$\begin{bmatrix} E_{tm} \\ E_{bm} \end{bmatrix} = \mathbf{P}_m \begin{bmatrix} E_{im} \\ E_{rm} \end{bmatrix} \quad (4.4)$$

The single layer model can be expanded to a stack of material layers by multiplying the appropriate number of interface matrices and propagation matrices. This will generate a single matrix for the system that can be used to find the optical response of an isotropic material for the case of normal light incidence with respect to the interface.

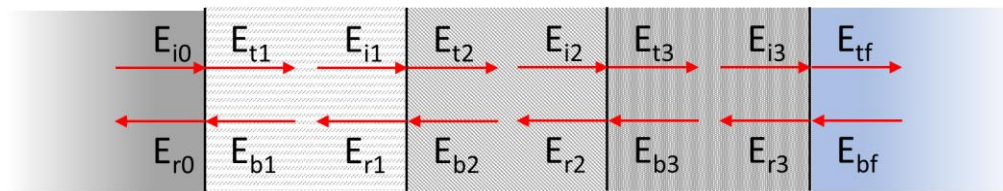


Figure 4-3 Field components for a 3-layer stack.

This is exemplified in Figure 4-3 for the case with 3 layers. This stack is comprised of 3 layers and 4 interfaces bound between two infinite slabs. The incident field,  $E_{i0}$  propagates from the left and reaches the first interface at  $90^\circ$ . For the actual measurement, the slab on the left could be air or the fluid the measurement is being made in. The slab on the right could be the substrate that has light entering it, but no light returning to the surface of the stack ( $E_{bf} = 0$ ). The transfer matrix for this system can be written as:

$$\begin{bmatrix} E_{i0} \\ E_{r0} \end{bmatrix} = \frac{1}{t_{0,1}} \begin{bmatrix} 1 & r_{0,1} \\ r_{0,1} & 1 \end{bmatrix} \begin{bmatrix} e^{ikn_1d_1} & 1 \\ 1 & e^{-ikn_1d_1} \end{bmatrix} \frac{1}{t_{1,2}} \begin{bmatrix} 1 & r_{1,2} \\ r_{1,2} & 1 \end{bmatrix} \begin{bmatrix} e^{ikn_2d_2} & 1 \\ 1 & e^{-ikn_2d_2} \end{bmatrix} \cdot \\ \frac{1}{t_{2,3}} \begin{bmatrix} 1 & r_{2,3} \\ r_{2,3} & 1 \end{bmatrix} \begin{bmatrix} e^{ikn_3d_3} & 1 \\ 1 & e^{-ikn_3d_3} \end{bmatrix} \frac{1}{t_{3,f}} \begin{bmatrix} 1 & r_{3,f} \\ r_{3,f} & 1 \end{bmatrix} \begin{bmatrix} E_{tf} \\ E_{bf} \end{bmatrix} \quad (4.5)$$

The expression (4.5) can be written in an abbreviated form by introducing interface matrices,  $S_{i,j}$  from equation (4.2) and the propagation matrices,  $P_{i,j}$  defined in equation (4.4).

$$\begin{bmatrix} E_{i0} \\ E_{r0} \end{bmatrix} = S_{0,1} P_1 S_{1,2} P_2 S_{2,3} P_3 S_{3,f} \begin{bmatrix} E_{tf} \\ E_{bf} \end{bmatrix} \quad (4.6)$$

For N layers this can be generalized to

$$\begin{bmatrix} E_{i0} \\ E_{r0} \end{bmatrix} = \prod_{m=0}^N (S_{m,m+1} P_m) S_{N,N+1} \begin{bmatrix} E_{tN+1} \\ E_{bN+1} \end{bmatrix} \quad (4.7)$$

which can be written as:

$$\begin{bmatrix} E_{i0} \\ E_{r0} \end{bmatrix} = \mathbf{T} \begin{bmatrix} E_{tN+1} \\ E_{bN+1} \end{bmatrix} \quad (4.8)$$

where  $\mathbf{T}$  is called the transfer matrix.

Assuming an isotropic medium, the difference between normal incident rays and an arbitrary angle is a modification of the optical path length to factor in the angle of the beam within

the material. So, the physical distance the light travels is  $d/\cos(\theta)$ , where  $\theta$  is the angle the light propagates with respect to the surface normal in the material. We also need to assume that the beam is wide enough compared to the optical thickness that edge effects can be ignored. The  $r$  and  $t$  functions derived in equation (2.8) can now be applied to the field at the beginning of the stack and at the last interface, so the reflectance and transmittance can be found.

The extension of this method to anisotropic cases is now necessary because the material I am analyzing is hexagonal, meaning there are differences when fields travel through material positioned at different orientations. When transitioning to an anisotropic medium the orientation of the principal axes of the material must be considered. Katsidis extended the applicability of the generalized transfer matrix to anisotropic materials by assuming that the principal axes of the material align with the surface of the material and the normal to that surface [159]. By using this geometry, a  $4 \times 4$  matrix was defined that addresses s- and p- polarized electric fields separately.

$$T_4 = \begin{bmatrix} T_{2s} & 0 \\ 0 & T_{2p} \end{bmatrix} \quad (4.9)$$

Here  $T_{2s}$  is the  $2 \times 2$  transfer matrix for s-polarized light and  $T_{2p}$  is the  $2 \times 2$  transfer matrix for p-polarized light. The electric field vector used in this form can be written as:

$$\begin{bmatrix} E_{ts} \\ E_{bs} \\ E_{tp} \\ E_{bp} \end{bmatrix} \quad (4.10)$$

While this model allows modeling the light transmission and reflection of multi-layer materials, it, at the same time, imposes very strict requirements on the crystallographic orientations of the studied material. In most cases it is very challenging to achieve even for epitaxial monocrystalline films. Moreover, this model cannot be used for polycrystalline material. An



example of such material is the InN films studied in this thesis (Chapter 3): they are polycrystalline grainy films, as proven by Raman spectroscopy, XRD and AFM measurements.

#### 4.1.2 Multi-layer stack modelling – Anisotropic media

In 1972 Berreman produced a differential formulation of a  $4 \times 4$  matrix to relate incoming and outgoing fields of a single layer of material [166]. Berreman defined the incoming and outgoing fields as the surface-parallel components of the electric and magnetic strength fields, seen in Figure 4-4. This means that there are no interfaces that need to be calculated as these field values are the same across an interface.

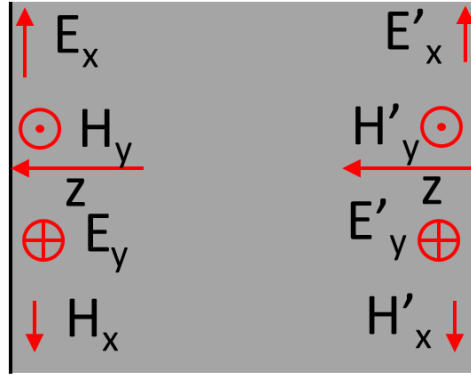


Figure 4-4 Surface parallel components of the electric and magnetic strength fields.

Schubert [163] explicitly defines the propagation matrix  $T_m$  in terms of the dielectric tensor (since, in this case, there are no assumptions about the isotropy or orientation of the material). His assumption of non-gyrotropic and non-magnetic material does not affect InN modeling. The matrix relationship between the fields at the top and the bottom of the layer can be written as:

$$\begin{bmatrix} E_x \\ E_y \\ H_x \\ H_y \end{bmatrix} = T_m \begin{bmatrix} E'_x \\ E'_y \\ H'_x \\ H'_y \end{bmatrix} \quad (4.11)$$

where  $T_m$  is defined as

$$T_m = \exp\left(i \frac{\omega}{c} \Delta d\right)$$

and  $\omega$  is the angular frequency of the field,  $c$  is the speed of light, and  $d$  is still the layer thickness.

$\Delta$  is defined as:

$$\Delta = \begin{bmatrix} -k_x \frac{\epsilon_{31}}{\epsilon_{33}} & -k_x \frac{\epsilon_{32}}{\epsilon_{33}} & 0 & 1 - \frac{k_x^2}{\epsilon_{33}} \\ 0 & 0 & -1 & 0 \\ \epsilon_{23} \frac{\epsilon_{31}}{\epsilon_{33}} - \epsilon_{21} & k_x^2 - \epsilon_{22} + \epsilon_{11} - \epsilon_{23} \frac{\epsilon_{32}}{\epsilon_{33}} & 0 & k_x \frac{\epsilon_{23}}{\epsilon_{33}} \\ \epsilon_{11} - \epsilon_{13} \frac{\epsilon_{31}}{\epsilon_{33}} & \epsilon_{12} - \epsilon_{13} \frac{\epsilon_{32}}{\epsilon_{33}} & 0 & -k_x \frac{\epsilon_{13}}{\epsilon_{33}} \end{bmatrix} \quad (4.12)$$

where  $k_x$  is the factor relating the wavevector in a vacuum to its  $x$ -component at the incident interface,  $k_x = n_i \sin(\theta_i)$ , where  $n_i$  is the index of refraction in the incident medium and  $\theta_i$  is the incident angle.  $\epsilon_{mn}$  are the components of the dielectric tensor which will be discussed in section 4.1.3.

The challenging part of calculating  $T_m$  is taking the exponential of the matrix found in equation (4.12). Berreman presents an approximation using a Taylor expansion that works for cases when film thicknesses are significantly less than the wavelength in the material. Wöhler et al. [168] presented a method that uses the Cayley-Hamilton theorem to truncate the approximation to the first 4 powers of the  $\Delta$  matrix (4.12), while removing the restriction on thickness, they rename the matrix  $P_m$  to differentiate.

$$P_m = \beta_0 \Delta^0 + \beta_1 \Delta + \beta_2 \Delta^2 + \beta_3 \Delta^3 \quad (4.13)$$

where  $\beta_n$  are defined in the following way:

$$\exp\left(i \frac{\omega}{c} \lambda_m d\right) = \sum_{n=0}^3 \beta_n \lambda_m^n \quad (4.14)$$

and  $\lambda_m$  are the eigenvalues of  $\Delta$ . This process is carried out for each layer in the stack with its respective values. The last piece of work needed is to convert the  $x$  and  $y$  electric and magnetic strength fields to the incident, reflected, transmitted and backward fields. These field components

transformations can be described by two matrices: the incident matrix,  $L_a$ , and the exit matrix,  $L_f$ , as notated by Schubert [163]. This means the entire light propagation process can be described by the entrance matrix, multiplied by the product of the propagation matrices for each layer multiplied by the exit matrix, as can be seen below:

$$\begin{bmatrix} E_{is0} \\ E_{rs0} \\ E_{ip0} \\ E_{rp0} \end{bmatrix} = L_a^{-1} \prod_{m=0}^N (P_m)^{-1} L_f \begin{bmatrix} E_{tsN+1} \\ E_{bsN+1} \\ E_{tpN+1} \\ E_{bpN+1} \end{bmatrix} \quad (4.15)$$

Knowing the dielectric tensor for the material would allow solving the equation (4.15) to find the required reflectance. Again, it should be noted, that this is subject to no light propagating into the bottom of the stack ( $E_b = 0$ ). The overall goal of the work presented in this chapter is to use this model to fit the experimental reflection data, thus extracting valuable sample information. As it is pointed out in Schubert [161], in order to discuss all the properties of the model, the entire reflectance spectrum needs to be fitted simultaneously, rather than utilizing point-by-point fitting of the spectrum. This presents a challenge to this method: for every measured frequency the reflectance needs to be calculated using the same model for the dielectric tensor at that frequency.

#### 4.1.3 Dielectric functions and tensors

The selection of a dielectric function  $\epsilon(\omega)$  for a material provides an opportunity to model different aspects of the material in order to compare them to data and get feedback on those properties.

The dielectric function is the relationship between how the electric field behaves in a vacuum compared to how it behaves in a material. By considering the response of an electron to an electric field, and its interaction with other electrons within the solid, we can define a simple model for the dielectric function. Berreman and Unterwald [169] call a different form of this equation the Helmholtz-Kettler uncoupled harmonic oscillator dispersion relation.

$$\frac{\epsilon(\omega)}{\epsilon_0} = 1 + \frac{Ne^2}{\epsilon_0} \sum_j \frac{f_j}{(\omega_j^2 - \omega^2 - i\omega\gamma_j)} \quad (4.16)$$

where  $N$  is the molecular concentration in the lattice,  $\omega_j$  is the binding frequency for the  $j^{th}$  type of electron oscillation, and  $\gamma_j$  is the damping constant for that resonance. The total number of oscillating electrons in each molecule,  $Z$ , must be equal to the sum of the oscillator strengths,  $f_j$ , i.e.  $\sum_j f_j = Z$ . As noted by Jackson [108] these values need “suitable quantum mechanical definition” in order to define an accurate relationship. This model of the dielectric function does not account for charges that are free to move in the material, which would add a term,  $-\omega_p^2/(\omega^2 + i\omega\gamma)$  for each species of free electron [161,170].  $\omega_p$  is the plasma frequency and is defined as:

$$\omega_p = \sqrt{ne^2/\epsilon_0 m^*} \quad (4.17)$$

where  $n$  is the free electron concentration and  $m^*$  is the effective mass of the free electron.

Berreman and Unterwald then expanded on work by Barker [171] to define a new relationship for the dielectric function [169]. Gervais and Piriou [172] present a form of that equation that is consistent with our notation:

$$\epsilon(\omega) = \epsilon_\infty \prod_j \frac{\omega_{jLO}^2 - \omega^2 + i\gamma_{jLO}\omega}{\omega_{jTO}^2 - \omega^2 + i\gamma_{jTO}\omega} \quad (4.18)$$

where  $\omega_{jLO}$ ,  $\gamma_{jLO}$ , and  $\omega_{jTO}$ ,  $\gamma_{jTO}$ , are the frequencies and damping coefficients for the  $j^{th}$  LO and TO phonon modes.  $\epsilon_\infty$  is the high frequency dielectric constant.

Another form of dielectric function which would be most suited to InN films would be a form which couples the phonon response with a plasmon response due to the high free electron concentration observed in Hall measurements (section 3.3.5). Kukharskii [173] presents a formulation of the dielectric function where this coupling is considered. Kasic et al. [162] present an equation for  $\epsilon$  using similar notation to the work done in this chapter so far:

$$\epsilon(\omega) = \epsilon_{\infty} \frac{\prod_j (\omega^2 + i\gamma_{jLPP}\omega - \omega_{jLPP}^2)}{(\omega^2 + i\gamma_p\omega)(\omega^2 + i\gamma_{TO}\omega - \omega_{TO}^2)} \quad (4.19)$$

where the combined plasmon/phonon damping term  $\gamma_{jLPP}$  is unique for each combined excitation frequency. And the corresponding frequency is defined as

$$\omega_{LPP}^2 = \frac{1}{2} \left[ \omega_p^2 + \omega_{LO}^2 + (-1)^j \sqrt{(\omega_p^2 + \omega_{LO}^2)^2 - 4\omega_p^2\omega_{TO}^2} \right] \quad (4.20)$$

This method does assume that the wavenumber is small in comparison to the size of the reciprocal lattice. This restriction does not apply to the study of InN as the reciprocal lattice is on the order of  $10^8 \text{ cm}^{-1}$  and the target frequencies for analysis are less than  $10^4 \text{ cm}^{-1}$  [162].

The dielectric function (4.19) can be derived for each crystal axis.  $\epsilon(\omega)$  along the parallel and perpendicular components to the c-axis of the crystal (see Figure 1-7) form the diagonal terms of the dielectric tensor:

$$\epsilon = \begin{bmatrix} \epsilon_{\perp} & 0 & 0 \\ 0 & \epsilon_{\perp} & 0 \\ 0 & 0 & \epsilon_{\parallel} \end{bmatrix} \quad (4.21)$$

The tensor can then be rotated to arbitrary orientations using rotation matrices, to establish the orientation of the crystal with respect to the established coordinate system [163].

Using this theoretical work, the goal is to model the reflectance of multilayer stack to gain information about the properties of each individual layer in the stack such as plasma frequency, and thickness. The orientation of the crystal structure, or grains, and strains within the crystal are not known so there must be an allowance for variation in phonon frequencies and damping coefficients. There are also crystalline defects which are not accounted for within the model (in the dielectric function) that may need to be included to better match the data.

## 4.2 MATLAB Script for fitting FTIR data

The model described above was programmed in the MATLAB software package. The fitting code can be found in appendix B. The fitting program is broken into three main portions. The first defines the initial oscillator parameters and the search range for modifying those initial parameters. For this model the list of parameters that can be changed is given in Table 4-1.

*Table 4-1 Table of Fitting parameters for FTIR model*

Perpendicular polarization	Parallel polarization	Polarization independent
$\epsilon_{\infty\perp}$	$\epsilon_{\infty\parallel}$	$\omega_p$
$\omega_{LO\perp}, \omega_{TO\perp}$	$\omega_{LO\parallel}, \omega_{TO\parallel}$	$\gamma_{LPP-}, \gamma_{LPP+}$
$\gamma_{TO\perp}$	$\gamma_{TO\parallel}$	$d$
		$\theta_c$

Here  $\theta_c$  is the rotation of the c-axis of the crystal with respect to the surface normal of the film.

At this point interface roughness has not been incorporated in the modelling. Katsidis and Siapakas present a model that should be investigated and perhaps incorporated [160].

The value of the high-frequency dielectric constant for InN is not found to be consistent within literature:  $\epsilon_{\infty} = 6.7$  [162], 7.73 [174], 8.3 [159]. This is most likely an artifact of the multivariable nature of this problem. The other phonon parameters are initialized close to values found in the sources for the high frequency dielectric constant and allowed to vary. The sample thickness is initialized as a best guess based on growth factors and previous models.

Each of these parameters is set to vary independently and randomly within the range specified, having an equal probability (defined by MATLAB's random number generator) to move above or below the initialized value. Each iteration of the program produces a number of sample

value sets to be used to calculate a number of model reflectances. These new random value sets are then used to calculate the parallel and perpendicular dielectric function.

The second step is to calculate the  $\Delta$  matrix. The orientation of the c-axis is randomly selected, and the lattice-oriented dielectric tensor is transformed into the film-oriented dielectric tensor for each measured wavenumber. Using Schubert's method [161] the  $\Delta$  matrix is calculated for each wavenumber and then the eigenvalues for those matrices are found.

In order to maintain continuity in the components of the field associated with each eigenvalue, the eigenvalues are sorted and attempts are made to check that each eigenvalue forms part of a continuous function in frequency space. Once the eigenvalues are sorted, equation (4.14) is solved for  $\beta$  vectors and the propagation matrix, equation (4.13), for each layer can be found.

After the propagation matrix is found, it is combined with the transform matrices to convert the electric and magnetic field strength terms to the s- and p- polarized incoming, reflected, transmitted, and backward (which we assume to be zero) electric fields and calculate the model reflectance. In the case the calculated reflectance value is greater than one (due to a computational error) that reflectance is set to zero.

The last step is to compare the model reflectance for each of the models calculated with the experimental reflectance. I find the root mean square error (RMSE) between the models and data and select the input parameter set associated with the minimum RMSE value from the iteration to define the new initialization values for the model. This process is repeated until the minimum RMSE is less than a set value. At this point the modelled reflectance, experimental reflectance and all the fit parameters are stored, and can be used to analyze the material.

### 4.3 FTIR Modelling Results

The experimentally acquired FTIR reflectance spectrum of InN was used to test the model fitting operation. The reflectance spectrum of the sample 1167 (InN film grown at 957°C, see Table 3-1 for details) was chosen. Sample parameters were initialized to the values shown in Table 4-2.

*Table 4-2 Initial values for FTIR reflectance model. Note:  $\theta_c$  is limited to values between 0 and  $\pi/2$*

	Initial Value	Variation allowed in one iteration of the model
$\epsilon_{\infty\perp}$	7.7	0.5
$\epsilon_{\infty\parallel}$	7.7	0.5
$\omega_{LO\perp}$	582	100
$\omega_{TO\perp}$	465	10
$\omega_{LO\parallel}$	568	100
$\omega_{TO\parallel}$	423	10
$\gamma_{TO\perp}$	2.9	1
$\gamma_{TO\parallel}$	3.94	1
$\omega_p$	3500	500
$\gamma_{LPP-}$	12	0.2
$\gamma_{LPP+}$	375	6
$l$	55	10
$\theta_c$	$\pi/4$	$\pi/4$



The MATLAB script was run until the RMSE was 0.0160. The modelling results and experimental reflectivity graphs are plotted in Figure 4-5. As can be seen in the figure, there is good agreement between the model and the data, except for a couple of features. The two absorption dips around  $2100\text{ cm}^{-1}$ , likely originating from sample impurities [144], are not accounted for in the current model, therefore it is expected that the model and data would not match at that wavenumber range. The other points where there seems to be a disagreement is at about  $410\text{ cm}^{-1}$  and  $525\text{ cm}^{-1}$ . These wavenumber values are near phonon frequencies and are likely a result of issues caused by finding the eigenvalues of the  $\Delta$  matrix.

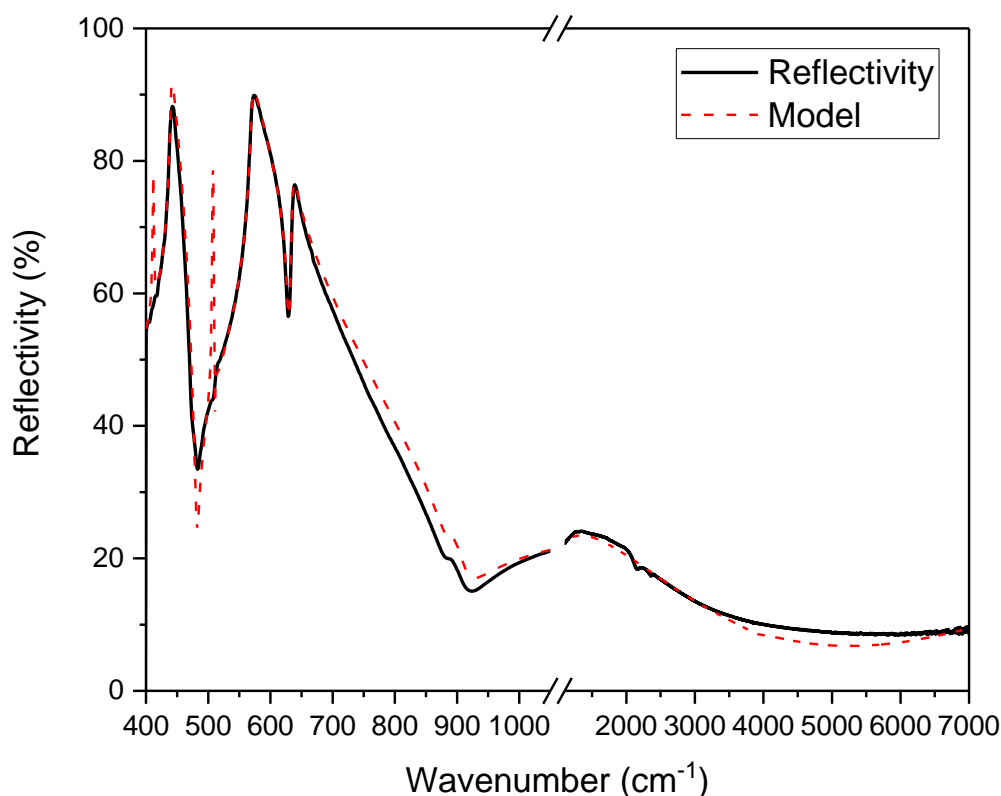


Figure 4-5 Experimental reflectance and modelled reflectance for sample 1167

The features between 400 and 900  $\text{cm}^{-1}$  correspond to the phonon resonances of InN and the sapphire substrate. For sapphire, the phonon features are expected at 439  $\text{cm}^{-1}$ , 481  $\text{cm}^{-1}$ , 511  $\text{cm}^{-1}$ , 569  $\text{cm}^{-1}$ , 582  $\text{cm}^{-1}$ , 630  $\text{cm}^{-1}$ , 634  $\text{cm}^{-1}$  and 881  $\text{cm}^{-1}$  [136]. Maxima and minima are found near those points as expected. Except for the unexpected dips around 2100  $\text{cm}^{-1}$  the data from 900 to 7000  $\text{cm}^{-1}$  are thickness related changes in reflectance. The fitting results for the InN film are summarized in Table 4-3. Parameter errors are half of the variation allowed, meaning this is at least a local minima for the model.

*Table 4-3 Model parameters found in fitting program*

	Model Values
$\epsilon_{\infty\perp}$	$6.71\pm0.25$
$\epsilon_{\infty\parallel}$	$7.74\pm0.25$
$\omega_{LO\perp}$	$378.8\pm50$
$\omega_{TO\perp}$	$507.0\pm5$
$\omega_{LO\parallel}$	$368.5\pm50$
$\omega_{TO\parallel}$	$411.5\pm5$
$\gamma_{TO\perp}$	$5.8\pm0.5$
$\gamma_{TO\parallel}$	$1.2\pm0.5$
$\omega_p$	$3928\pm250$
$\gamma_{LPP-}$	$12.3\pm0.1$
$\gamma_{LPP+}$	$379\pm25$
$l$	$46.3\pm5$
$\theta_c$	$1.51\pm \pi/8$

Since the angle of the c-axis with respect to the surface normal is close to  $\pi/2$ , it can be reasonably assumed that the parallel ( $A_1$ ) and perpendicular components ( $E_1$ ) components are switched with and the c-axis is actually at an angle of 0.061 radians relative to the surface normal. The position of the two TO branch frequencies (411 and 507  $\text{cm}^{-1}$ ) seem to coincide with the

irregularities seen in the model. As the variation in phonon frequency is large, this could be an artifact and needs to be refined by tightening the variation allowed in phonon frequencies.

The plasma frequency found in this model is related to the free electron concentration and the effective mass of the electron in the lattice  $m^*$  in the InN layer using (4.17). This can be used to evaluate either the effective mass of the electron assuming a constant free electron concentration, or vice versa. Using the free electron concentration of  $1.5 \times 10^{19} \text{ cm}^{-3}$  found in section 3.3.5 we can calculate an effective mass of  $8.57m_0$  where  $m_0$  is the free electron mass. This effective mass is significantly larger than the currently accepted value of less than  $0.1m_0$  [175–179].

#### 4.4 Conclusion

The significant differences between modelled values and previously accepted values point to significant work that needs to be done in refining the model. The ability to produce a model for the entire spectrum and fit that is enticing, but the challenges of finding the eigenvalues of a matrix and keeping them in the “correct” order in order to calculate the entire spectrum is a daunting task. This model shows potential, but it would need to be extended beyond the calculation of a single layer, and work will need to be done to identify or generate good models for the dielectric function that accurately model reflectance behavior. The large effective mass could be attributed to poor crystallinity of InN over a large scale.

This model does produce a reflectance which satisfactorily fits the experimental data. At the same time there is plenty of room for its refinement. In contrast to previously developed models, it does fit the full spectrum simultaneously and allows working with polycrystalline materials.

## 5 CONCLUSIONS

The challenge of refining the synthesis of InN to the point of commercial viability and to be able to alloy it with GaN and AlN is a formidable challenge as evidenced by the last 30 to 40 years of research. This work represents another small step in the field of InN growth. It expands the parameter range accessible to InN growth to include higher growth temperatures. Reflectance modeling also expands existing characterization techniques and contributes to understanding of InN interaction with electromagnetic waves.

In this work I documented the growth of InN above its previously reported decomposition temperature. This is one of the possible first steps toward InN-based heterostructures and high indium content alloys with GaN and AlN. I also extended the current models for calculating reflectance for materials for the purpose of extracting data from FTIR reflectance spectra. This will allow researchers to better understand their materials and aid in the comparison of samples for future study.

### 5.1 High-temperature growth of InN

Chapter 3 documents the deposition of indium nitride on sapphire at growth temperatures from 700 to 957 °C. I was able to demonstrate the presence of polycrystalline InN of varying thicknesses at all growth temperatures. All growth temperatures that I explored were above the InN decomposition temperature. This growth was achieved by changing the physics of the reaction to form InN, from using an atomic or molecular form of nitrogen to using ionized nitrogen directly. It is important to note that in my experiment the temperature was limited arbitrarily, the growth parameters were being tested and the highest growth rate was the deciding factor for further work.

There is no apparent reason that InN cannot be grown using MEPA-MOCVD at higher temperatures than documented in this work. While this is an important contribution to the field of

InN growth, it remains mostly unexplored. More work needs to be done to refine the quality of material produced. The goal of growing atomically flat epitaxial layers is tackled in two parts, material growth and substrate effects. This work addresses the field of growth and expanding the parameters that are accessible to growing InN.

The substrate affects the initiation of that growth, such that even if growth is achieved it may be polycrystalline and disordered, as we have demonstrated. For this growth process more work needs to be done to understand the preparation a substrate needs, or growth initiation steps, for improved epitaxial growth.

The fact that growth is achieved at temperatures up to 957°C opens the possibilities to combine the growth of InN with GaN or AlN. Being able to grow these materials that typically require growth temperature of around 1000 °C on high-quality InN films would allow for the growth of InN-based semiconductor heterostructures. If this is realized, the demonstrated brilliance of GaN-based optoelectronic devices could be expanded into the IR spectral range. Lower energy detectors and emitters are not far off, and the potential for better harvesting of solar energy is something that needs to be explored.

## **5.2 FTIR modelling of InN and multilayer structures**

The modelling work done in chapter 4 is an extension of spectroscopic ellipsometry techniques to FTIR data. Being able extract some of the same information regarding bulk crystal orientation and surface quality, as well as phonon modes and layer thickness, all from one set of data would elucidate the materials being studied and give a lot of feedback that can be correlated with other measurements to establish a better understanding of the material and its properties. Extending this modelling to multiple layers is not accomplished yet, but this is something that I

am planning on carrying out in the future. This work will increase the amount of information that can be gathered in situ during growth to serve as real-time feedback for future growth.

## REFERENCES

- [1] S. Ploch, C. Meissner, M. Pristovsek, M. Kneissl, Shape of indium nitride quantum dots and nanostructures grown by metal organic vapour phase epitaxy, *Phys. Status Solidi (c)*. 6 (2009) S574–S577. <https://doi.org/10.1002/pssc.200880938>.
- [2] O. Briot, B. Maleyre, S. Ruffenach, Indium nitride quantum dots grown by metalorganic vapor phase epitaxy, *Appl. Phys. Lett.* 83 (2003) 2919–2921. <https://doi.org/10.1063/1.1613044>.
- [3] D. González, J.G. Lozano, M. Herrera, N.D. Browning, S. Ruffenach, O. Briot, R. García, Structural changes during the natural aging process of InN quantum dots, *Journal of Applied Physics*. 105 (2009) 013527. <https://doi.org/10.1063/1.3010309>.
- [4] A. Moelbjerg, P. Kaer, M. Lorke, J. Mørk, Resonance Fluorescence from Semiconductor Quantum Dots: Beyond the Mollow Triplet, *Phys. Rev. Lett.* 108 (2012) 017401. <https://doi.org/10.1103/PhysRevLett.108.017401>.
- [5] B. Tekcan, S. Alkis, M. Alevli, N. Dietz, B. Ortaç, N. Biyikli, A.K. Okyay, A Near-Infrared Range Photodetector Based on Indium Nitride Nanocrystals Obtained Through Laser Ablation, *IEEE Electron Device Letters*. 35 (2014) 936–938. <https://doi.org/10.1109/LED.2014.2336795>.
- [6] Z. Liu, R. Beaulac, Nature of the Infrared Transition of Colloidal Indium Nitride Nanocrystals: Nonparabolicity Effects on the Plasmonic Behavior of Doped Semiconductor Nanomaterials, *Chem. Mater.* 29 (2017) 7507–7514. <https://doi.org/10.1021/acs.chemmater.7b02545>.
- [7] A. Shetty, K.J. Vinoy, S.B. Krupanidhi, A Study on the Suitability of Indium Nitride for Terahertz Plasmonics, (n.d.) 5.
- [8] J.I. Pankove, E.A. Miller, D. Richman, J.E. Berkeyheiser, Electroluminescence in GaN, *Journal of Luminescence*. 4 (1971) 63–66. [https://doi.org/10.1016/0022-2313\(71\)90009-3](https://doi.org/10.1016/0022-2313(71)90009-3).
- [9] H. Amano, M. Kito, K. Hiramatsu, I. Akasaki, P-Type Conduction in Mg-Doped GaN Treated with Low-Energy Electron Beam Irradiation (LEEBI), *Jpn. J. Appl. Phys.* 28 (1989) L2112–L2114. <https://doi.org/10.1143/JJAP.28.L2112>.
- [10] I. Akasaki, H. Amano, Conductivity Control of AlGaIn. Fabrication of AlGaIn/GaN Multi-Heterostructure and their Application to UV/Blue Light Emitting Devices, *MRS Proc.* 242 (1992) 383. <https://doi.org/10.1557/PROC-242-383>.
- [11] S. Nakamura, M. Senoh, T. Mukai, High-power InGaIn/GaN double-heterostructure violet light emitting diodes, *Appl. Phys. Lett.* 62 (1993) 2390–2392. <https://doi.org/10.1063/1.109374>.
- [12] S. Nakamura, M. Senoh, T. Mukai, P-GaN/N-InGaIn/N-GaN Double-Heterostructure Blue-Light-Emitting Diodes, *Japanese Journal of Applied Physics*. 32 (1993) L8–L11. <https://doi.org/10.1143/JJAP.32.L8>.
- [13] M.R. Krames, O.B. Shchekin, R. Mueller-Mach, G.O. Mueller, L. Zhou, G. Harbers, M.G. Craford, Status and Future of High-Power Light-Emitting Diodes for Solid-State Lighting, *J. Display Technol.* 3 (2007) 160–175. <https://doi.org/10.1109/JDT.2007.895339>.
- [14] S. Nakamura, M. Senoh, S. Nagahama, N. Iwasa, T. Yamada, T. Matsushita, H. Kiyoku, Y. Sugimoto, InGaIn-Based Multi-Quantum-Well-Structure Laser Diodes, *Japanese Journal of Applied Physics*. 35 (1996) L74–L76. <https://doi.org/10.1143/JJAP.35.L74>.

- [15] W. Terashima, N. Kamata, H. Hirayama, Realization of unexplored frequency terahertz quantum-cascade lasers by using III nitride semiconductors, in: 2016 International Semiconductor Laser Conference (ISLC), 2016: pp. 1–2.
- [16] J. Wu, W. Walukiewicz, K.M. Yu, W. Shan, J.W. Ager, E.E. Haller, H. Lu, W.J. Schaff, W.K. Metzger, S. Kurtz, Superior radiation resistance of In<sub>1-x</sub>Ga<sub>x</sub>N alloys: Full-solar-spectrum photovoltaic material system, *Journal of Applied Physics*. 94 (2003) 6477–6482. <https://doi.org/10.1063/1.1618353>.
- [17] A. Yamamoto, M. Tsujino, M. Ohkubo, A. Hashimoto, Metalorganic chemical vapor deposition growth of InN for InN/Si tandem solar cell, *Solar Energy Materials and Solar Cells*. 35 (1994) 53–60. [https://doi.org/10.1016/0927-0248\(94\)90122-8](https://doi.org/10.1016/0927-0248(94)90122-8).
- [18] P. Aliberti, Y. Feng, Y. Takeda, S.K. Shrestha, M.A. Green, G. Conibeer, Investigation of theoretical efficiency limit of hot carriers solar cells with a bulk indium nitride absorber, *Journal of Applied Physics*. 108 (2010) 094507. <https://doi.org/10.1063/1.3494047>.
- [19] Rashid, STABILITY ANALYSIS OF SOLAR CELL CHARACTERISTICS ABOVE ROOM TEMPERATURE USING INDIUM NITRIDE BASED QUANTUM DOT, *American Journal of Applied Sciences*. 10 (2013) 1345–1350. <https://doi.org/10.3844/ajassp.2013.1345.1350>.
- [20] Y. Feng, P. Aliberti, B.P. Veetil, R. Patterson, S. Shrestha, M.A. Green, G. Conibeer, Non-ideal energy selective contacts and their effect on the performance of a hot carrier solar cell with an indium nitride absorber, *Appl. Phys. Lett.* 100 (2012) 053502. <https://doi.org/10.1063/1.3680594>.
- [21] S. Alkis, F.I. Chowdhury, M. Alevli, N. Dietz, B. Yalızay, S. Aktürk, A. Nayfeh, A.K. Okyay, Enhancement of polycrystalline silicon solar cells efficiency using indium nitride particles, *J. Opt.* 17 (2015) 105903. <https://doi.org/10.1088/2040-8978/17/10/105903>.
- [22] A.S.A. Fletcher, D. Nirmal, A survey of Gallium Nitride HEMT for RF and high power applications, *Superlattices and Microstructures*. 109 (2017) 519–537. <https://doi.org/10.1016/j.spmi.2017.05.042>.
- [23] R. Juza, H. Hahn, Über die Kristallstrukturen von Cu<sub>3</sub>N, GaN und InN Metallamide und Metallnitride, *Z. Anorg. Allg. Chem.* 239 (1938) 282–287. <https://doi.org/10.1002/zaac.19382390307>.
- [24] G. Brauer, ed., *Handbook of Preparative Inorganic Chemistry*, 2nd ed., Academic Press, New York, 1963. [https://s3.amazonaws.com/academia.edu.documents/59932219/Preparative\\_Inorganic\\_Chemistry\\_Brauer20190704-105818-j8ja34.pdf](https://s3.amazonaws.com/academia.edu.documents/59932219/Preparative_Inorganic_Chemistry_Brauer20190704-105818-j8ja34.pdf) (accessed March 24, 2020).
- [25] G.V. Samsonov, *Nitridiy, Naukova Dumka, Kiyev*, 1969. <https://apps.dtic.mil/dtic/tr/fulltext/u2/712413.pdf> (accessed March 24, 2020).
- [26] Th. Renner, Herstellung der Nitride von Bor, Aluminium, Gallium und Indium nach dem Aufwachsverfahren, *Z. Anorg. Allg. Chem.* 298 (1959) 22–33. <https://doi.org/10.1002/zaac.19592980106>.
- [27] G.V. Samsonov, M.D. Lyutaya, Preparation and properties of Indium Nitride, *Zhurnal Prikladnoi Khimii*. 36 (1963) 1416–1420.
- [28] N. Sclar, Energy Gaps of the III–V and the (Rare Earth)-V Semiconductors, *Journal of Applied Physics*. 33 (1962) 2999–3002. <https://doi.org/10.1063/1.1728552>.
- [29] In: *Progress in Dielectrics*, John Wiley & Sons, New York, 1959: p. 219.
- [30] E.E. Loebner, The future of electroluminescent solids in display applications, *Proc. IEEE*. 61 (1973) 837–861. <https://doi.org/10.1109/PROC.1973.9174>.



- [31] B.F. Ormont, O Shirine Zapreshchennoi zony ryada soedinene A (III) B (V), Zhurnal Neorganicheskoi Khimii. 4 (n.d.) 2176–2177.
- [32] N.E. Alekseevski, G.V. Samsonov, O.I. Shulishova, SUPERCONDUCTIVITY OF GALLIUM NITRIDES, Zh. Eksperim. i Teor. Fiz., 44 (1963).
- [33] J.B. MacChesney, P.M. Bridenbaugh, P.B. O'Connor, Thermal stability of indium nitride at elevated temperatures and nitrogen pressures, Materials Research Bulletin. 5 (1970) 783–791. [https://doi.org/10.1016/0025-5408\(70\)90028-0](https://doi.org/10.1016/0025-5408(70)90028-0).
- [34] H.J. Hovel, J.J. Cuomo, Electrical and Optical Properties of rf-Sputtered GaN and InN, Appl. Phys. Lett. 20 (1972) 71–73. <https://doi.org/10.1063/1.1654051>.
- [35] N. Puychevri, M. Menoret, Synthesis of III–V semiconductor nitrides by reactive cathodic sputtering, Thin Solid Films. 36 (1976) 141–145. [https://doi.org/10.1016/0040-6090\(76\)90423-5](https://doi.org/10.1016/0040-6090(76)90423-5).
- [36] M. Yamaguchi, Thermal Nitridation of InP, Jpn. J. Appl. Phys. 19 (1980) L401–L404. <https://doi.org/10.1143/JJAP.19.L401>.
- [37] T.L. Tansley, C.P. Foley, Optical band gap of indium nitride, Journal of Applied Physics. 59 (1986) 3241–3244. <https://doi.org/10.1063/1.336906>.
- [38] B.T. Sullivan, R.R. Parsons, K.L. Westra, M.J. Brett, Optical properties and microstructure of reactively sputtered indium nitride thin films, Journal of Applied Physics. 64 (1988) 4144–4149. <https://doi.org/10.1063/1.341326>.
- [39] T.L. Tansley, C.P. Foley, Infrared absorption in indium nitride, Journal of Applied Physics. 60 (1986) 2092–2095. <https://doi.org/10.1063/1.337213>.
- [40] C.P. Foley, T.L. Tansley, Morphology and structure of indium nitride films, Applications of Surface Science. 22–23 (1985) 663–669. [https://doi.org/10.1016/0378-5963\(85\)90199-0](https://doi.org/10.1016/0378-5963(85)90199-0).
- [41] T.J. Kistenmacher, D. Dayan, R. Fainchtein, W.A. Bryden, J.S. Morgan, T.O. Poehler, Substrate and Temperature Dependent Morphology of rf-Sputtered Indium Nitride Films, MRS Proc. 162 (1989) 573. <https://doi.org/10.1557/PROC-162-573>.
- [42] T.L. Tansley, C.P. Foley, Electron mobility in indium nitride, Electronics Letters. 20 (1984) 1066–1068. <https://doi.org/10.1049/el:19840729>.
- [43] C.P. Foley, T.L. Tansley, Pseudopotential band structure of indium nitride, Phys. Rev. B. 33 (1986) 1430–1433. <https://doi.org/10.1103/PhysRevB.33.1430>.
- [44] S.N. Grinyaev, V.Ya. Malakhov, V.A. Chaldyshev, Calculation of the band structure of GaN and InN using the pseudopotential method, Soviet Physics Journal. 29 (1986) 311–314. <https://doi.org/10.1007/BF00893005>.
- [45] K.L. Westra, R.P.W. Lawson, M.J. Brett, The effects of oxygen contamination on the properties of reactively sputtered indium nitride films, Journal of Vacuum Science & Technology A: Vacuum, Surfaces, and Films. 6 (1988) 1730–1732. <https://doi.org/10.1116/1.575280>.
- [46] L.A. Marasina, I.G. Pichugin, M. Tlaczala, Preparation of InN epitaxial layers in InCl<sub>3</sub>-NH<sub>3</sub> system, Kristall Und Technik. 12 (1977) 541–545. <https://doi.org/10.1002/crat.19770120603>.
- [47] A. Wakahara, A. Yoshida, Heteroepitaxial growth of InN by microwave-excited metalorganic vapor phase epitaxy, Appl. Phys. Lett. 54 (1989) 709–711. <https://doi.org/10.1063/1.100870>.
- [48] A. Wakahara, T. Tsuchiya, A. Yoshida, Epitaxial layers of indium nitride by microwave-excited metalorganic vapor phase epitaxy, Vacuum. 41 (1990) 1071–1073. [https://doi.org/10.1016/0042-207X\(90\)93870-O](https://doi.org/10.1016/0042-207X(90)93870-O).

- [49] A. Wakahara, T. Tsuchiya, A. Yoshida, Epitaxial growth of indium nitride, *Journal of Crystal Growth*. 99 (1990) 385–389. [https://doi.org/10.1016/0022-0248\(90\)90549-Z](https://doi.org/10.1016/0022-0248(90)90549-Z).
- [50] T.L. Tansley, Li Xin, Ma Yanhua, Argon fluoride laser activated deposition of nitride films, *Thin Solid Films*. 163 (1988) 255–259. [https://doi.org/10.1016/0040-6090\(88\)90432-4](https://doi.org/10.1016/0040-6090(88)90432-4).
- [51] W.A. Bryden, T.J. Kistenmacher, D.K. Wickenden, J.S. Morgan, A.E. Wickenden, S.A. Ecelberger, T.O. Poehler, METAL NITRIDE SEMICONDUCTORS FOR OPTICAL APPLICATIONS, *John Hopkins APL Technical Digest*. 10 (1989) 11.
- [52] W.M. Lau, X. Feng, I. Bello, S. Sant, K.K. Foo, R.P.W. Lawson, Construction, characterization and applications of a compact mass-resolved low-energy ion beam system, *Nuclear Instruments and Methods in Physics Research Section B: Beam Interactions with Materials and Atoms*. 59–60 (1991) 316–320. [https://doi.org/10.1016/0168-583X\(91\)95231-2](https://doi.org/10.1016/0168-583X(91)95231-2).
- [53] I. Bello, W.M. Lau, R.P.W. Lawson, K.K. Foo, Deposition of indium nitride by low energy modulated indium and nitrogen ion beams, *Journal of Vacuum Science & Technology A: Vacuum, Surfaces, and Films*. 10 (1992) 1642–1646. <https://doi.org/10.1116/1.577763>.
- [54] Q. Guo, O. Kato, A. Yoshida, Thermal stability of indium nitride single crystal films, *Journal of Applied Physics*. 73 (1993) 7969–7971. <https://doi.org/10.1063/1.353906>.
- [55] W.E. Hoke, P.J. Lemonias, D.G. Weir, Evaluation of a new plasma source for molecular beam epitaxial growth of InN and GaN films, *Journal of Crystal Growth*. 111 (1991) 1024–1028. [https://doi.org/10.1016/0022-0248\(91\)91125-T](https://doi.org/10.1016/0022-0248(91)91125-T).
- [56] A. Munoz, K. Kunc, Structure and static properties of indium nitride at low and moderate pressures, *J. Phys.: Condens. Matter*. 5 (1993) 6015–6022. <https://doi.org/10.1088/0953-8984/5/33/010>.
- [57] S. Strite, D. Chandrasekhar, D.J. Smith, J. Sariel, H. Chen, N. Teraguchi, H. Morkoç, Structural properties of InN films grown on GaAs substrates: observation of the zincblende polytype, *Journal of Crystal Growth*. 127 (1993) 204–208. [https://doi.org/10.1016/0022-0248\(93\)90605-V](https://doi.org/10.1016/0022-0248(93)90605-V).
- [58] Q. Xia, H. Xia, A.L. Ruoff, NEW CRYSTAL STRUCTURE OF INDIUM NITRIDE: A PRESSURE-INDUCED ROCKSALT PHASE, *Mod. Phys. Lett. B*. 08 (1994) 345–350. <https://doi.org/10.1142/S0217984994000352>.
- [59] Y. Sato, S. Sato, Growth of InN thin films by hydride vapor phase epitaxy, *Journal of Crystal Growth*. 144 (1994) 15–19. [https://doi.org/10.1016/0022-0248\(94\)90004-3](https://doi.org/10.1016/0022-0248(94)90004-3).
- [60] D.A. Neumayer, J.G. Ekerdt, Growth of Group III Nitrides. A Review of Precursors and Techniques, *Chem. Mater*. 8 (1996) 9–25. <https://doi.org/10.1021/cm950108r>.
- [61] V.W.L. Chin, T.L. Tansley, T. Osotchan, Electron mobilities in gallium, indium, and aluminum nitrides, *Journal of Applied Physics*. 75 (1994) 7365–7372. <https://doi.org/10.1063/1.356650>.
- [62] T. Inushima, T. Yaguchi, A. Nagase, A. Iso, T. Shiraishi, S. Ooya, Optical and electrical properties of InN grown by the atomic layer epitaxy, in: *Seventh International Conference on Indium Phosphide and Related Materials*, 1995: pp. 187–190. <https://doi.org/10.1109/ICIPRM.1995.522110>.
- [63] F. Ren, S.J. Pearton, J.R. Lothian, S.N.G. Chu, W.K. Chu, R.G. Wilson, C.R. Abernathy, S.S. Pei, Low resistance ohmic contacts on nitrogen ion bombarded InP, *Appl. Phys. Lett*. 65 (1994) 2165–2167. <https://doi.org/10.1063/1.112750>.

- [64] J.S. Pan, A.T.S. Wee, C.H.A. Huan, H.S. Tan, K.L. Tan, XPS studies on nitridation of InP(100) surface by ion beam bombardment, *J. Phys. D: Appl. Phys.* 29 (1996) 2997–3002. <https://doi.org/10.1088/0022-3727/29/12/010>.
- [65] Y. Sato, S. Sato, InN thin-film growth using an ECR plasma source, *Materials Science and Engineering: B*. 35 (1995) 171–175. [https://doi.org/10.1016/0921-5107\(95\)01344-X](https://doi.org/10.1016/0921-5107(95)01344-X).
- [66] O. Ambacher, Thermal stability and desorption of Group III nitrides prepared by metal organic chemical vapor deposition, *Journal of Vacuum Science & Technology B: Microelectronics and Nanometer Structures*. 14 (1996) 3532. <https://doi.org/10.1116/1.588793>.
- [67] J.S. Dyck, K. Kash, C.C. Hayman, A. Argoitia, M.T. Grossner, J.C. Angus, W.-L. Zhou, Synthesis of bulk polycrystalline indium nitride at subatmospheric pressures, *J. Mater. Res.* 14 (1999) 2411–2417. <https://doi.org/10.1557/JMR.1999.0324>.
- [68] Q. Guo, M. Nishio, H. Ogawa, A. Yoshida, Low-Temperature Growth of InN Films on (111)GaAs Substrates, *Jpn. J. Appl. Phys.* 38 (1999) L490–L491. <https://doi.org/10.1143/JJAP.38.L490>.
- [69] F.E. Fernandez, M. Pumarol, A. Martinez, W. Jia, Y. Wang, E. Rodriguez, H.A. Mourad, Advances in pulsed laser deposition growth of nitride thin films, in: J.J. Dubowski, H. Helvajian, E.-W. Kreutz, K. Sugioka (Eds.), San Jose, CA, 1999: pp. 475–486. <https://doi.org/10.1117/12.352706>.
- [70] F. Yang, Y. Yang, J. Hwang, C. Lee, K. Chen, C. Lin, High-growth rate epitaxy of InN film by a novel-design MOCVD, in: Y.-K. Su, P. Bhattacharya (Eds.), Taipei, Taiwan, 2000: p. 500. <https://doi.org/10.1117/12.392179>.
- [71] H. Lu, W.J. Schaff, J. Hwang, H. Wu, W. Yeo, A. Pharkya, L.F. Eastman, Improvement on epitaxial grown of InN by migration enhanced epitaxy, *Appl. Phys. Lett.* 77 (2000) 2548–2550. <https://doi.org/10.1063/1.1318235>.
- [72] Y. Horikoshi, Advanced epitaxial growth techniques: atomic layer epitaxy and migration-enhanced epitaxy, *Journal of Crystal Growth*. 201–202 (1999) 150–158. [https://doi.org/10.1016/S0022-0248\(98\)01314-1](https://doi.org/10.1016/S0022-0248(98)01314-1).
- [73] R.W. Cumberland, R.G. Blair, C.H. Wallace, T.K. Reynolds, R.B. Kaner, Thermal Control of Metathesis Reactions Producing GaN and InN<sup>†</sup>, *J. Phys. Chem. B*. 105 (2001) 11922–11927. <https://doi.org/10.1021/jp0126558>.
- [74] V.Y. Davydov, A.A. Klochikhin, R.P. Seisyan, V.V. Emtsev, S.V. Ivanov, F. Bechstedt, J. Furthmüller, H. Harima, A.V. Mudryi, J. Aderhold, O. Semchinova, J. Graul, Absorption and Emission of Hexagonal InN. Evidence of Narrow Fundamental Band Gap, *Physica Status Solidi (b)*. 229 (2002) r1–r3. [https://doi.org/10.1002/1521-3951\(200202\)229:3<R1::AID-PSSB99991>3.0.CO;2-O](https://doi.org/10.1002/1521-3951(200202)229:3<R1::AID-PSSB99991>3.0.CO;2-O).
- [75] J. Wu, W. Walukiewicz, K.M. Yu, J.W.A. Iii, E.E. Haller, H. Lu, W.J. Schaff, Indium nitride: A narrow gap semiconductor, (n.d.) 9.
- [76] K.S.A. Butcher, M. Wintrebert-Fouquet, Indium Nitride Emerges, (2002) 4.
- [77] Z.G. Qian, W.Z. Shen, H. Ogawa, Q.X. Guo, Infrared reflection characteristics in InN thin films grown by magnetron sputtering for the application of plasma filters, *Journal of Applied Physics*. 92 (2002) 3683–3687. <https://doi.org/10.1063/1.1506199>.
- [78] Z.G. Qian, G. Yu, W.Z. Shen, H. Ogawa, Q.X. Guo, Growth-dependent phonon characteristics in InN thin films, *Physica B: Condensed Matter*. 318 (2002) 180–187. [https://doi.org/10.1016/S0921-4526\(02\)00569-0](https://doi.org/10.1016/S0921-4526(02)00569-0).

- [79] B.R. Nag, On the band gap of indium nitride, *Physica Status Solidi (b)*. 237 (2003) R1–R2. <https://doi.org/10.1002/pssb.200301823>.
- [80] K.S.A. Butcher, T.L. Tansley, InN, latest development and a review of the band-gap controversy, *Superlattices and Microstructures*. 38 (2005) 1–37. <https://doi.org/10.1016/j.spmi.2005.03.004>.
- [81] E. Burstein, Anomalous Optical Absorption Limit in InSb, *Phys. Rev.* 93 (1954) 632–633. <https://doi.org/10.1103/PhysRev.93.632>.
- [82] A.G. Bhuiyan, T. Tanaka, A. Yamamoto, A. Hashimoto, Laser-Assisted Metalorganic Vapor-Phase Epitaxy (LMOVPE) of Indium Nitride (InN), *Physica Status Solidi (a)*. 194 (2002) 502–505. [https://doi.org/10.1002/1521-396X\(200212\)194:2<502::AID-PSSA502>3.0.CO;2-2](https://doi.org/10.1002/1521-396X(200212)194:2<502::AID-PSSA502>3.0.CO;2-2).
- [83] A.G. Bhuiyan, A. Yamamoto, A. Hashimoto, Y. Ito, High temperature growth of InN on GaP(111)B substrate using a new two-step growth method, *Journal of Crystal Growth*. 236 (2002) 59–65. [https://doi.org/10.1016/S0022-0248\(01\)02155-8](https://doi.org/10.1016/S0022-0248(01)02155-8).
- [84] V. Woods, J. Senawirante, N. Dietz, Nucleation and growth of InN by high-pressure chemical vapor deposition: Optical monitoring, *J. Vac. Sci. Technol. B*. 23 (2005) 1790. <https://doi.org/10.1116/1.1943444>.
- [85] R. Atalay, M. Buegler, S. Gamage, M.K.I. Senevirathna, B. Küçükçök, A.G. Melton, A. Hoffmann, A.G.U. Perera, I.T. Ferguson, N. Dietz, Effect of V/III molar ratio on the structural and optical properties of InN epilayers grown by HPCVD, in: M.H. Kane, C. Wetzel, J.-J. Huang, I.T. Ferguson (Eds.), San Diego, California, USA, 2012: p. 84840X. <https://doi.org/10.1117/12.930199>.
- [86] M. Buegler, S. Gamage, R. Atalay, J. Wang, M.K.I. Senevirathna, R. Kirste, T. Xu, M. Jamil, I. Ferguson, J. Tweedie, R. Collazo, A. Hoffmann, Z. Sitar, N. Dietz, Growth temperature and growth rate dependency on reactor pressure for InN epilayers grown by HPCVD, *Physica Status Solidi (c)*. 8 (2011) 2059–2062. <https://doi.org/10.1002/pssc.201001067>.
- [87] G. Durkaya, M. Buegler, R. Atalay, I. Senevirathna, M. Alevli, O. Hitzemann, M. Kaiser, R. Kirste, A. Hoffmann, N. Dietz, The influence of the group V/III molar precursor ratio on the structural properties of InGaN layers grown by HPCVD, *Physica Status Solidi (a)*. 207 (2010) 1379–1382. <https://doi.org/10.1002/pssa.200983622>.
- [88] S. Ruffenach, M. Moret, O. Briot, B. Gil, Recent advances in the MOVPE growth of indium nitride, *Physica Status Solidi (a)*. 207 (2010) 9–18. <https://doi.org/10.1002/pssa.200982642>.
- [89] R. Togashi, T. Kamoshita, H. Adachi, H. Murakami, Y. Kumagai, A. Koukitu, Investigation of polarity dependent InN0001 decomposition in N<sub>2</sub> and H<sub>2</sub> ambient, *Physica Status Solidi c*. 6 (2009) S372–S375. <https://doi.org/10.1002/pssc.200880894>.
- [90] S.-Y. Kwon, Z. Ren, Q. Sun, J. Han, Y.-W. Kim, E. Yoon, B.H. Kong, H.K. Cho, I.-J. Kim, H. Cheong, Observation of oxide precipitates in InN nanostructures, *Applied Physics Letters*. 91 (2007) 234102. <https://doi.org/10.1063/1.2822396>.
- [91] G. Pettinari, F. Masia, M. Capizzi, A. Polimeni, M. Losurdo, G. Bruno, T.H. Kim, S. Choi, A. Brown, V. Lebedev, V. Cimalla, O. Ambacher, Experimental evidence of different hydrogen donors in n -type InN, *Phys. Rev. B*. 77 (2008) 125207. <https://doi.org/10.1103/PhysRevB.77.125207>.
- [92] D. González, J.G. Lozano, M. Herrera, F.M. Morales, S. Ruffenach, O. Briot, R. García, Phase mapping of aging process in InN nanostructures: oxygen incorporation and the role of the zinc blende phase, *Nanotechnology*. 21 (2010) 185706. <https://doi.org/10.1088/0957-4484/21/18/185706>.

- [93] H. Vollstädt, E. Ito, M. Akaishi, S. Akimoto, O. Fukunaga, High pressure synthesis of rocksalt type of AlN., *Proceedings of the Japan Academy. Ser. B: Physical and Biological Sciences.* 66 (1990) 7–9. <https://doi.org/10.2183/pjab.66.7>.
- [94] M. Ueno, A. Onodera, O. Shimomura, K. Takemura, X-ray observation of the structural phase transition of aluminum nitride under high pressure, *Phys. Rev. B.* 45 (1992) 10123–10126. <https://doi.org/10.1103/PhysRevB.45.10123>.
- [95] P. Perlin, C. Jauberthie-Carillon, J.P. Itie, A. San Miguel, I. Grzegory, A. Polian, Raman scattering and x-ray-absorption spectroscopy in gallium nitride under high pressure, *Phys. Rev. B.* 45 (1992) 83–89. <https://doi.org/10.1103/PhysRevB.45.83>.
- [96] D. Nilsson, E. Janzén, A. Kakanakova-Georgieva, Lattice parameters of AlN bulk, homoepitaxial and heteroepitaxial material, *J. Phys. D: Appl. Phys.* 49 (2016) 175108. <https://doi.org/10.1088/0022-3727/49/17/175108>.
- [97] V. Darakchieva, B. Monemar, A. Usui, On the lattice parameters of GaN, *Appl. Phys. Lett.* 91 (2007) 031911. <https://doi.org/10.1063/1.2753122>.
- [98] B. Maleyre, S. Ruffenach, O. Briot, A. van der Lee, Lattice parameters of relaxed wurtzite indium nitride powder obtained by MOCVD, *Superlattices and Microstructures.* 36 (2004) 527–535. <https://doi.org/10.1016/j.spmi.2004.09.052>.
- [99] S.S. Liu, Growth Kinetics and Catalytic Effects in the Vapor Phase Epitaxy of Gallium Nitride, *J. Electrochem. Soc.* 125 (1978) 1161. <https://doi.org/10.1149/1.2131641>.
- [100] Z. Ahmad, G.B. Cross, M. Vernon, D. Gebregiorgis, D. Deocampo, A. Kozhanov, Influence of plasma-activated nitrogen species on PA-MOCVD of InN, *Appl. Phys. Lett.* 115 (2019) 223101. <https://doi.org/10.1063/1.5126625>.
- [101] S. Nakamura, GaN Growth Using GaN Buffer Layer, *Jpn. J. Appl. Phys.* 30 (1991) L1705–L1707. <https://doi.org/10.1143/JJAP.30.L1705>.
- [102] T. Yuasa, Y. Ueta, Y. Tsuda, A. Ogawa, M. Taneya, K. Takao, Effect of Slight Misorientation of Sapphire Substrate on Metalorganic Chemical Vapor Deposition Growth of GaN, *Jpn. J. Appl. Phys.* 38 (1999) L703–L705. <https://doi.org/10.1143/JJAP.38.L703>.
- [103] D. Lu, D.I. Florescu, D.S. Lee, V. Merai, J.C. Ramer, A. Parekh, E.A. Armour, Sapphire substrate misorientation effects on GaN nucleation layer properties, *Journal of Crystal Growth.* 272 (2004) 353–359. <https://doi.org/10.1016/j.jcrysgro.2004.08.113>.
- [104] A. Yamamoto, Y. Yamauchi, M. Ohkubo, A. Hashimoto, T. Saitoh, Heteroepitaxial growth of InN on Si(111) using a GaAs intermediate layer, *Solid-State Electronics.* 41 (1997) 149–154. [https://doi.org/10.1016/S0038-1101\(96\)00156-6](https://doi.org/10.1016/S0038-1101(96)00156-6).
- [105] D. Seidlitz, M.K.I. Senevirathna, Y. Abate, A. Hoffmann, N. Dietz, Optoelectronic and structural properties of InGaN nanostructures grown by plasma-assisted MOCVD, in: M.H. Kane, J. Jiao, N. Dietz, J.-J. Huang (Eds.), *Fourteenth International Conference on Solid State Lighting and LED-Based Illumination Systems*, SPIE, San Diego, California, United States, 2015: p. 95710P. <https://doi.org/10.1117/12.2188612>.
- [106] I.M. Kankanamge, *Optoelectronic and Structural Properties of Group III-Nitride Semiconductors Grown by High Pressure MOCVD and Migration Enhance Plasma Assisted MOCVD*, Georgia State University, 2016.
- [107] G.B. Cross, Z. Ahmad, D. Seidlitz, M. Vernon, N. Dietz, D. Deocampo, D. Gebregiorgis, S. Lei, A. Kozhanov, Kinetically stabilized high-temperature InN growth, *Journal of Crystal Growth.* 536 (2020) 125574. <https://doi.org/10.1016/j.jcrysgro.2020.125574>.
- [108] J.D. Jackson, *Classical electrodynamics*, 3rd ed, Wiley, New York, 1999.

- [109] L.J. van der Pauw, A Method of Measuring the Resistivity and Hall Coefficient on Lamellae of Arbitrary Shape, Philips Technical Review. 20 (1958) 222–224.
- [110] J.D. Weiss, R.J. Kaplar, K.E. Kambour, A derivation of the van der Pauw formula from electrostatics, Solid-State Electronics. 52 (2008) 91–98. <https://doi.org/10.1016/j.sse.2007.07.029>.
- [111] R. Chwang, B.J. Smith, C.R. Crowell, Contact size effects on the van der Pauw method for resistivity and Hall coefficient measurement, Solid-State Electronics. 17 (1974) 1217–1227. [https://doi.org/10.1016/0038-1101\(74\)90001-X](https://doi.org/10.1016/0038-1101(74)90001-X).
- [112] A.A. Ramadan, R.D. Gould, A. Ashour, On the Van der Pauw method of resistivity measurements, Thin Solid Films. 239 (1994) 272–275. [https://doi.org/10.1016/0040-6090\(94\)90863-X](https://doi.org/10.1016/0040-6090(94)90863-X).
- [113] S. Young Moon, J. Ho Son, K. Jin Choi, J.-L. Lee, H.W. Jang, Indium as an efficient ohmic contact to N-face  $n$ -GaIn of GaN-based vertical light-emitting diodes, Appl. Phys. Lett. 99 (2011) 202106. <https://doi.org/10.1063/1.3662421>.
- [114] M. Kučera, A. Adikimenakis, E. Dobročka, R. Kúdela, M. Ťapajna, A. Laurenčíková, A. Georgakilas, J. Kuzmík, Structural, electrical, and optical properties of annealed InN films grown on sapphire and silicon substrates, Thin Solid Films. 672 (2019) 114–119. <https://doi.org/10.1016/j.tsf.2019.01.006>.
- [115] A.R. Acharya, S. Gamage, M.K.I. Senevirathna, M. Alevli, K. Bahadir, A.G. Melton, I. Ferguson, N. Dietz, B.D. Thoms, Thermal stability of InN epilayers grown by high pressure chemical vapor deposition, Applied Surface Science. 268 (2013) 1–5. <https://doi.org/10.1016/j.apsusc.2012.10.184>.
- [116] R. Aleksiejūnas, Ž. Podlipskas, S. Nargelas, A. Kadys, M. Kolenda, K. Nomeika, J. Mickevičius, G. Tamulaitis, Direct Auger recombination and density-dependent hole diffusion in InN, Scientific Reports. 8 (2018). <https://doi.org/10.1038/s41598-018-22832-6>.
- [117] Y.N. Buzynin, O.I. Khrykin, P.A. Yunin, M.N. Drozdov, A.Y. Luk'yanov, InN Layers Grown by MOCVD on a-Plane Al<sub>2</sub>O<sub>3</sub>, Physica Status Solidi (a). 215 (2018) 1700919. <https://doi.org/10.1002/pssa.201700919>.
- [118] C.C. Lund, Metal-Organic Chemical Vapor Deposition of N-Polar InGaIn and InN for Electronic Devices, Ph.D., University of California, Santa Barbara, 2018. <https://search.proquest.com/docview/2023582136/abstract/EC95C3FB539B43B7PQ/1> (accessed March 1, 2019).
- [119] M. Drago, P. Vogt, W. Richter, MOVPE growth of InN with ammonia on sapphire, Physica Status Solidi (a). 203 (2006) 116–126. <https://doi.org/10.1002/pssa.200563527>.
- [120] T. Shioda, M. Sugiyama, Y. Shimogaki, Y. Nakano, Kinetic Analysis of InN Selective Area Metal–Organic Vapor Phase Epitaxy, Appl. Phys. Express. 1 (2008) 071102. <https://doi.org/10.1143/APEX.1.071102>.
- [121] S. Porowski, Growth and properties of single crystalline GaIn substrates and homoepitaxial layers, Materials Science and Engineering: B. 44 (1997) 407–413. [https://doi.org/10.1016/S0921-5107\(96\)01730-8](https://doi.org/10.1016/S0921-5107(96)01730-8).
- [122] C.D. Thurmond, R.A. Logan, The Equilibrium Pressure of N<sub>2</sub> over GaIn, J. Electrochem. Soc. 119 (1972) 622. <https://doi.org/10.1149/1.2404274>.
- [123] V. Woods, N. Dietz, InN growth by high-pressures chemical vapor deposition: Real-time optical growth characterization, Materials Science and Engineering: B. 127 (2006) 239–250. <https://doi.org/10.1016/j.mseb.2005.10.032>.

- [124] N. Dietz, M. Straßburg, V. Woods, Real-time optical monitoring of ammonia flow and decomposition kinetics under high-pressure chemical vapor deposition conditions, *Journal of Vacuum Science & Technology A: Vacuum, Surfaces, and Films*. 23 (2005) 1221–1227. <https://doi.org/10.1116/1.1894422>.
- [125] N. Dietz, M. Alevli, V. Woods, M. Strassburg, H. Kang, I.T. Ferguson, The characterization of InN growth under high-pressure CVD conditions, *Phys. Stat. Sol. (b)*. 242 (2005) 2985–2994. <https://doi.org/10.1002/pssb.200562246>.
- [126] O. Bierwagen, S. Choi, J.S. Speck, Hall and Seebeck profiling: Determining surface, interface, and bulk electron transport properties in unintentionally doped InN, *Physical Review B*. 84 (2011). <https://doi.org/10.1103/PhysRevB.84.235302>.
- [127] G. Koblmüller, C.S. Gallinat, J.S. Speck, Surface kinetics and thermal instability of N-face InN grown by plasma-assisted molecular beam epitaxy, *Journal of Applied Physics*. 101 (2007) 083516. <https://doi.org/10.1063/1.2718884>.
- [128] T.A. Komissarova, E. Kampert, J. Law, V.N. Jmerik, P. Paturi, X. Wang, A. Yoshikawa, S.V. Ivanov, Electrical properties of surface and interface layers of the N- and In-polar undoped and Mg-doped InN layers grown by PA MBE, *Applied Physics Letters*. 112 (2018) 022104. <https://doi.org/10.1063/1.5009794>.
- [129] T.A. Komissarova, P. Wang, P. Paturi, X. Wang, S.V. Ivanov, Influence of MBE growth modes and conditions on spontaneous formation of metallic In nanoparticles and electrical properties of InN matrix, *Journal of Crystal Growth*. 478 (2017) 216–219. <https://doi.org/10.1016/j.jcrysgro.2017.09.010>.
- [130] X. Feng, H. Peng, J. Gong, W. Wang, H. Liu, Z. Quan, S. Pan, L. Wang, Epitaxial growth of InN thin films by plasma-enhanced atomic layer deposition, *Journal of Applied Physics*. 124 (2018) 243104. <https://doi.org/10.1063/1.5054155>.
- [131] M. Higashiwaki, T. Matsui, High-Quality InN Film Grown on a Low-Temperature-Grown GaN Intermediate Layer by Plasma-Assisted Molecular-Beam Epitaxy, *Jpn. J. Appl. Phys.* 41 (2002) L540–L542. <https://doi.org/10.1143/JJAP.41.L540>.
- [132] M.K.I. Senevirathna, D. Seidlitz, A. Fali, B. Cross, Y. Abate, N. Dietz, Effect of AlN buffer layers on the structural and optoelectronic properties of InN/AlN/Sapphire heterostructures grown by MEPA-MOCVD, in: M.H. Kane, N. Dietz, I.T. Ferguson (Eds.), San Diego, California, United States, 2016: p. 99540R. <https://doi.org/10.1117/12.2237957>.
- [133] M. Wojdyr, *Fityk*: a general-purpose peak fitting program, *J Appl Crystallogr.* 43 (2010) 1126–1128. <https://doi.org/10.1107/S0021889810030499>.
- [134] K. Levenberg, A method for the solution of certain non-linear problems in least squares, *Quart. Appl. Math.* 2 (1944) 164–168. <https://doi.org/10.1090/qam/10666>.
- [135] D.W. Marquardt, An Algorithm for Least-Squares Estimation of Nonlinear Parameters, *Journal of the Society for Industrial and Applied Mathematics*. 11 (1963) 431–441. <https://doi.org/10.1137/0111030>.
- [136] M. Schubert, T.E. Tiwald, C.M. Herzinger, Infrared dielectric anisotropy and phonon modes of sapphire, *Physical Review B*. 61 (2000) 8187–8201. <https://doi.org/10.1103/PhysRevB.61.8187>.
- [137] G. Kaczmarczyk, A. Kaschner, S. Reich, A. Hoffmann, C. Thomsen, D.J. As, A.P. Lima, D. Schikora, K. Lischka, R. Averbeck, H. Riechert, Lattice dynamics of hexagonal and cubic InN: Raman-scattering experiments and calculations, *Appl. Phys. Lett.* 76 (2000) 2122–2124. <https://doi.org/10.1063/1.126273>.

- [138] M. Kuball, J.W. Pomeroy, M. Wintrebert-Fouquet, K.S.A. Butcher, H. Lu, W.J. Schaff, A Raman spectroscopy study of InN, *Journal of Crystal Growth*. 269 (2004) 59–65. <https://doi.org/10.1016/j.jcrysgro.2004.05.034>.
- [139] F. Demangeot, C. Pinquier, J. Frandon, M. Gaio, O. Briot, B. Maleyre, S. Ruffenach, B. Gil, Raman scattering by the longitudinal optical phonon in InN: Wave-vector nonconserving mechanisms, *Physical Review B*. 71 (2005). <https://doi.org/10.1103/PhysRevB.71.104305>.
- [140] J.S. Thakur, D. Haddad, V.M. Naik, R. Naik, G.W. Auner, H. Lu, W.J. Schaff, A 1 (LO) phonon structure in degenerate InN semiconductor films, *Physical Review B*. 71 (2005). <https://doi.org/10.1103/PhysRevB.71.115203>.
- [141] A.G. Kontos, Y.S. Raptis, N.T. Pelekanos, A. Georgakilas, E. Bellet-Amalric, D. Jalabert, Micro-Raman characterization of In<sub>x</sub>Ga<sub>1-x</sub>N/GaN/Al<sub>2</sub>O<sub>3</sub> heterostructures, *Physical Review B*. 72 (2005). <https://doi.org/10.1103/PhysRevB.72.155336>.
- [142] V.Yu. Davydov, A.A. Klochikhin, Electronic and vibrational states in InN and In<sub>x</sub>Ga<sub>1-x</sub>N solid solutions, *Semiconductors*. 38 (2004) 861–898. <https://doi.org/10.1134/1.1787109>.
- [143] C. Park, W.-S. Jung, Z. Huang, T.J. Anderson, In situ Raman spectroscopic studies of trimethylindium pyrolysis in an OMVPE reactor, *J. Mater. Chem.* 12 (2002) 356–360. <https://doi.org/10.1039/b107586a>.
- [144] M.W. Chase, NIST-JANAF Thermochemical Tables, 4th ed., American Institute of Physics, 1998.
- [145] M.K.I. Senevirathna, S. Gamage, R. Atalay, A.R. Acharya, A.G. Unil Perera, N. Dietz, M. Buegler, A. Hoffmann, L. Su, A. Melton, I. Ferguson, Effect of reactor pressure on the electrical and structural properties of InN epilayers grown by high-pressure chemical vapor deposition, *Journal of Vacuum Science & Technology A: Vacuum, Surfaces, and Films*. 30 (2012) 031511. <https://doi.org/10.1116/1.4705727>.
- [146] IR Spectrum Table & Chart, Sigma-Aldrich. (n.d.). <https://www.sigmaaldrich.com/technical-documents/articles/biology/ir-spectrum-table.html> (accessed October 24, 2019).
- [147] A.G. Bhuiyan, A. Hashimoto, A. Yamamoto, Indium nitride (InN): A review on growth, characterization, and properties, *Journal of Applied Physics*. 94 (2003) 2779–2808. <https://doi.org/10.1063/1.1595135>.
- [148] D. Nečas, P. Klapetek, Gwyddion: an open-source software for SPM data analysis, *Open Physics*. 10 (2012). <https://doi.org/10.2478/s11534-011-0096-2>.
- [149] F. Gao, Y. Guan, J. Li, J. Gao, J. Guo, G. Li, Epitaxial growth and interfaces of high-quality InN films grown on nitrided sapphire substrates, *J. Mater. Res.* 28 (2013) 1239–1244. <https://doi.org/10.1557/jmr.2013.67>.
- [150] M. Moret, S. Ruffenach, O. Briot, B. Gil, MOVPE growth and characterization of indium nitride on C-, A-, M-, and R-plane sapphire, *Physica Status Solidi (a)*. 207 (2010) 24–28. <https://doi.org/10.1002/pssa.200982641>.
- [151] Y. Huang, H. Wang, Q. Sun, J. Chen, J.F. Wang, Y.T. Wang, H. Yang, Study on the thermal stability of InN by in-situ laser reflectance system, *Journal of Crystal Growth*. 281 (2005) 310–317. <https://doi.org/10.1016/j.jcrysgro.2005.04.055>.
- [152] V.I. Korepanov, S.-Y. Chan, H.-C. Hsu, H. Hamaguchi, Phonon confinement and size effect in Raman spectra of ZnO nanoparticles, *Heliyon*. 5 (2019) e01222. <https://doi.org/10.1016/j.heliyon.2019.e01222>.



- [153] H. Lu, W.J. Schaff, L.F. Eastman, C.E. Stutz, Surface charge accumulation of InN films grown by molecular-beam epitaxy, *Appl. Phys. Lett.* 82 (2003) 1736–1738. <https://doi.org/10.1063/1.1562340>.
- [154] R.P. Bhatta, B.D. Thoms, M. Alevli, N. Dietz, Surface electron accumulation in indium nitride layers grown by high pressure chemical vapor deposition, *Surface Science*. 601 (2007) L120–L123. <https://doi.org/10.1016/j.susc.2007.07.018>.
- [155] R.P. Bhatta, B.D. Thoms, A. Weerasekera, A.G.U. Perera, M. Alevli, N. Dietz, Carrier concentration and surface electron accumulation in indium nitride layers grown by high pressure chemical vapor deposition, *Journal of Vacuum Science & Technology A: Vacuum, Surfaces, and Films*. 25 (2007) 967–970. <https://doi.org/10.1116/1.2712185>.
- [156] A. Denisenko, C. Pietzka, A. Chuvilin, U. Kaiser, H. Lu, W.J. Schaff, E. Kohn, Depletion of surface accumulation charge in InN by anodic oxidation, *Journal of Applied Physics*. 105 (2009) 033702. <https://doi.org/10.1063/1.3073930>.
- [157] T.D. Veal, I. Mahboob, L.F.J. Piper, C.F. McConville, H. Lu, W.J. Schaff, Indium nitride: Evidence of electron accumulation, *J. Vac. Sci. Technol. B*. 22 (2004) 2175. <https://doi.org/10.1116/1.1771672>.
- [158] L. Colakerol, T.D. Veal, H.-K. Jeong, L. Plucinski, A. DeMasi, T. Learmonth, P.-A. Glans, S. Wang, Y. Zhang, L.F.J. Piper, P.H. Jefferson, A. Fedorov, T.-C. Chen, T.D. Moustakas, C.F. McConville, K.E. Smith, Quantized Electron Accumulation States in Indium Nitride Studied by Angle-Resolved Photoemission Spectroscopy, *Physical Review Letters*. 97 (2006). <https://doi.org/10.1103/PhysRevLett.97.237601>.
- [159] C.C. Katsidis, A.O. Ajagunna, A. Georgakilas, Optical characterization of free electron concentration in heteroepitaxial InN layers using Fourier transform infrared spectroscopy and a  $2 \times 2$  transfer-matrix algebra, *Journal of Applied Physics*. 113 (2013) 073502. <https://doi.org/10.1063/1.4792259>.
- [160] C.C. Katsidis, D.I. Siapkas, General transfer-matrix method for optical multilayer systems with coherent, partially coherent, and incoherent interference, *Appl. Opt.* 41 (2002) 3978. <https://doi.org/10.1364/AO.41.003978>.
- [161] M. Schubert, *Infrared ellipsometry on semiconductor layer structures: phonons, plasmons, and polaritons*, Springer, Berlin ; New York, 2004.
- [162] A. Kasic, M. Schubert, Y. Saito, Y. Nanishi, G. Wagner, Effective electron mass and phonon modes in  $n$ -type hexagonal InN, *Phys. Rev. B*. 65 (2002) 115206. <https://doi.org/10.1103/PhysRevB.65.115206>.
- [163] M. Schubert, Polarization-dependent optical parameters of arbitrarily anisotropic homogeneous layered systems, *Physical Review B*. 53 (1996) 4265–4274. <https://doi.org/10.1103/PhysRevB.53.4265>.
- [164] F. Abelès, Recherches sur la propagation des ondes électromagnétiques sinusoïdales dans les milieux stratifiés: Application aux couches minces, *Ann. Phys.* 12 (1950) 596–640. <https://doi.org/10.1051/anphys/195012050596>.
- [165] P. Yeh, Optics of anisotropic layered media: A new  $4 \times 4$  matrix algebra, *Surface Science*. 96 (1980) 41–53. [https://doi.org/10.1016/0039-6028\(80\)90293-9](https://doi.org/10.1016/0039-6028(80)90293-9).
- [166] D.W. Berreman, Optics in Stratified and Anisotropic Media:  $4 \times 4$  Matrix Formulation, *Journal of the Optical Society of America*. 62 (1972) 502–510.
- [167] P. Yeh, *Optical waves in layered media*, Wiley, New York, 1988.

- [168] H. Wöhler, G. Haas, M. Fritsch, D.A. Mlynski, Faster  $4 \times 4$  matrix method for uniaxial inhomogeneous media, J. Opt. Soc. Am. A. 5 (1988) 1554. <https://doi.org/10.1364/JOSAA.5.001554>.
- [169] D.W. Berreman, F.C. Unterwald, Adjusting Poles and Zeros of Dielectric Dispersion to Fit Reststrahlen of Pr Cl<sub>3</sub> and La Cl<sub>3</sub>, Phys. Rev. 174 (1968) 791–799. <https://doi.org/10.1103/PhysRev.174.791>.
- [170] C. Kittel, Introduction to solid state physics, 8th ed, Wiley, Hoboken, NJ, 2005.
- [171] A.S. Barker, Transverse and Longitudinal Optic Mode Study in Mg F<sub>2</sub> and Zn F<sub>2</sub>, Phys. Rev. 136 (1964) A1290–A1295. <https://doi.org/10.1103/PhysRev.136.A1290>.
- [172] F. Gervais, B. Piriou, Anharmonicity in several-polar-mode crystals: adjusting phonon self-energy of LO and TO modes in Al<sub>2</sub>O<sub>3</sub> and TiO<sub>2</sub> to fit infrared reflectivity, J. Phys. C: Solid State Phys. 7 (1974) 2374–2386. <https://doi.org/10.1088/0022-3719/7/13/017>.
- [173] A.A. Kukharskii, Plasmon-phonon coupling in GaAs, Solid State Communications. 13 (1973) 1761–1765. [https://doi.org/10.1016/0038-1098\(73\)90724-2](https://doi.org/10.1016/0038-1098(73)90724-2).
- [174] C. Bungaro, K. Rapcewicz, J. Bernholc, *Ab initio* phonon dispersions of wurtzite AlN, GaN, and InN, Phys. Rev. B. 61 (2000) 6720–6725. <https://doi.org/10.1103/PhysRevB.61.6720>.
- [175] M. Goiran, M. Millot, J.-M. Poumirol, I. Gherasoiu, W. Walukiewicz, J. Leotin, Electron cyclotron effective mass in indium nitride, Appl. Phys. Lett. 96 (2010) 052117. <https://doi.org/10.1063/1.3304169>.
- [176] J. Wu, W. Walukiewicz, W. Shan, K.M. Yu, J.W. Ager, E.E. Haller, H. Lu, W.J. Schaff, Effects of the narrow band gap on the properties of InN, Phys. Rev. B. 66 (2002) 201403. <https://doi.org/10.1103/PhysRevB.66.201403>.
- [177] S.P. Fu, Y.F. Chen, Effective mass of InN epilayers, Appl. Phys. Lett. 85 (2004) 1523–1525. <https://doi.org/10.1063/1.1787615>.
- [178] T. Inushima, M. Higashiwaki, T. Matsui, Optical properties of Si-doped InN grown on sapphire (0001), Phys. Rev. B. 68 (2003) 235204. <https://doi.org/10.1103/PhysRevB.68.235204>.
- [179] G. Pettinari, A. Polimeni, M. Capizzi, J.H. Blokland, P.C.M. Christianen, J.C. Maan, V. Lebedev, V. Cimalla, O. Ambacher, Carrier mass measurements in degenerate indium nitride, Phys. Rev. B. 79 (2009) 165207. <https://doi.org/10.1103/PhysRevB.79.165207>.

## APPENDICES

### Appendix A Mathematica Script to find the Matrix representations of the Reflected field ( $E_r$ ) and Refracted Field ( $E_t$ ), as a function of the incident field ( $E_i$ )

```

Solve[{Sqrt[ε1/μ1]*(Ep+Erp)==Sqrt[ε2/μ2]Etp,(Ep-
Erp)*Cos[i]==Etp*Cos[r],Es+Ers==Ets, Sqrt[ε1/μ1]*(Es-
Ers)*Cos[i]==Sqrt[ε2/μ2]*Ets*Cos[r]},{Erp,Ers,Etp,Ets},{Ex,Ey}]

{ {Erp -> -((Ep*Cos[r]*Sqrt[ε1/μ1] - Ep*Cos[i]*Sqrt[ε2/μ2])/(Cos[i]*Sqrt[ε2/μ2] +
Cos[r]*Sqrt[ε1/μ1])), Ers -> -((Es*Cos[r]*Sqrt[ε2/μ2] -
Es*Cos[i]*Sqrt[ε1/μ1])/(Cos[i]*Sqrt[ε1/μ1] + Cos[r]*Sqrt[ε2/μ2])),
Etp -> (2*Ep*Cos[i]*Sec[r]*Sqrt[ε1/μ1])/(Cos[i]*Sec[r]*Sqrt[ε2/μ2] + Sqrt[ε1/μ1]),
Ets -> Es - (Es*Cos[r]*Sqrt[ε2/μ2] - Es*Cos[i]*Sqrt[ε1/μ1])/(Cos[i]*Sqrt[ε1/μ1] +
Cos[r]*Sqrt[ε2/μ2])} }

```

## Appendix B MATLAB Program to model reflectance data and compare it to experimental Data

```
%===== Main program to test multilayer reflection calculations =====
%===== (c)GBC2020 =====
%
% -----
%Based on work by NALD (c) 2010 and Indika

clear

clc;

% stepwidth width
stepwidth = 1.0;

% Numbers of layers - in addition to ambient!!!
% prompt = 'How many layers are there besides the...
%ambient layer? \n';
% Nblay = input(prompt);
Nblay = 2;

% Material id# for each layer
% prompt = ['Input a matrix ( [id1; id2; id...]) of material IDs for...
%the layers counted above,top to bottom: subs for ambient;'
...\n uAlN, uGaN, uInN, nGaN, pGaN \n'];
% Eps_lay = input(prompt);
% Eps_lay = [5, 9];

% Dielectric function of ambient
eps_amb = 1;

% Dielectric function of Substrate - or last infinite medium
eps_sub = 1;

% Thickness for each layer (nm)
% prompt = ['How thick are the layers (nm) top to bottom? \n'...
%'(input a matrix[thick1, thick2, thick...])'...
%'(Sapphire substrates are 435 micron thick): \n'];
% thi_lay = input(prompt);
thi_lay = [55, 435000];

% Thickness variation for each layer (nm)
% prompt = ['What is the variation in thickness for each layer (nm)? \n'...
% '(input a matrix [thickvar1, thickvarvar2, thickvar...])\n'];
```

```

% thicknvar = input(prompt);
thicknvar = [10, 0];

% Interface perfection / loss for each layer

InterfPerf(1:Nblay) = 1;

% Interface perfection variation range

InterfPerfvar(1:Nblay) = 0;

% limits for x-axis range in simulation -
% Also limits for reading experimental FTIR data spectrum
% prompt = 'What wavenumber range do you want to analyze?...
% [xlowlimit,xuplimit] \n';
% xrange = input(prompt);
% xlowlimit = xrange(1);
% xuplimit = xrange(2);

xlowlimit = 400;
xuplimit = 7000;

% Parthilay: initial thickness array - which are the parent parameter!!
Parthilay = thi_lay;
% ParInterfPerf: initial Interface perfections parameter
% always with respect to layer k/k+1
ParInterfPerf = InterfPerf;

% enter here the number of childrens generated through
% each fit iteration cycle
itnumb = 30;

% stop if best least-square fit value is below bestfitvalue
% bestfitvalue = input('What threshold would you like for...
% the least square fit value to cross? \n');
bestfitvalue = 1;

% read in experimental data array
[wavenum, ExpRefl, start, stop, NbStep, inpath, infile]= ...
    read_experiment_csv(xlowlimit, xuplimit);
if (NbStep==0)
    error('error reading in experimental data');
    % break;
end

```

```

%-----%
% get all dielectric function values
% get the initial simulation parameter sets for the parent

% epspar=zeros(Nblay,NbStep,itnumb);
% epsper=zeros(Nblay,NbStep,itnumb);

epsinfper(1,1) = 7.7;
epsinfper(1,2) = 0.50; % epsinf and delta_epsinf
epsinfpar(1,1) = 7.7;
epsinfpar(1,2) = 0.50; % epsinf and delta_epsinf

oscper(1, 1) = 582.0;
oscper(1, 2) = 1.00; % WLO1 Oscillator strength and delta WLO1
gamper(1, 1) = 6.5;
gamper(1, 2) = .10; % gamLO1 and delta gamLO1
oscper(1, 3) = 465.0;
oscper(1, 4) = 1.00; % WTO1 and delta WTO1
gamper(1, 3) = 2.9;
gamper(1, 4) = .10; % gamWTO1 and delta gamWTO1

oscpar(1, 1) = 568.00;
oscpar(1, 2) = 1.00; % SLO2 Oscillator strength and delta SLO2
gampar(1, 1) = 7.7;
gampar(1, 2) = .10; % gamLO2 and delta gamLO2
oscpar(1, 3) = 423.00;
oscpar(1, 4) = 1.00; % WTO2 and delta WTO2
gampar(1, 3) = 3.94;
gampar(1, 4) = .10; % gamTO2 and delta gamTO2

plasma_freq(1) = 4 000;
plasma_freq(2) = 5; % Plasma frequency and delta Plasma frequency
plasma_gam(1) = 1500;
plasma_gam(2) = 50; % damping of plasma frequency and delta

gamlpp(1,1) = 12;          gamlpp(1,2) = 0.2;
gamlpp(2,1) = 375;        gamlpp(2,2) = 6;

fpar=repmat(oscpar',[1 itnumb]);
fper=repmat(oscper',[1 itnumb]);
gpar=repmat(gampar',[1 itnumb]);
gper=repmat(gamper',[1 itnumb]);
glpp=repmat(gamlpp,[1 1 itnumb]);

%rename variables, may be unnecessary

```

```

xaxis=wavenum;
Numbstep=NbStep;
Numblay=Nblay;
thilay = Parthilay;
IntPerf=ParInterfPerf;

%convert cm-1 to omega( angular frequency
wavenum = 2*pi()*xaxis/1e7;

% find incident angle, based on manual of rotating platform
thetai=(20)/180*pi();

%set initial value for rmsrefl
rmsrefl=1e4;

% Load the output matrix for sapphire, can be recalculated using script
% in Sapphire Substrate folder
load sapphireLf.mat

xaxisq = xaxis.^2;
ll=1;
err = 0.003;

while rmsrefl>err

    epsinfparit(1,:)=epsinfpar(1)+(0.5-rand(1,itnumb)).*epsinfpar(2);
    epsinfperit(1,:)=epsinfper(1)+(0.5-rand(1,itnumb)).*epsinfper(2);
    oscparit([1,3],1:itnumb) = fpar([1,3],:)+...
        (0.5-rand(2,itnumb)).*fpar([2,4],:);
    oscperit([1,3],1:itnumb) = fper([1,3],:)+...
        (0.5-rand(2,itnumb)).*fper([2,4],:);
    gamparit([1,3],1:itnumb) = gpar([1,3],:)+...
        (0.5-rand(2,itnumb)).*gpar([2,4],:);
    gamperit([1,3],1:itnumb) = gper([1,3],:)+...
        (0.5-rand(2,itnumb)).*gper([2,4],:);
    plasma_freqit(1,:) = plasma_freq(1)+...
        (0.5-rand(1,itnumb)).*plasma_freq(2);
    plasma_gamit(1,:) = plasma_gam(1)+...
        (0.5-rand(1,itnumb)).*plasma_gam(2);
    gamlppit(1:2,1,1:itnumb) = glpp(:,1,:)+...
        (0.5-rand(2,1,itnumb)).*glpp(:,2,:);

    % calculate initial dielectric functions for each layer
    for m = 1:Nblay-1

        for j=1:length(xaxis)

```

```

itoscper(1,:)=squeeze((xaxisq(j)-...
    (0.5*(plasma_freqit(1,:).^2 + oscperit(1,:).^2-...
    ((plasma_freqit(1,:).^2 + oscperit(1,:).^2).^2-...
    4.*plasma_freqit(1,:).^2.*oscperit(3,:).^2).^0.5))+ ...
    1i.*xaxis(j).*squeeze(gamlppit(1,:,:)).');
itoscper(2,:)=squeeze((xaxisq(j)-...
    (0.5*(plasma_freqit(1,:).^2 + oscperit(1,:).^2+...
    ((plasma_freqit(1,:).^2 + oscperit(1,:).^2).^2-...
    4.*plasma_freqit(1,:).^2.*oscperit(3,:).^2).^0.5))+ ...
    1i.*xaxis(j).*squeeze(gamlppit(2,:,:)).');

itoscpar(1,:)=squeeze((xaxisq(j)-...
    (0.5*(plasma_freqit(1,:).^2 + oscparit(1,:).^2-...
    ((plasma_freqit(1,:).^2 + oscparit(1,:).^2).^2-...
    4.*plasma_freqit(1,:).^2.*oscparit(3,:).^2).^0.5))+ ...
    1i.*xaxis(j).*squeeze(gamlppit(1,:,:)).');
itoscpar(2,:)=squeeze((xaxisq(j)-...
    (0.5*(plasma_freqit(1,:).^2 + oscparit(1,:).^2+...
    ((plasma_freqit(1,:).^2 + oscparit(1,:).^2).^2-...
    4.*plasma_freqit(1,:).^2.*oscparit(2,:).^2).^0.5))+ ...
    1i.*xaxis(j).*squeeze(gamlppit(2,:,:)).');

Epsper(j,:)= epsinfperit(1,:).*prod(itoscper)./((xaxisq(j)+...
    1i*plasma_gamit(1,:).*xaxis(j)).*(xaxisq(j)+...
    1i*gamperit(3,:).*wavenum(j)-(oscperit(3,:).^2)));

Epspar(j,:)= epsinfparit(1,:).*prod(itoscpar)./((xaxisq(j)+...
    1i*plasma_gamit(1,:).*xaxis(j)).*(xaxisq(j)+...
    1i*gamparit(3,:).*wavenum(j)-(oscparit(3,:).^2)));
end

end % end for m - layers .....

%set up variable thickness, surface perfection,
%make sure it is between 1 and 0.05
thilay = Parthilay+(rand(itnumb,Numblay)*2-1).*thicknvar;
IntPerf = [0.5,0.5]+(rand(itnumb,Numblay)*2-1).*InterfPerfvar;
IntPerf(IntPerf>1)=1;
IntPerf(IntPerf<0)=0.05;

% initialize calculated reflection
testrefl = zeros(Numbstep,itnumb);

```



```

% Start timer
tic

%Calculate the input Matrix
Lainv=1/2*[0 1 -1/cos(thetai) 0; 0 1 1/cos(thetai) 0;...
    1/cos(thetai) 0 0 1; -1/cos(thetai) 0 0 1];

kx=sin(thetai);

for jj = 1:itnumb

    [T,ctheta(1:Numblay,jj)] = inmatmaker(Numbstep, Epspar, ...
        Epsper,jj,kx, Numblay,IntPerf, wavenum, thilay);

    [diffsq(jj),testrefl(:,jj)] = reflrmsmaker(T,Lf,...
        Numbstep, Lainv, ExpRefl);

end % end for itnumb

newrmsrefl = sqrt((diffsq)/Numbstep);
% Pick the minimum rms and store those values to start a new search
[minrms, ii] = min(newrmsrefl);

if minrms-rmsrefl<err || ll<10
    epsinfpar(1) = epsinfparit(1,ii);
    epsinfper(1) = epsinfperit(1,ii);
    fpar([1,3,:]) = repmat(oscparit([1,3],ii),1,itnumb);
    fper([1,3,:]) = repmat(oscperit([1,3],ii),1,itnumb);
    gpar([1,3,:]) = repmat(gamparit([1,3],ii),1,itnumb);
    gper([1,3,:]) = repmat(gamperit([1,3],ii),1,itnumb);
    plasma_freq(1) = plasma_freqit(1,ii);
    plasma_gam(1) = plasma_gamit(1,ii);
    glpp(1:2,1,:) = repmat(gamlppit(:,ii),1,1,30);
    IntPerf = squeeze(IntPerf(ii,:));

    fprintf('minrms is %f, this round rms is %f, round %d \n',...
        rmsrefl,minrms,ll)
else
    fprintf('minrms for round %d is %f\n',ll,minrms)
end

if minrms<rmsrefl
    rmsrefl=minrms;
    set = struct('Refl',testrefl(:,ii),'thick',thilay(ii,:),...
        'rough',IntPerf,'RMS',rmsrefl, 'epspar', epsinfpar,...


```

```

        'epsper', epsinfper, 'oscpa', fpar(:,1),...
        'oscpa', fper(:,1), 'gampar', gpar(:,1),...
        'gampar', gper(:,1), 'plasma_freq', plasma_freq,...
        'plasma_gam', plasma_gam(:,1), 'gamlpp', glpp(:,1),...
        'ctheta', ctheta(:,ii));
    [minrms, IntPerf]
    plot(xaxis, testrefl(:,ii), xaxis, ExpRefl)
    drawnow
    save([infile(1:end-3), '.mat'], 'set')
end

Refl = testrefl(:,jj);

testthick = thilay;
ll = ll + 1;
end

function [mat_prop] = de_init(mat)
% (c) GBC 2020 based on work  NALD2010 - last updated: sep, 2010 by Indika

%

% display (eps_lay_num);
switch mat
case 1 % ambient
    epsinfpar = 1.0;
    epsinfper = 1.0;
    oscpar = 0.0;
    oscper = 0.0;
    gampar = 0.0;
    gamper = 0.0;
    plasma_freq = 0.0;
    plasma_gam = 0.0;

% case {'AlN', 'aln'} % = AlN layer
% eps_inf = 4.7; del_eps = 0.10;
% osc(1,1) = 880.00; del_osc(1,1) = 0.00; % SLO1 Oscillator strength and
delta SLO1
% gam(1,1) = 0.00; del_gam(1,1) = 0.00; % gamLO1 and delta gamLO1
% osc(1,2) = 670.00; del_osc(1,2) = 0.00; % WTO1 and delta WTO1
% gam(1,2) = 3.0; del_gam(1,2) = 0.0; % gamWTO1 and delta gamWTO1
%
```

```

% %      mat_prop(2, 2) = 0.00;      mat_prop(3,2) = 0.00; % SLO2 Oscilator strength
and delta SLO2
% %      mat_prop(4, 2) = 0.00;      mat_prop(5,2) = 0.00; % gamLO2 and delta
gamLO2
% %      mat_prop(6, 2) = 0.00;      mat_prop(7,2) = 0.00; % WTO2 and delta WTO2
% %      mat_prop(8, 2) = 0.00;      mat_prop(9,2) = 0.00; % gamTO2 and delta
gamTO2
% %
% %      mat_prop(2, 3) = 0.00;      mat_prop(3,3) = 0.00; % SLO3 Oscilator strength
and delta SLO3
% %      mat_prop(4, 3) = 0.00;      mat_prop(5,3) = 0.00; % gamLO3 and delta
gamLO3
% %      mat_prop(6, 3) = 0.00;      mat_prop(7,3) = 0.00; % WTO3 and delta WTO3
% %      mat_prop(8, 3) = 0.00;      mat_prop(9,3) = 0.00; % gamTO3 and delta
gamTO3
%
%      plasma_freq = 0.00;      del_pf = 0.00; % Plasma frequency and delta
Plasma frequency
%      plasma_gam = 0.00;      del_pg = 0.00; % damping of plasma frequency
and delta
%
%
%
%
case {'GaN','gan',10} % = undoped GaN

epsinfper(1) = 5.15;      epsinfper(2) = 0.10; % epsinf and delta_epsinf
epsinfpar(1) = 5.34;      epsinfpar(2) = 0.10; % epsinf and delta_epsinf

%Perpendicular osicillators (to c-axis)
oscper(1, 1) = 740;      oscper(1,2) = 5.00; % WLO1 and delta WLO1
gamper(1, 1) = 10;      gamper(1,2) = 2.00; % gamLO1 and delta gamLO1
oscper(1, 3) = 560.9;      oscper(1,4) = 2.00; % WTO1 and delta WTO1
gamper(1, 3) = 16;      gamper(1,4) = 2.00; % gamTO1 and delta gamTO1

%Parallel osicillators (to c-axis)
oscpar(1, 1) = 734.5 ;      oscpar(1,2) = 3.00; % WLO5 and delta WLO5
gampar(1, 1) = 7;      gampar(1,2) = 10; % gamLO5 and delta gamLO5
oscpar(1, 3) = 538.0;      oscpar(1,4) = 3.20; % WTO5 and delta WTO5
gampar(1, 3) = 6;      gampar(1,4) = 10; % gamTO5 and delta gamTO5

plasma_freq(1) = 1000;      plasma_freq(2) = 300; % Plasma frequency and delta
Plasma frequency
plasma_gam(1) = 200;      plasma_gam(2) = 200; % damping of plasma frequency and
delta

```

```

case 5    % = InN layer    %Bungaro et al., Ab initio phonon dispersion of wurtzite AlN, Gan,
InN, Phys rev B. 61, (2000)
    epsinfper(1,1) = 7.27;    epsinfper(1,2) = 0.10; % epsinf and delta_epsinf
    epsinfpar(1)   = 6.94;    epsinfpar(2)   = 0.10; % epsinf and delta_epsinf

    oscper(1, 1) = 595.0;    oscper(1, 2) = 10.00; % SLO1 Oscilator strength and delta
SLO1
    gamper(1, 1) = 5.00;    gamper(1, 2) = 1.00; % gamLO1 and delta gamLO1
    oscper(1, 3) = 477.0;    oscper(1, 4) = 2.00; % WTO1 and delta WTO1
    gamper(1, 3) = 5.0;    gamper(1, 4) = 1.00; % gamWTO1 and delta gamWTO1

    oscpar(1, 1) = 580.00;    oscpar(1, 2) = 3.00; % SLO2 Oscilator strength and delta
SLO2
    gampar(1, 1) = 5.00;    gampar(1, 2) = 1.00; % gamLO2 and delta gamLO2
    oscpar(1, 3) = 443.00;    oscpar(1, 4) = 2.00; % WTO2 and delta WTO2
    gampar(1, 3) = 5.00;    gampar(1, 4) = 1.00; % gamTO2 and delta gamTO2

    plasma_freq(1) = 1600;    plasma_freq(2) = 300; % Plasma frequency and delta
Plasma frequency
    plasma_gam(1) = 200;    plasma_gam(2) = 50; % damping of plasma frequency and
delta
%
%
% case 6    % = InN layer top
%    mat_prop(1,1) = 8.3;    mat_prop(1,2) = 0.10; % epsinf and delta_epsinf
%
%    mat_prop(2, 1) = 590.00;    mat_prop(3,1) = 1.00; % SLO1 Oscilator strength
and delta SLO1
%    mat_prop(4, 1) = 0.00;    mat_prop(5,1) = 0.00; % gamLO1 and delta
gamLO1
%    mat_prop(6, 1) = 480.00;    mat_prop(7,1) = 0.00; % WTO1 and delta WTO1
%    mat_prop(8, 1) = 3.0;    mat_prop(9,1) = 0.0; % gamWTO1 and delta
gamWTO1
%
%    mat_prop(2, 2) = 0.00;    mat_prop(3,2) = 0.00; % SLO2 Oscilator strength
and delta SLO2
%    mat_prop(4, 2) = 0.00;    mat_prop(5,2) = 0.00; % gamLO2 and delta gamLO2
%    mat_prop(6, 2) = 0.00;    mat_prop(7,2) = 0.00; % WTO2 and delta WTO2
%    mat_prop(8, 2) = 0.00;    mat_prop(9,2) = 0.00; % gamTO2 and delta gamTO2
%
%    mat_prop(2, 3) = 0.00;    mat_prop(3,3) = 0.00; % SLO3 Oscilator strength
and delta SLO3
%    mat_prop(4, 3) = 0.00;    mat_prop(5,3) = 0.00; % gamLO3 and delta gamLO3
%    mat_prop(6, 3) = 0.00;    mat_prop(7,3) = 0.00; % WTO3 and delta WTO3
%    mat_prop(8, 3) = 0.00;    mat_prop(9,3) = 0.00; % gamTO3 and delta gamTO3

```

```

%
%   mat_prop(2, 4) = 3500.00;   mat_prop(3,4) = 1000.00; % Plasma frequency and
delta Plasma frequency
%   mat_prop(4, 4) = 300.00;   mat_prop(5,4) = 300.00; % damping of plasma
frequency and delta
%   mat_prop(6, 4) = 0.00;   mat_prop(7,4) = 0.00; % not used
%   mat_prop(8, 4) = 0.00;   mat_prop(9,4) = 0.00; % not used
%
%
% case 7   % = GaN buffer layer
%
%   mat_prop(1,1) = 4.73;   mat_prop(1,2) = 0.1; % epsinf and delta_epsinf
%
%   mat_prop(2, 1) = 740.00;   mat_prop(3,1) = 1.00; % SLO1 Oscilator strength
and delta SLO1
%   mat_prop(4, 1) = 1.00;   mat_prop(5,1) = 1.00; % gamLO1 and delta gamLO1
%   mat_prop(6, 1) = 561.00;   mat_prop(7,1) = 1.00; % WTO1 and delta WTO1
%   mat_prop(8, 1) = 4.0;   mat_prop(9,1) = 1.0; % gamWTO1 and delta
gamWTO1
%
%   mat_prop(2, 2) = 0.00;   mat_prop(3,2) = 0.00; % SLO2 Oscilator strength
and delta SLO2
%   mat_prop(4, 2) = 0.00;   mat_prop(5,2) = 0.00; % gamLO2 and delta gamLO2
%   mat_prop(6, 2) = 0.00;   mat_prop(7,2) = 0.00; % WTO2 and delta WTO2
%   mat_prop(8, 2) = 0.00;   mat_prop(9,2) = 0.00; % gamTO2 and delta gamTO2
%
%   mat_prop(2, 3) = 0.00;   mat_prop(3,3) = 0.00; % SLO3 Oscilator strength
and delta SLO3
%   mat_prop(4, 3) = 0.00;   mat_prop(5,3) = 0.00; % gamLO3 and delta gamLO3
%   mat_prop(6, 3) = 0.00;   mat_prop(7,3) = 0.00; % WTO3 and delta WTO3
%   mat_prop(8, 3) = 0.00;   mat_prop(9,3) = 0.00; % gamTO3 and delta gamTO3
%
%   mat_prop(2, 4) = 00.00;   mat_prop(3,4) = 0.00; % Plasma frequency and
delta Plasma frequency
%   mat_prop(4, 4) = 00.00;   mat_prop(5,4) = 0.00; % damping of plasma
frequency and delta
%   mat_prop(6, 4) = 0.00;   mat_prop(7,4) = 0.00; % not used
%   mat_prop(8, 4) = 0.00;   mat_prop(9,4) = 0.00; % not used
%

```

case {'Subs','subs',9} % Sapphire Yu et al, J. Vac. Sci. Technol. A, Vol. 22 No.4 Jul/Aug (2004)

```

epsinfper(1) = 3.10;   epsinfper(2) = 0.07; % epsinf and delta_epsinf
epsinfpar(1) = 3.10;   epsinfpar(2) = 0.03; % epsinf and delta_epsinf

```

```

%Perpendicular osicillators (to c-axis)
oscper(1, 1) = 387.94;    oscper(1,2) = 0.1; % WLO1 and delta WLO1
gamper(1, 1) = 3.01;     gamper(1,2) = 0.3; % gamLO1 and delta gamLO1
oscper(1, 3) = 384.19;   oscper(1,4) = 0.1; % WTO1 and delta WTO1
gamper(1, 3) = 2.58;     gamper(1,4) = 0.3; % gamTO1 and delta gamTO1

oscper(2, 1) = 481.81;    oscper(2,2) = 0.1; % WLO2 and delta WLO2
gamper(2, 1) = 2.63 ;     gamper(2,2) = 0.1; % gamLO2 and delta gamLO2
oscper(2, 3) = 439.46;   oscper(2,4) = 0.1; % WTO2 and delta WTO2
gamper(2, 3) = 1.45 ;     gamper(2,4) = 0.7; % gamTO2 and delta gamTO2

oscper(3, 1) = 629.69;    oscper(3,2) = 0.1; % WLO3 and delta WLO3
gamper(3, 1) = 7.24 ;     gamper(3,2) = 0.5; % gamLO3 and delta gamLO3
oscper(3, 3) = 568.89 ;   oscper(3,4) = 0.4; % WTO3 and delta WTO3
gamper(3, 3) = 4.32;     gamper(3,4) = 0.9; % gamTO3 and delta gamTO3

oscper(4, 1) = 909.96 ;   oscper(4,2) = 0.9; % WLO4 and delta WLO4
gamper(4, 1) = 20.89;     gamper(4,2) = 1.1; % gamLO4 and delta gamLO4
oscper(4, 3) = 633.92;   oscper(4,4) = 0.3; % WTO4 and delta WTO4
gamper(4, 3) = 5.62;     gamper(4,4) = 0.5; % gamTO4 and delta gamTO4

%Parallel osicillators (to c-axis)
oscpa(1, 1) = 880.93 ;    oscpa(1,2) = 0.5; % WLO5 and delta WLO5
gampar(1, 1) = 19.10;     gampar(1,2) = 1.1; % gamLO5 and delta gamLO5
oscpa(1, 3) = 582.99;    oscpa(1,4) = 0.3; % WTO5 and delta WTO5
gampar(1, 3) = 0.46;     gampar(1,4) = 0.6; % gamTO5 and delta gamTO5

oscpa(2, 1) = 510.81 ;    oscpa(2,2) = 0.1; % WLO6 and delta WLO6
gampar(2, 1) = 1.15;     gampar(2,2) = 0.07; % gamLO6 and delta gamLO6
oscpa(2, 3) = 398.58;    oscpa(2,4) = 0.5; % WTO6 and delta WTO6
gampar(2, 3) = 0.43;     gampar(2,4) = 0.9; % gamTO6 and delta gamTO6

plasma_freq(1) = 0;   plasma_freq(2) = 0; % Plasma frequency and delta Plasma
frequency
plasma_gam(1) = 0;   plasma_gam(2) = 0; % damping of plasma frequency and
delta

end % switch (eps_lay_numb)

mat_prop = struct('epspar',epsinfpar, 'epsper', epsinfper, 'freqper', oscper, 'decayper', gamper,
'freqpar',...
    oscpar, 'decaypar', gampar, 'plasma', plasma_freq, 'pdecay', plasma_gam);

end % end function

```

```

function [Epspar, Epsper] = de_lorentz(matprop, wave_array, mat)
% (c) Brendan Cross 2017 based on work NALD -

wavenum = wave_array;
wavenumsq = wave_array.^2;

% if ismatrix(matprop.freqper)
%   matprop.freqper(:,1)=matprop.freqper;
%   matprop.freqpar(:,1)=matprop.freqpar;
%   matprop.decayper(:,1)=matprop.decayper;
%   matprop.decaypar(:,1)=matprop.decaypar;
%   matprop.plasma(:,1)=matprop.plasma(:);
%   matprop.pdecay(:,1)=matprop.pdecay(:);
% end

%mat_prop = struct('epspar',epsinfpar, 'epsper', epsinfper, 'freqper', oscper, 'decayper', gamper,
'freqpar',...
%   oscpar, 'decaypar', gampar, 'plasma', plasma_freq, 'pdecay', plasma_gam);
[~,~,iter]=size(matprop.freqpar);
Epspar = zeros(length(wave_array),iter);
Epsper = zeros(length(wave_array),iter);
switch mat
case 5
    %based on Kasic, et al, Effective electron mass and phonon modes
    %in n-type hexagonal InN, Phys Rev B. 65, (2002)
    % q close to zero

    for j=1:length(wave_array)

        oscper=squeeze((wavenum(j).^2- ...
            ((0.5*(matprop.plasma(:,1).^2 + matprop.freqper(:,1,:).^2+ ...
            flip.*((matprop.plasma(:,1).^2 + matprop.freqper(:,1,:).^2).^2-...
            4.*matprop.plasma(:,1).^2.*matprop.freqper(:,3,:).^2).^0.5))).^0.5).^2- ...
            1i.*wave_array(j).*matprop.decayper(:,1,:)));

        oscpar=squeeze((matprop.freqpar(:,1,:).^2- ...
            (0.5*(matprop.plasma(:,1).^2 + matprop.freqpar(:,1,:).^2+ ...
            flip.*((matprop.plasma(:,1).^2 + matprop.freqpar(:,1,:).^2).^2-...
            4.*matprop.plasma(:,1).^2.*matprop.freqpar(:,2,:).^2).^0.5))).^0.5- ...
            1i.*wave_array(j).*gamlpppar(j)));

        Epsper(j,:) = matprop.epspar(:,1).*prod(oscper)'./((wavenumsq(j)+...
            1i*matprop.pdecay(:,1).*wave_array(j)).*(wavenumsq(j)+...

```

```

        1i*matprop.decayper(:,3,:).*wavenum(j)-...
        matprop.freqper(:,3,:)));

    Epspar(j,:) = matprop.epspar(:,1).*prod(oscpar)'./((wavenumsq(j)+...
        1i*matprop.pdecay(:,1).*wave_array(j)).*(wavenumsq(j)+...
        1i*matprop.decaypar(:,3,:).*wavenum(j)-...
        matprop.freqpar(:,3,:)));
    end
otherwise

    %Based on model by F Gervais and B Piriou 1974 J. Phys. C: Solid State
    %Phys. 7 2374, with free free electron term
    for j=1:length(wave_array)
        oscper=squeeze((matprop.freqper(:,1,:).^2-wavenumsq(j)-
1i.*wave_array(j)*matprop.decayper(:,1,:))./...
        (matprop.freqper(:,3,:).^2-wavenumsq(j)-1i.*wave_array(j)*matprop.decayper(:,3,:)));

        oscpar=squeeze((matprop.freqpar(:,1,:).^2-wavenumsq(j)-
1i.*wave_array(j).*matprop.decaypar(:,1,:))./...
        (matprop.freqpar(:,3,:).^2-wavenumsq(j)-1i.*wave_array(j).*matprop.decaypar(:,3,:)));

        Epspar(j,:) = matprop.epspar(:,1).*(prod(oscpar)'-matprop.plasma(:,1).^2./...
        (wavenumsq(j)+matprop.pdecay(:,1).*1i.*wave_array(j)));
        Epsper(j,:) = matprop.epsper(:,1).*(prod(oscper)'-matprop.plasma(:,1).^2./...
        (wavenumsq(j)+matprop.pdecay(:,1).*1i.*wave_array(j)));
    end
end

function [T,ctheta]= inmatmaker(Numbstep, epspar, epsper,jj,kx,Numblay, IntPerf, wavenum,
thilay)
% -----
% set up material rotation.
% psi around z, ctheta around new x, phi around new z. since epsx=epsy,
% no rotation is necessary beyond theta to get inclination of z relative
% to c - crystal axis
psi=zeros(Numblay,1);
ctheta=rand(Numblay,1)*pi()/4;
% ctheta=0;
phi=zeros(Numblay,1);

% calculate sines and cosines of rotation angles
c1=cos(psi); s1=sin(psi); % 1 -psi -phi in goldstein
c2=cos(ctheta); s2=sin(ctheta); % 2 -cheta - theta in goldstein
c3=cos(phi); s3=sin(phi); % 3 - phi, psi in goldstein

```



```

%Initialize rotation matrix for each layer
A = zeros(3,3,Numblay);

%find rotation matrix for each layer
for i=1:Numblay

    A(:,i,i)=[c3(i)*c1(i)-c2(i)*s1(i)*s3(i) -s3(i)*c1(i)-c2(i)*s1(i)*c3(i) s2(i)*s1(i);
              c3(i)*s1(i)+c2(i)*c1(i)*s2(i) -s3(i)*s1(i)+c2(i)*c3(i)*c1(i) -s2(i)*c1(i);
              -s2(i)*s3(i) -s2(i)*c3(i) c2(i)];

end

for m = 1:Numblay-1
    %Initialize delta, T, q and Q.
    delta = zeros(Numbstep,4,4);
    Q = zeros(Numbstep,4,4);
    q = zeros(Numbstep,4);
    q1 = zeros(Numbstep,4);
    T=repmat(eye(4),1,1,Numbstep);

    % Calculate Matrix: M0 = ambient - Layer_1 and M_subs = Layer_N - Substrate

    for kk = 1:Numbstep

        eps = A(:,i,m)*[(epsper(kk,jj)) 0 0;
                        0 (epsper(kk,jj)) 0;
                        0 0 (epspar(kk,jj))]*A(:,i,m).';

        delta(kk, :, :) = [-kx*eps(3,1)/eps(3,3) -kx*eps(3,2)/eps(3,3) 0 1-kx^2/eps(3,3);
                           0 0 -1 0;
                           eps(2,3)*eps(3,1)/eps(3,3)-eps(2,1) kx^2-eps(2,2)+eps(2,3)*eps(3,2)/eps(3,3) 0
                           kx*eps(2,3)/eps(3,3);
                           eps(1,1)-eps(1,3)*eps(3,1)/eps(3,3) eps(1,2)-eps(1,3)*eps(3,2)/eps(3,3) 0 -
                           kx*eps(1,3)/eps(3,3)];

        [Q(kk, :, :), B] = eig(squeeze(delta(kk, :, :)));
        q(kk, :) = diag(B);

        [q1(kk, :), index] = sort(q(kk, :), 'ComparisonMethod', 'real');

        Q(kk, :, :) = Q(kk, :, index);

    end
end

```

```

Q1 = squeeze(sum(Q,2));
sortvar = real(q1)./abs(imag(q1));

for ii = 2:550
    for lll = 1:3

        P = sortvar(ii+1, lll:end)-2*sortvar(ii, lll)+sortvar(ii-1, lll);
        [~, ind] = min((P));

%         q1(ii+1:end, [lll, ind+lll-1]) = q1(ii+1:end, [ind+lll-1, lll]);
        Q(ii+1:end, :, [lll, ind+lll-1]) = Q(ii+1:end, :, [ind+lll-1, lll]);

        sortvar(ii+1:end, [lll, ind+lll-1]) = sortvar(ii+1:end, [ind+lll-1, lll]);
    end
end

qp = q1(:, [4, 1, 3, 2]);

if m ~= Numblay
    for kk = 1:Numbstep
        q = qp(kk, :);
        beta = exp(1i*wavenum(kk)*q*thilay(jj, m))/(q.^0; q.^1; q.^2; q.^3);

        T(:, :, kk) =
squeeze(T(:, :, kk))*IntPerf(jj, m)/(beta(1)*eye(4)+beta(2)*squeeze(delta(kk, :, :))+beta(3)*squeeze(
delta(kk, :, :))^2+beta(4)*squeeze(delta(kk, :, :))^3);
    end
end
end
end

```